Study of the combined performance of the Digital Hadronic Calorimeter and the Silicon-Tungsten Electromagnetic Calorimeter

MELISSA ALMANZA SOTO

Department of Physics
McGill University, Montreal

A thesis submitted to McGill University in partial fulfillment of the requirements of the degree of

Master of Science

Abstract

This thesis presents a study of the alignment and the energy response to pions of a combined electromagnetic and hadronic calorimeter system using two calorimeter prototypes from the CALICE international collaboration: the Digital Hadron Calorimeter (DHCAL) and the Silicon-Tungsten Electromagnetic Calorimeter (Si-W ECAL). The data was taken in April 2011 at the Fermilab test beam facilities. The experimental setup was exposed to a range of beam energies from 4 to 120 GeV. A first study and correction of the misalignment between detectors was performed using muon tracks. The linearity of DHCAL for hadronic and electromagnetic showers was next investigated. The prototype presented significant signal saturation effects for beam energies above 60 GeV. Finally, energy calibration factors for the calorimeters were obtained for hadronic events. Using the calibration, the hadronic energy resolution of the DHCAL was calculated to become $44\%/\sqrt{E/GeV}$. This presents a 25% improvement from the energy resolution calculated with hit-to-energy conversion methods excluding ECAL.

Résumé

Cette thèse représente une étude de l'alignement et de la réponse en énergie aux pions d'un système de deux prototypes de calorimètre de la collaboration internationale CALICE: le Calorimètre Hadronique Digital (DHCAL) et le Calorimètre électromagnétique au Silicium-Tungstène (Si-W ECAL). Les données ont été prises en avril 2011 au centre de recherche Fermilab. Le montage expérimental a été soumis à des tests de faisceaux de particules allant de 4 à 120 GeV en energie. Les traces de muons ont été analysées et utilisées pour corriger le mésalignement entre les deux détecteurs. La linéarité du DHCAL a ensuite été étudiée pour les gerbes électromagnétiques et hadroniques. Des effets de saturation de signal ont été observés pour les energies supérieures à 60 GeV. Finalement, les facteurs de calibration en energie des calorimètres ont été obtenus pour les événements hadroniques. Après leur application, la résolution en énergie hadronique a été calculée à $44\%/\sqrt{E/GeV}$, ce qui représente une amélioration de 25% de ce qu'elle est si la méthode de conversion "hit"-énergie est utilisée sans la présence du ECAL.

Acknowledgements

I want to thank my supervisor François Corriveau for his patience, guidance, and words of encouragement while I was working on this thesis.

To my best friend Karen Macias, thank you for all your help in physics and life, it was really a blessing to have you as a friend.

To my small family Carlos Maciel and Orion, thank you for your love and for always being there for me in this once new chapter of our life.

A special thank you to my Soto family, even if we are far apart, you once again showed that you will always be there for me. Your support always inspires me to do my best.

To my grandmother Chuyita, I think that waiting for your call every Sunday kept me going. You always encouraged me to follow my dreams and are always proud of me no matter what, thank you.

Lastly, I would like to thank my mother. Thanks to you I am once again finishing another thesis. Without your example, love, and encouragement I would not be here.

Table of Contents

Abstract i
Résumé ii
Acknowledgements iii
Contribution of Author vii
List of Figures x
List of Tables xx

1 Introduction **1**

2 The Standard Model **4**
2.1 The Start of Particle Physics 4
2.2 The Standard Model 5

3 Particle Interactions with Matter **8**
3.1 Energy loss of heavy charged particles 8
3.1.1 Multiple Scattering 11
3.2 Energy loss of electrons and positrons 12
3.3 Interaction of photons with matter 13
3.3.1 Compton Scattering 13
3.3.2 Pair Production 14
3.4 Interaction of hadrons with matter 14
3.5 Particle showers 15
3.5.1 Electromagnetic showers 15
3.5.2 Hadronic showers 17

4 Calorimetry **19**

4.1 Homogeneous calorimeters 20

4.2 Sampling calorimeters 21

5 The international Linear Collider and CALICE Calorimeters **22**

5.1 The International Linear Collider 23

5.1.1 Particle Flow Algorithm 24

5.1.2 Experiments for the International Linear Collider 25

5.2 CALICE Calorimeter prototypes for ILC 26

5.2.1 AHCAL 29

5.2.2 SDHCAL 30

5.2.3 DHCAL 31

5.2.4 ScECAL 33

5.2.5 Si-W ECAL 34

6 Event selection and Particle ID **38**

6.1 Run parameters 40

6.1.1 Run parameters for DHCAL 44

6.1.2 Run parameters for Si-W ECAL 45

6.1.3 Combined Run parameters for ECAL + DHCAL 45

6.2 Sets of cuts for particle identification 46

7 Alignment **55**

7.1 Cuts for noise and track quality 56

7.2 Measurement of misalignment procedure 58

7.3 Correction of misalignment 62

7.4 Global Fit 65

8 Linearity for DHCAL **69**

8.1 Types of hadronic showers for the April 2011 testing period 71

8.2 Linearity analysis 71

9 Energy Analysis **77**
9.1 Calculation of energy deposited in ECAL absorber 77
9.2 Conversion of measured energy to MeV units 79
9.3 Calculation of energy deposited in DHCAL 81
9.4 Hadronic and electromagnetic energy resolution for June 2011 data 86
9.5 Hadronic energy resolution of the Si-W ECAL + DHCAL system 90
9.5.1 Diagonal Fit Method 91
9.5.2 Sum of Energies Method 92
9.5.3 Energy resolution comparison between the June 2011 and April 2011 data 93
9.5.4 Systematic uncertainties 98

10 Conclusions **101**

List of Abbreviations **103**

Bibliography **108**

Contribution of Author

The CALICE Collaboration is dedicated to R&D of high-granularity calorimeters for future high energy physics experiments. The collaboration has individual groups all around the world, each working in specific parts of the design, building and commissioning of the calorimeters. The data used for the analysis in this thesis was taken by the DHCAL and the Si-W ECAL groups using the Fermilab Test Beam Facilities in April 2011. The data sets were available to the author in a text file format. The author confirms sole responsibility for the creation of all presented figures and tables without a source specified in their caption. The contributions of the author for each chapter are:

- Chapter 1: A brief description of the present stated of high-energy physics experiments and particle detectors, a summary of the contributions of the CALICE Collaboration to the area of detector development, specifically the contributions of the McGill CALICE group for the DHCAL performance studies, and a preview of the contents of each chapter of this thesis.

- Chapter 2: A review of the literature regarding elementary particles and the Standard Model of Particle Physics and its connection to the area of experimental high-energy physics.

- Chapter 3: A review of the literature for particle interactions with matter in a particle detectors design perspective.

- Chapter 4: A description of the characteristics of the most common types of calorimeters from a review to the available literature.

- Chapter 5: A summary of the description of the International Linear Collider project, of the Particle Flow algorithm approach for calorimetry, as well as a description of the main characteristics of most CALICE calorimetry designs, all reviewed from the available literature.

- Chapter 6: Writing by the author and implementation of all computer codes necessary for the production of the Standard Plots. These include: codes for the conversion of the data sets from text format to ROOT TTree format to ease the reading of test run data, ROOT codes to read the TTree files, calculate all listed run parameters from the data, and print the Standard Plots. The author also contributed with the setting of particle identification cuts in the run parameters and the creation of a code to separate the original test run files into three TTree files, one for each type of particle in the test run.

- Chapter 7: Setting of the cuts for noise and track quality and the writing and execution of the codes to implement them. Definition of the misalignment parameters, writing and implementation of computer codes to calculate. Development of method and codes for the correction of misalignment and re-calculation of alignment parameters. Discussion of the results from the alignment correction methods. Writing and implementation of the computer codes necessary to produce the Global Fit Plots. Discussion of the results for all stages of the alignment methodology.

- Chapter 8: Writing and implementation of computer codes to read TTree files of each type of particle and find the mean number of hits through a Gaussian fit to the hits distribution for all available test runs. Calculation of mean hits and standard deviation averages for each beam energy and production of linearity plots with linear and exponential fits using ROOT. Discussion of the results.

- Chapter 9: Development of a method to calculate the energy deposition in the Si-W ECAL absorber layers. Development of the Paraboloid fit method to find the energy calibration parameters for the DHCAL using the Si-W ECAL event energy and its implementation using ROOT. Discussion of results for energy resolution between different hit-to-energy conversion methods.

- Chapter 10: A summary of the methods and results obtained throughout the analysis Chapters (Chapters 6, 7, 8 and 9). Conclusion on the findings from the analysis of the different data sets used.

List of Figures

2.1 Classification of the elementary particles. Quarks (in purple) and leptons (in green) are separated into three generations. The generations go from I to III in mass order, I being the lightest mass and III the heaviest. The bosons are separated by their type, gauge bosons in red and scalar bosons in yellow. The mass, electric charge, and spin are indicated for each particle. The electric charge is in units of e (charge of the electron). Obtained from [6]. 6

3.1 Mean energy loss per path length $\langle -\frac{dE}{dx} \rangle$ by ionization and excitation as a function of path length for the muon, pion, and proton in liquid hydrogen, helium gas, carbon, aluminum, iron, tin, and lead. Obtained from [10]. . . . 10

3.2 Mean energy loss per path length $\langle -\frac{dE}{dx} \rangle$ of μ^+ in copper as a function of the muon momentum. Obtained from [10]. 11

3.3 Longitudinal development of an electromagnetic shower for several radiation lengths X_0 of absorber material. The energy of the secondary particles is also stated for each step in terms of the initial photon's energy E_0. Obtained from [9]. 16

5.1 Schematic layout of the ILC. Obtained from [7]. 24

5.2 Profile view of the SiD detector describing the positioning of the main subsystems of the experiment. Obtained from [7]. 26

5.3 Profile view of the ILD detector describing the positioning of the main detector systems as well as the coil. All measurements are in millimeters. Obtained from [7]. 27

5.4 Conceptual map of calorimeter technologies for PFA Calorimeters. Obtained from [15] 28
5.5 Example photograph of the segmented active layer for the AHCAL physics prototype. The circular shapes show the carved regions in which the optical fibers were inserted. Obtained from [17]. 29
5.6 Example photograph of the segmented active layer before wrapping for the AHCAL technological prototype. Obtained from [20]. 30
5.7 DHCAL Configurations obtained from [24]. On the left: Main Stack before cabling, in the middle: TCMT, and on the right: the MinDHCAL. 33
5.8 Schematic 3D view of the Si-W ECAL physics prototype. Obtained from [26]. 35
5.9 Detailed measurements of one ECAL slab, showing an absorber (tungsten) layer sandwiched between two active (silicon) layers. All measurements are in millimeters. The separation between two silicon layers is composed of either only a tungsten layer or of two PCB, carbon structure, and aluminum glue in addition to the tungsten layer. Obtained from [27]. 36

6.1 Example of the X-Y, X-Z, and Y-Z Distribution Standard Slots for Si-W ECAL for run 630098 at 120 GeV. The scatter plots show many faulty modules which are easily recognizable as light and dark stripes along Z. The light stripe corresponds to modules that were off during the run and the dark stripes to constantly misfiring modules. 41
6.2 Example of the Standard Plots for DHCAL for a test run at 50 GeV in the April 2011 testing period. 42
6.3 Example of the Standard Plots for ECAL for a test run at 50 GeV in the April 2011 testing period. 43

6.4 Example of the Standard Plots for a combination of ECAL and DHCAL parameters for a test run at 50 GeV in the April 2011 testing period. Top row: The plot on the left is a 2D histogram of Event Energy in ECAL (in arbitrary units) vs the number of hits in DHCAL, this shows how the energy of events is shared between the two detectors; the center plot shows the distribution of how the hits in a shower are shared between the two detectors; on the right the distribution of Total Hits is shown. Bottom row: Histogram of the Ratio ECAL parameter; the center plot is a 2D histogram of the Ratio ECAL vs Total Hits parameters, it shows clear separation between the three types of particles measured and it is the main plot used for the particle ID in the April 2011 period; the plot on the right shows a 2D histogram of the Ratio ECAL vs the number of hits in DHCAL. 46

6.5 Example of a typical muon event for an April 2011 test run at 60 GeV. The top plots show the path of a muon starting on the left (first layer of Si-W ECAL and continuing all through the detector until reaching DHCAL (right plot) and again continuing its path until the last layer of DHCAL. The first three histograms on the second row show the XY, XZ, and YZ projections of ECAL respectively. The next three histograms of the second row show the XY, XZ, and YZ projections of DHCAL respectively. The bottom row shows 1D histograms of the X, Y, and Z distributions of hits in the event respectively. The first three histograms correspond to the ECAL 1D projections and the following three to DHCAL. 48

6.6 Example of a typical late showering pion event for an April 2011 test run at 60 GeV.The top plots show the path of the incoming pion starting on the left (first layer of Si-W ECAL and continuing all through the detector until reaching DHCAL (right plot) and again continuing its path until it starts a shower. The shower is fully contained in DHCAL. The first three histograms on the second row show the XY, XZ, and YZ projections of the hits in ECAL respectively. The next three histograms of the second row show the XY, XZ, and YZ projections of the hits in DHCAL respectively. The bottom row shows 1D histograms of the X, Y, and Z distributions of hits in the event respectively. The first three histograms correspond to the ECAL 1D projections and the following three to DHCAL. 49
6.7 Example of a typical positron event for an April 2011 test run at 60 GeV. The top plots show the path of the incoming positron starting on the left (first layer of Si-W ECAL and continuing a straight trajectory until reaching starting a shower. The shower is mostly contained by ECAL and only a few particles deposit energy in the first layers of DHCAL, which is shown on the plot on the right. The first three histograms on the second row show the XY, XZ, and YZ projections of the hits in ECAL respectively. The next three histograms of the second row show the XY, XZ, and YZ projections of the hits in DHCAL respectively. The bottom row shows 1D histograms of the X, Y, and Z distributions of hits in the event respectively. The first three histograms correspond to the ECAL 1D projections and the following three to DHCAL. 50
6.8 Example of the Ratio(0-15) vs Hits plot for a June 2011 test run at 32 GeV. The color squares represent the cuts for particle ID from Table 6.4. The color blue section corresponds to the positrons, the magenta section to the pions, and the green section to the muons. The gap between the pion and positron cuts in the vertical direction represents a mixture of hadronic and electromagnetic events. These events were discarded to reduce pion contamination in the positron sample and vice versa. 52

6.9 Example of the Ratio(0-15) plot after removing the muon events for a test run at 40 GeV from the June 2011 period. The first peak represents the pions, which start the shower later in the detector. The wider peak to the left corresponds to the positrons. The red lines represent the cuts for particle identification. The events between the red lines are discarded to minimize pion contamination in the positron sample and vice versa. 53

7.1 Example of a muon event with a considerable amount of noise in ECAL hits for an April 2011 test run at 60 GeV before clearing for noise. The top plots show the path of a muon starting on the left (first layer of Si-W ECAL and continuing all through the detector until reaching DHCAL (right plot) and again continuing its path until the last layer of DHCAL. The first three histograms on the second row show the XY, XZ and YZ projections of ECAL respectively. The next three histograms of the second row show the XY, XZ and YZ projections of DHCAL respectively. The bottom row shows 1D histograms of the X, Y and Z distributions of hits in the event respectively. The first three histograms correspond to the ECAL 1D projections and the following three to DHCAL. 57

7.2 2D Representation of a muon event with linear fits on XZ and YZ profiles of the detector Si-W ECAL+DHCAL system for a 60 GeV test run. The top left plot shows XZ projection of the muon's trajectory through Si-W ECAL until reaching its last layer and continuing on the DHCAL which is shown in the plot to the top right. The bottom left and bottom right plots show the same sequence but for the YZ projections. All fits are linear fits with p0 as the slope and p1 as the intercept to the vertical axis. 59

7.3 X Distance distribution for the 50 GeV test run muon tracks before moving DHCAL. 60

7.4 Results for the average alignment parameters before moving the DHCAL. For all plots, the runs are in the following order: 1=630081, 2=630090, 3=630091, 4=630092, 5=630093, and 6=630094. The data points are listed in Table 7.2. 61
7.5 X Distance distribution for the 50 GeV test run muon tracks after moving DHCAL. 63
7.6 Results for the average alignment parameters after moving the DHCAL with respect to the Si-W ECAL. For all plots, the runs are in the following order: 1=630081, 2=630090, 3=630091, 4=630092, 5=630093, and 6=630094. The information of the data points is listed in Table 7.4. 64
7.7 Profile hit representations of a muon event with Global Fit for a 60 GeV test run track after moving the track points of DHCAL (in magenta) with respect to the Si-W ECAL (in blue) and translating the full track to the horizontal axis. The first layer of the Si-W ECAL is placed at $z = 0$ and the first layer of DHCAL at $z = 20.225$ equivalent to the depth of ECAL plus $2\ cm$ of space between the two detectors. The top plot shows the XZ profile of the detector setup. The bottom plot shows the YZ profile. The error bars assigned to the hits are arbitrary, but they are the same for every hit of the same track. 66
7.8 Results for the average alignment parameters from the Global Fit after moving the DHCAL and Si-W ECAL to align the track to the center of the detector system. For all plots, the runs are in the following order: 1=630081, 2=630090, 3=630091, 4=630092, 5=630093, and 6=630094. The information of data points are listed in Table 7.6. 68

8.1 Example of a typical early showering pion event for an April 2011 test run at 60 GeV. The top plots show the path of the incoming positron starting on the left (first layer of Si-W ECAL and continuing a straight trajectory until reaching starting a shower. The shower is partly contained by ECAL and continues its development until reaching the first layers of DHCAL, which is shown on the plot on the right. The rest of the shower is then fully contained in DHCAL. The first three histograms on the second row show the XY, XZ and YZ projections of the hits in ECAL respectively. The next three histograms of the second row show the XY, XZ and YZ projections of the hits in DHCAL respectively. The bottom row shows 1D histograms of the X, Y and Z distributions of hits in the event respectively. The first three histograms correspond to the ECAL 1D projections and the following three to DHCAL. 70
8.2 Example of a Gaussian fit to the hits distribution of electromagnetic showers for a 40 GeV test run from June 2011, the fit only covers bins higher than 15% of the height of the peak. 72
8.3 Distribution of mean number of hits for all available 40 GeV test runs from the June 2011 testing period. The error bars represent the standard deviation from the Gaussian fits to the hits distributions rather than the error on the mean as this was measured to be less than one hit. 73
8.4 Linearity for electromagnetic and hadronic showers in the June 2011 testing period. In both figures, the red line represents a linear fit from 0 to 60 GeV given by Equation 8.1 to guide the eye and the blue line represents an exponential fit given by the function in Equation 8.2 74
8.5 Linearity for hadronic events in the April 2011 testing period, which start their shower within DHCAL (late showering pions). The red line represents a linear fit given by Equation 8.1 and the blue line represents an exponential fit given by the function in Equation 8.2 75

9.1 Hits distribution in DHCAL (top) and MIP Silicon energy distribution for Si-W ECAL (bottom) for a 50 GeV test run. The first is fitted a Gaussian function and the second a Landau function. The MIP Silicon energy distribution is presented in arbitrary units. 78
9.2 MPV from Landau fit to the silicon energy distribution of each available April 2011 test run. The first point from left to right corresponds to the 50 GeV test run: 630081; the following four points to 60 GeV runs: 630090, 630091, 630092, and 630093 respectively; and the final two points to 120 GeV runs: 630095 and 630097 respectively. 80
9.3 Hits in DHCAL (top) and Energy in ECAL (bottom) Distributions for all pions in the 50 GeV test run. 80
9.4 Hits in DHCAL (top) and Energy in ECAL (bottom) Distributions for early showering pions in the 50 GeV test run. 82
9.5 Scatter plot of the Hits in DHCAL vs Energy in ECAL Distributions for early showering pions in a 50 GeV test run. On the left is the color projection and on the right the LEGO view. 83
9.6 Paraboloid function fitted to the Scatter plot of the Hits in DHCAL vs Energy in ECAL Distributions for early showering pions in the 50 GeV test run. The plot shows the 2D function from Equation 9.4, the peaks at the top are due to the binning of the axes. 84
9.7 On the left: Scatter plot of the Hits in DHCAL vs Energy in ECAL Distributions for early showering pions in a 50 GeV test run. On the right: Contour projections of the paraboloid function fitted to the distribution on the left. . 85
9.8 Energy in DHCAL and Energy in ECAL Distributions for early showering pions in the 50 GeV test run. Both red lines are Gaussian fits to guide the eye. 86
9.9 Energy distribution of positrons for a 50 GeV test run from the June 2011 testing period. The red line represents a Gaussian fit covering only bins higher than 30% of the height of the peak. 87

9.10 Energy resolution for electromagnetic and hadronic showers in the June 2011 testing period. In both figures, the line represents the fit to Equation 9.8 setting the parameter b to zero. 89
9.11 On the left: Scatter plot of the Energy in DHCAL vs Energy in ECAL Distributions for early showering pions in the 50 GeV test run. On the right: Histogram of the diagonal projection of the distribution on the left. 91
9.12 Total energy distribution for the 50 GeV test run from the April 2011 testing period. Each entry is calculated from adding the energies measured by ECAL and DHCAL in the same event. 93
9.13 Hadronic energy resolution of the combined Si-W ECAL + DHCAL system. The fitted function is found in Equation 9.8. The parameter a is the stochastic term from Equation 9.8. The parameter b is set to zero in the fit. . 94
9.14 Energy resolution of DHCAL for late showering pions using the April 2011 data. The resolution was calculated using the linearity fit (same method used for the June 2011 data). The fitted function is found in Equation 9.8 and the parameter b was set to zero. 95
9.15 Energy resolution of DHCAL for late showering pions using the April 2011 data. The results were calculated using the correction factor from the paraboloid fit method. The fitted function is found in Equation 9.8. The parameter b is set to zero for the fit. 96

9.16 Hadronic energy resolution comparison between the June 2011 and April 2011 testing periods. The April 2011 results are shown for three methods of measuring the energy resolution. All of the lines represent fits to the data points following Equation 9.8 with b=0. Green and squares: Energy resolution of late showering pions for April 2011 calculated using the linearity fit. Magenta and diamonds: Energy resolution of pions in the June 2011 period, calculated from the linearity fit. Red and triangles: Energy resolution of late showering pions for April 2011 calculated using the correction factor from the paraboloid fit method. Blue and circles: Energy resolution of Early showering pions for the Si-W ECAL+DHCAL set up from April 2011. 97

List of Tables

5.1 Summary of the number of layers and thicknesses in radiation lengths X_0 and nuclear interaction lengths λ_I for the DHCAL structures. Obtained from [24]. 33

6.1 Summary of testing periods with DHCAL at the Fermilab Test Beam Facilities. Obtained from [24]. 38

6.2 Summary of available test runs and number of events for each beam energy in the June 2011 testing period. 39

6.3 Summary of available test runs and number of events for each beam energy in the April 2011 testing period. In the full data sample only eight test runs contained ECAL data: one for 50 GeV, the five 60 GeV test runs, and two 120 GeV test runs. 39

6.4 Set of particle ID cuts for the June 2011 testing period. 51

6.5 Set of particle ID cuts for the April 2011 testing period. 54

6.6 Set of particle ID cuts for late showering pions in energies of 40 GeV and below in the April 2011 testing period. 54

7.1 Distribution of number of muon events for the April 2011 test runs. 56

7.2 Results for the misalignment parameters of the original muon tracks. The data points represent the averages of the alignment parameters from all tracks in the same test run. All runs belong to the April 2011 testing period. All errors are purely statistical. The average for the 60 GeV runs was weighted by their number of events to properly compare to the 50 GeV results. 60

7.3 Systematic errors from the misalignment parameters before moving DHCAL for each analyzed run. The average for the 60 GeV runs' systematic errors was weighted by their number of events. 61
7.4 Results for the alignment parameters of the muon tracks after moving the DHCAL with respect to the Si-W ECAL using the results from Table 7.2. All runs belong to the April 2011 testing period and correspond to the same events used for Table 7.2. The average over the 60 GeV runs was weighted by their number of events. 64
7.5 Systematic errors from the alignment parameters after moving DHCAL for each analyzed run. The average over the 60 GeV runs was weighted by their number of events. 65
7.6 Results for the alignment parameters from the Global Fits to the moved Si-W ECAL+DHCAL muon tracks. All runs belong to the April 2011 testing period. The average over the 60 GeV runs was weighted by their number of events. 67
7.7 Systematic errors from the alignment parameters of Global Fit for each analyzed run. The average over the 60 GeV runs was weighted by their number of events. 67

8.1 Linearity results for June 2011. The parameters p0 and p1 represent the variables constants from Equation 8.2 and were obtained by performing a fit to the data of Figures 8.4a and 8.4b. 75
8.2 Linearity results for April 2011. The parameters p0 and p1 represent the variables constants from Equation 8.2 and were obtained by performing a fit to the data of Figure 8.5. 76

9.1 The X and Y values are the intersections with horizontal and vertical axes for all available energies respectively. The correction factors used to calculate the energies of both detectors are also shown. The first row shows the parameters calculated for the 50 GeV test run, the second run shows averages of the parameters from the four 60 GeV test runs studied, and the last row shows the averaged parameters from the two 120 GeV test runs. . 85

9.2 Energy resolution results for positrons and pions of the June 2011 testing period. The blank spaces represent energies which could not be fitted to Gaussian function properly. These energies were therefore excluded from the analysis. 88

9.3 Energy resolution parameters of the June 2011 testing period for positrons and pions. 90

9.4 Energy resolution results for the Si-W ECAL + DHCAL system in the April 2011 test period from the diagonal fit method. The parameters b and c were set to zero. 92

9.5 Energy resolution of the combined Si-W ECAL+DHCAL system for early showering pions in the April 2011 period, obtained from the sum of energies method. The parameters b and c were set to zero. 92

9.6 Energy resolution results for late showering pions in the April 2011 testing period. Results are shown for both energy conversion methods. 95

9.7 Results for the energy resolution of pions in the two analyzed testing periods for all energy conversion methods. Only the energies 50 GeV, 60 GeV and 120 GeV are compared. The Marker column on the Table represents the markers of the data points in Figure 9.16. 96

9.8 Fit parameters from the fit of Equation 9.7 all the data points in Figure 9.16. The parameter b was set to zero for all fits. All the results in the table correspond only to hadronic showers. **This fit was performed with only three data points*. 98

9.9 Percentile difference between the data points of energy resolution for 50 GeV, 60 GeV and 120 GeV for pions in all studied testing periods and methods. . 98

9.10 Percentage of events discarded from each run by the DHCAL containment condition cut. All the events are hadronic events from the April 2011 sample. 99

9.11 Systematic errors associated to the containment cuts for in the energy resolution study for the April 2011 testing period. 99

Chapter 1

Introduction

The field of experimental particle physics emerged from the discovery of elementary particles in the 1800s. From this time, the development of particle detecting techniques made possible the discovery of even more elementary particles which led to the formulation of a field theory to describe their interactions: the Standard Model of Particle Physics. Nowadays, the field of experimental particle physics continues to investigate the building blocks of matter through the innovative designs of particle physics experiments.

In recent decades, human-made particle accelerators such as the Large Hadron Collider (LHC) have made it possible to complete the experimental detection of every particle in the Standard Model, culminating in the discovery of the Higgs boson in 2012. This discovery opened a new area of precision measurements of the Standard Model, which requires the construction of new electron-positron colliders.

The International Linear Collider (ILC) is a proposed electron-positron collider designed to perform precision measurements of the Higgs boson at center-of-mass energies up to 1 TeV. The correct interpretation of the physical processes expected to be seen at this collider requires the use of Particle Flow calorimetry. In the particle flow approach, individual particles in jets have to be properly identified from each other to then determine the energies of all the jet particles individually, thus improving the jet energy resolution.

The implementation of Particle Flow Algorithms for jet energy reconstruction requires the construction of high-granularity calorimeters which apart from energy measurements present tracking abilities to a significant degree. Such detectors are being developed by the CALICE Collaboration. Among the many high-granularity calorimeter designs by CALICE, this thesis has as main subjects two in particular: the Digital Hadron Calorimeter (DHCAL) and the Silicon-Tungsten Electromagnetic Calorimeter (Si-W ECAL).

The DHCAL physics prototype has been tested in several test beams at Fermilab and CERN in 2010 and 2011. The final prototype was calibrated in terms of efficiency, multiplicity, and alignment between layers right after construction [1]. A DHCAL configuration without absorbers was tested at low beam energies (below 10 GeV) to study the energy response of the prototype to low-energy positrons [2]. More recently, a study on track segment identification and calibration was performed using test beam data from a 52-layer DHCAL configuration tested at Fermilab [3].

The Si-W ECAL has been extensively tested for calibration and energy response studies at Fermilab and CERN. A $1 \times 1\ cm^2$ cell size physics prototype was jointly tested with CALICE hadron calorimeter prototypes. In April 2011, a joint setup of the DHCAL and the Si-W ECAL was exposed to pions, positrons, and muons at the Fermilab test beam facilities, at energies ranging from 4 to 120 GeV. This thesis presents a study of the alignment between the detectors using muon tracks, as well as the combined energy response of the calorimetry system to pions.

A brief review of the Standard Model and elementary particle interactions will be presented in Chapter 2. This will be followed by Chapter 3, in which the main interactions of particles with matter are explained in a particle detector design perspective. The main characteristics of calorimeters will be stated in Chapter 4, as well as a introduction to high-granularity calorimetry and its importance in high-energy physics.

An introduction to the experimental design and physics program of the ILC will be shown in Chapter 5, including a description of most studied calorimeter designs by the CALICE Collaboration. The chapter will emphasize the description of the DHCAL and Si-W ECAL physics prototypes.

The analysis of the experimental data from the commissioning of the detectors will be presented in Chapters 6 through 9. Chapter 6 will present a summary of the data sample and the methodology used to perform particle identification for the different detector configurations. The misalignment measurement, correction procedures and their results will be explained in Chapter 7. Linearity studies will be presented in Chapter 8. The final part of the analysis will be encompassed in Chapter 9. This will include the calculations of energy deposited in the absorber of the Si-W ECAL, hit-to-energy conversion methodology for the DHCAL and a discussion of the results. Finally, the conclusions on the results and the methodology used will be stated in Chapter 10.

Chapter 2

The Standard Model

2.1 The Start of Particle Physics

Particle physics starts from the need to understand the Universe and what it is made of. The interest in finding the smallest components of matter dates back to the time of Democritus and the Greek atomists [4].

In 1897, J. J. Thomson discovered the electron and determined that it was an essential constituent of atoms. This was the discovery of the first elementary particle, therefore it became the start of particle physics. With a simple experimental setup, Thomson was able to start a new field of experimental physics and measure the first important parameters characteristic of elementary particles, such as the charge-to-mass ratio.

From the discovery of the electron, more questions arose. For example, evidence pointed towards the mass of the electron being very small from the very large charge-to-mass ratio measured, this meant that there were still missing constituents of the atom to account for the atom's neutral charge and greater mass. Thereafter, Ernest Rutherford found the answer to Thomson's missing mass and charge. The discovery of the nucleus happened in the early 1900s. In his experiment, Rutherford fired a beam of α-particles into a sheet of gold and by measuring the deflection of the particles he found that the atom consisted of a small and heavy nucleus. The name proton was given to the nucleus of Hydrogen [4]. The atomic model was finally completed in 1932 with Chadwick's discovery of the neutron.

2.2 The Standard Model

The discovery of the three components of the atom set the ground for more theories of at the time unobserved particles. For instance, particles that could explain the behavior of protons in the atomic nucleus which according to the electromagnetic theory should repel from each other in the close distances of the nucleus. The strong force theory was proposed by Yukawa in 1934, thus explaining the phenomenon.

By the 1960s, the large number of elementary particles had been discovered through detection of cosmic rays, for example the pions and muon [4]. The development of a theory to describe the composition and interactions of this collection of particles was necessary.

The Standard Model of particle physics is a theory that describes the universe using relativistic quantum field theory [5]. In the Standard Model, the fundamental particles are called quarks and leptons. These particles interact with each other by exchanging the force mediator particles called bosons. There are corresponding bosons for each one of the fundamental forces included in the Standard Model. These are the photon for the electromagnetic force, the $W^{\pm}$ and Z^{0} bosons for the electroweak force, and the gluons for the strong force. It is noticeable that the gravitational force being about 34 orders of magnitude weaker than the electroweak force is excluded.

In a more fundamental form, the Standard Model particles are separated into two main groups depending on their spin number, these groups are the fermions and then bosons. The fermions are particles whose spin is half-odd-integer. In terms of spin, bosons are defined as particles with integer spin. Quarks and leptons are subdivisions of fermions.

The charged leptons and the quarks interact with each other through the electromagnetic force, but only those particles with color charge can interact through the strong force. Among the elementary particles, only the quarks and gluons have this type of charge.

All elementary particles are typically organized by their masses and type, as it is shown in Figure 2.1. Apart from the particles listed in the figure, nearly all elementary particles have their corresponding ”antiparticle”. An antiparticle has the same mass and

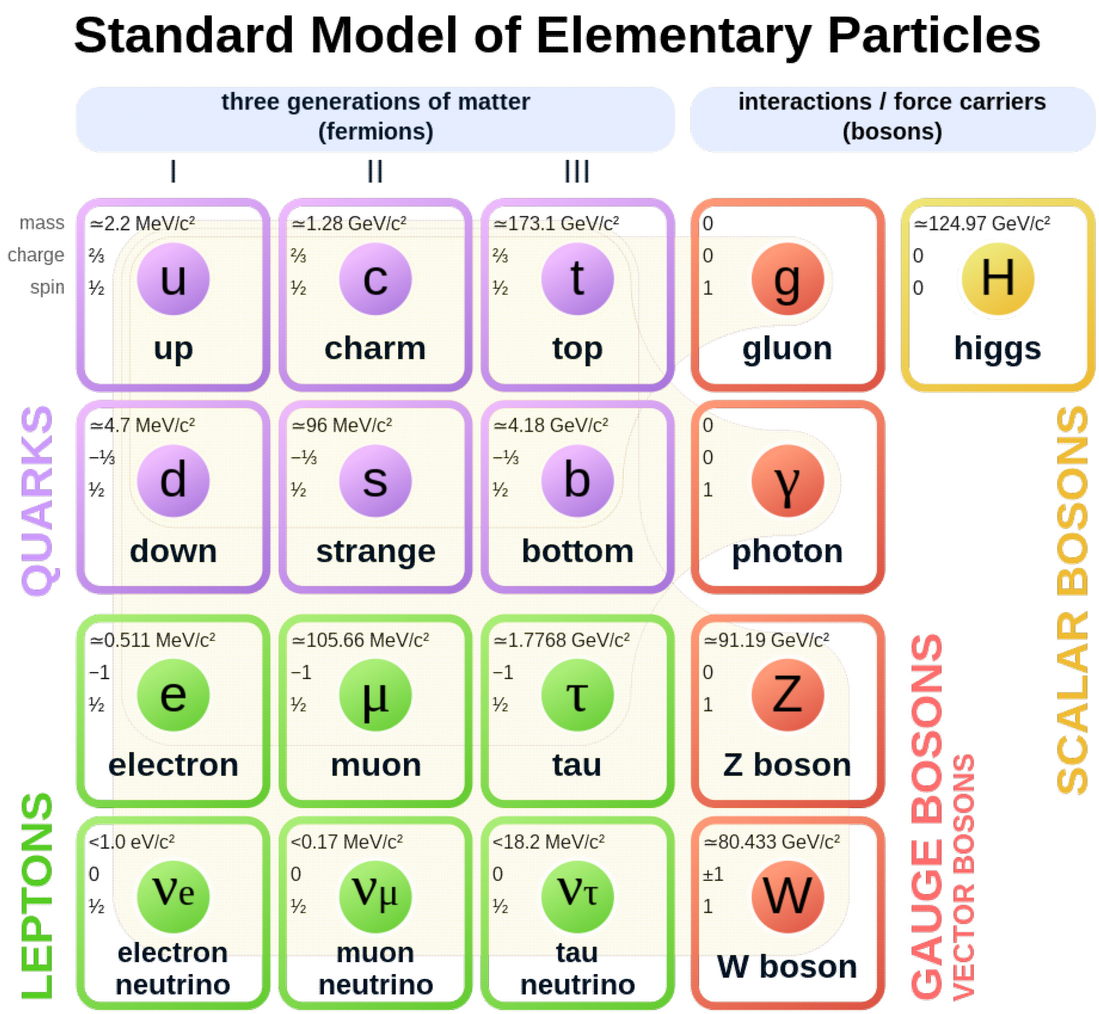

Figure 2.1: Classification of the elementary particles. Quarks (in purple) and leptons (in green) are separated into three generations. The generations go from I to III in mass order, I being the lightest mass and III the heaviest. The bosons are separated by their type, gauge bosons in red and scalar bosons in yellow. The mass, electric charge, and spin are indicated for each particle. The electric charge is in units of e (charge of the electron). Obtained from [6].

spin as a particle but the charge sign is the opposite. The antiparticle of the electron is commonly referred to as the "positron".

Even though every particle of the Standard Model has been experimentally observed, the model is still considered incomplete.

The first and most notorious missing piece is the lack of a quanta for the gravitational field. While all massive particles in the Standard Model interact gravitationally, no proven theory links gravity to a boson to explain these interactions at a quantum level.

A few other elements of the Standard Model are yet to be explained by the theory and verified by experiments, such as the masses of the neutrinos which are predicted to be massless by the model. The Standard Model explains how the masses of particles are generated through the Higgs mechanism, this works for all masses but the neutrino's.

Another phenomenon observed in nature which is not explained by the Standard Model is the presence of Dark Matter in the universe, which is measured to make up for about 27% of the entire universe while regular matter only accounts for 5% [7]. In total, dark matter makes up to 80% of all matter in the universe. The interactions between dark matter and particles of the Standard Model are a current trending topic in theoretical and experimental particle physics.

All of these open questions related to the Standard Model continue motivating the development of new particle physics experiments. Experiments like neutrino observatories and a new generation of particle accelerators need to be equipped with the most up-to-date detectors. Therefore, filling in the gaps of the Standard Model also boosts the development of innovative particle detection techniques.

Chapter 3

Particle Interactions with Matter

Since the discovery of the electron and thus the birth of particle physics, physicists have designed experimental techniques to detect particles and measure their characteristics. This is all to better understand the structure of matter and the interactions of the elementary particles. Of course, all these experiments do is measure some reaction from the particles interacting with the materials of the detector. Therefore it is important to understand the theory behind the behavior of particles interacting with matter. The different elementary particles and their composites act in different manners when interacting with matter. Understanding the following processes is of special importance for the construction of particle detectors and later for the correct interpretation of measurements from any type of particle detector.

3.1 Energy loss of heavy charged particles

Charged particles experience energy loss and deflection of their direction when traveling through matter. These observed effects are primarily caused by elastic scattering from nuclei or inelastic collisions with the atoms of the material [8]. Heavy charged particles, such as the muon, interact with matter mainly through inelastic collisions with the atomic electrons of the material. In this process, the particle transfers energy to the atoms by ionization and excitation. In the ionization process, the charged particle produces free electron-ion pairs. The excitation process refers to the loss of kinetic energy of a particle passing through matter due to the excitation of bound electrons in the material [9]. The photons produced by the de-excitation of atoms can be later measured with a light detector. The measured light will be proportional to the lost energy.

The energy loss dE of heavy particles ($m \gg m_e$) by unit of distance dx can be approximated using the Bethe-Bloch formula [9]

$$-\frac{dE}{dx} = 4\pi N_A {r_e}^2 m_e c^2 z^2 \frac{Z}{A} \frac{1}{\beta^2} \left(ln \left(\frac{2m_e c^2 \gamma^2 \beta^2}{I} \right) - \beta^2 - \frac{\delta}{2} \right), \tag{3.1}$$

where

$\mathbf{N_A}$: Avogadro number

$\mathbf{r_e}$: classical electron radius

$\mathbf{m_e}$: mass of the electron

$\mathbf{z}$: charge of the incident particle in units of electron charge

$\mathbf{Z}$: atomic number of the material

$\mathbf{A}$: atomic mass of the material

$\mathbf{I}$: mean excitation energy of the material

$\boldsymbol{\delta}$: density correction factor

$\boldsymbol{\beta}$: velocity of the incident particle $\beta = \frac{v}{c}$

$\boldsymbol{\gamma}$: Lorentz factor $\gamma = \frac{1}{\sqrt{1-\frac{v^2}{c^2}}}$

The quantity $-\frac{dE}{dx}$ is usually expressed in units of $MeV/(g/cm^2)$. The Bethe-Bloch formula is a function of the kinetic energy of the particle, therefore is commonly plotted for different particles and materials as it is shown in Figure 3.1.

In the non-relativistic range, the loss of energy is dominated by the $1/\beta^2$ term and decreases until a minimum is reached. A particle losing energy at the rate of this minimum is called a Minimum Ionizing Particle (MIP) [8]. Equation 3.1 can be corrected to account

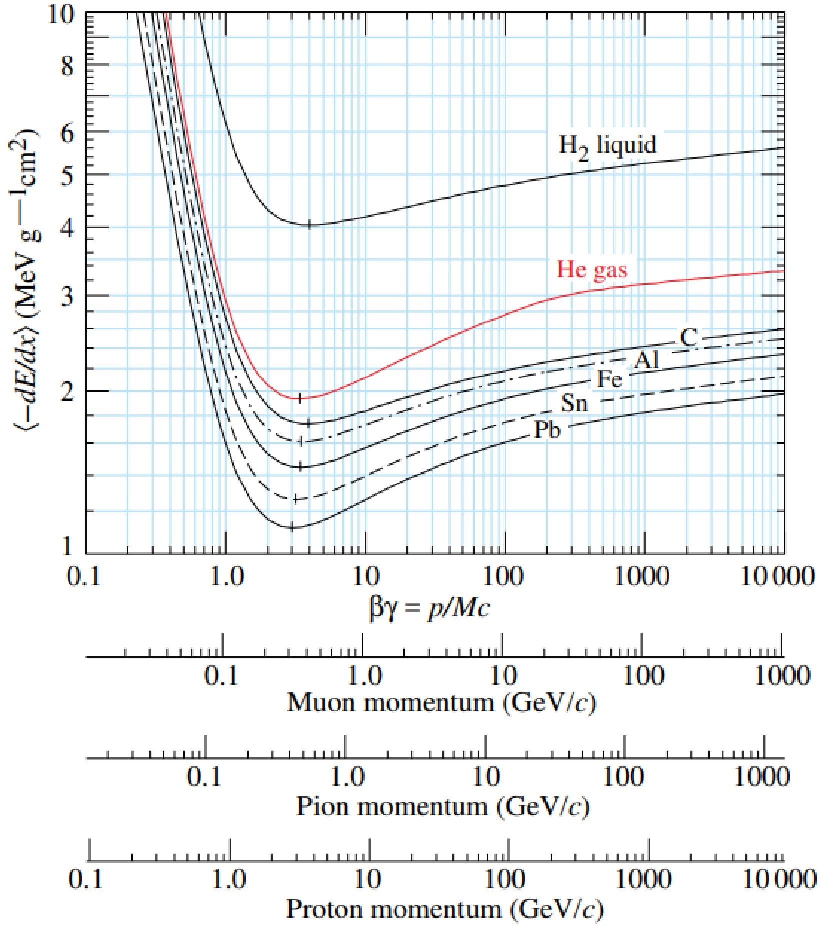

Figure 3.1: Mean energy loss per path length $\langle -\frac{dE}{dx} \rangle$ by ionization and excitation as a function of path length for the muon, pion, and proton in liquid hydrogen, helium gas, carbon, aluminum, iron, tin, and lead. Obtained from [10].

for other energy loss processes at energies lower and higher than the range from the plot in Figure 3.1. For example, the losses at high energies due to radiative processes. The mean energy loss as a function of momenta including low and high energy corrections to the Bethe-Bloch formula is shown for a muon in copper in Figure 3.2 . In the scope of this project, the Bethe-Bloch formula can be used without corrections as it is accurate to a few percent for energies up to hundreds of GeV.

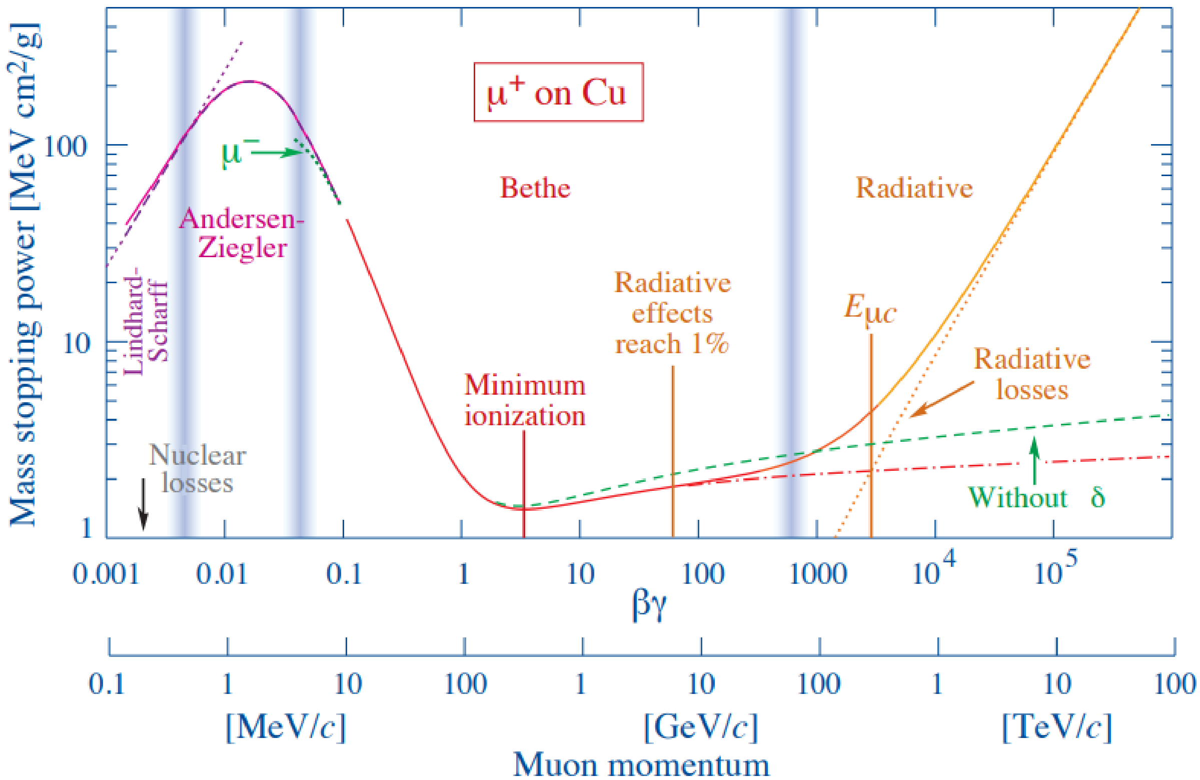

Figure 3.2: Mean energy loss per path length $\langle -\frac{dE}{dx} \rangle$ of μ^+ in copper as a function of the muon momentum. Obtained from [10].

3.1.1 Multiple Scattering

Charged particles are deflected by many small-angle scatters in their path through a material. The total contribution from the multiple processes can be calculated from their cross-sections, resulting in Gaussian distributions for the net scattering [10]. An estimate of the RMS width θ_0 for the multiple scattering can be calculated using the following empirical formula [10]

$$\theta_0 = \frac{113.6\ MeV}{\beta cp} z \sqrt{\frac{x}{X_0}} \left[1 + 0.038 ln \left(\frac{xz^2}{X_0 \beta^2} \right) \right] , \tag{3.2}$$

where p, β, and z are the momentum, velocity, and charge of the incident particle, and x is the thickness of the material in units of radiation lengths. This angle can be calculated for detectors composed of different materials by adding the total number of radiation lengths from the different materials and using Equation 3.2.

3.2 Energy loss of electrons and positrons

In the same way as the heavy charged particles, electrons lose energy due to inelastic collisions with the atomic electrons of the material. The energy loss of electrons and positrons is composed of two processes: radiative losses and collisions. Inelastic collisions dominate at low energies. When increasing the momentum of the incident particle, the energy loss rate reaches a point where the two types of processes contribute equally. This is called the critical energy E_c. At high energies (above E_c), the radiative processes dominate [8].

The radiative process responsible for energy losses of electrons and positrons in matter at high energies is called Bremsstrahlung. This type of radiation is released when the incoming charged particle is scattered in the electric field of a nucleus in the absorber [9].

While the energy loss rate for electrons and positrons by inelastic collisions can be calculated by corrections to the Bethe-Bloch formula, the energy loss by Bremsstrahlung can be approximated by [9]

$$-\frac{dE}{dx} \approx 4\alpha N_A \frac{Z^2}{A} z^2 \left(\frac{1}{4\pi\epsilon_0}\frac{e^2}{mc^2}\right)^2 E\ ln\left(\frac{183}{Z^{1/3}}\right), \tag{3.3}$$

where Z and A are the atomic number and atomic mass of the absorber, and z, m and E are the charge, mass, and energy of the incident particle. From Equation 3.3, it can be concluded that this process is of high importance in the energy loss of electrons due to their small mass.

Equation 3.3 can be simplified for electrons in the following way

$$-\frac{dE}{dx} = \frac{E}{X_0}, \tag{3.4}$$

where X_0 is called the radiation length and it can be approximated as [9]

$$X_0 = \frac{716.4\ A}{Z(Z+1)ln(287/\sqrt{Z})}\ g/cm^2. \tag{3.5}$$

From this definition of X_0, it can be seen that the radiation length is a quantity characteristic of the detector material. By integrating Equation 3.4, we obtain

$$E = E_0 \exp(-x/X_0), \tag{3.6}$$

this equation makes the meaning of a radiation length clearer, as the exponential rate of energy loss of charged particles by radiative processes in terms of distance traveled in the absorber. The quantity X_0 is usually known as the distance needed to be traveled by a particle in an absorber to lose all but $1/e$ of its initial energy E_0 by radiation losses.

3.3 Interaction of photons with matter

The interaction of photons with matter is considerably different from that of charged particles. The main difference resides in the absence of an electric charge from the photon. Photons interact with matter in mainly three ways: Photoelectric effect, Compton scattering, and pair production [8]. All of these processes involve electrons whose characteristics such as energy can be measured to indirectly determine the energy losses by the photon. Compton scattering and pair production are the main processes observed for photons with energies around and above the MeV scale [10].

3.3.1 Compton Scattering

The Compton effect or Compton scattering refers to the scattering of incoming photons with the quasi-free atomic electrons of the absorber. This happens when the photon's energy is higher than the binding energy of the atomic electrons. The binding energy can therefore be neglected and the electrons can are considered quasi-free [8]. For this reason, the effect dominates in the MeV scale. Compton scattering can be represented by the following reaction

$$\gamma + e^- \rightarrow \gamma + e^-, \tag{3.7}$$

In this inelastic collision, the photon has transferred part of its energy ($E_\gamma = h\nu$) to the electron and therefore lowered its frequency ν. The ratio between the resulting energy for the photon produced in the collision E'_γ to the initial energy E_γ can be written as [9]

$$\frac{E'_\gamma}{E_\gamma} = \frac{1}{1 + \frac{E_\gamma}{m_e c^2}(1 - \cos\theta_\gamma)}, \tag{3.8}$$

where θ_γ is the scattering angle of the photon.

3.3.2 Pair Production

Pair production can be represented by the following reaction

$$\gamma \, + \, nucleus \, \rightarrow \, e^+ \, + \, e^- + \, nucleus. \tag{3.9}$$

which pictures the transformation of a photon into an electron-positron pair via the interaction of a high-energy photon with a nucleus. This process has a minimum photon energy set by momentum conservation. For pair production to happen, the incoming photon must at least have an energy equal to the sum of the rest masses of the produced pair of particles plus the recoil energy transferred to the nucleus. This threshold is calculated as

$$E_\gamma \geq 2m_e c^2 \, + \, \frac{m_e^2}{m_{nucleus}} c^2 \, . \tag{3.10}$$

The threshold energy for electron-positron pair production is $E_\gamma = 1.022 \ MeV$. The mean free path for pair production λ_{pair} can be expressed in terms of the radiation length as [8]

$$\lambda_{pair} = \frac{9}{7} X_0 \, . \tag{3.11}$$

3.4 Interaction of hadrons with matter

Hadrons interact electromagnetically through the different mechanisms explained in the past sections. Neutral hadrons are detected through their interaction products when these are charged particles [9]. Apart from this, hadrons interact strongly through elastic and inelastic processes.

In collisions, hadrons produce strongly interacting particles which account for the inelastic part of the total cross-section. To define the interaction of hadrons with matter through inelastic processes it is important to define the absorption of hadrons in an absorber. In a very similar way to electrons (Equation 3.6), this is defined as

$$N = N_0 \exp\left(-x/\lambda_I\right), \tag{3.12}$$

defined in terms of the nuclear interaction length λ_I, the hadronic counterpart of the radiation length. The quantity λ_I can be calculated through the inelastic part of the hadronic cross section as [9]

$$\lambda_I = \frac{A}{N_A\ \varrho\ \sigma_{inel}}\ [cm] \tag{3.13}$$

where ϱ and A are the density in units of g/cm^3 and atomic mass of the absorber, σ_{inel} is the inelastic cross-section given in cm^2, and N_A is Avogadro's number.

3.5 Particle showers

The interaction of particles through matter produces a phenomenon called particle showers or cascades. A shower is started by an incoming energetic particle that produces secondary particles through pair production, bremsstrahlung radiation, or decays and other processes. These secondary particles then produce more particles and so on. The cascades stop when the secondary particles' energy is insufficient to produce more particles. The model of showers is of high importance for high-energy calorimetry. The main aspects of electromagnetic and hadronic showers will be explained next.

3.5.1 Electromagnetic showers

Electromagnetic showers are created by the combined effects of pair production and bremsstrahlung. At high energies, photons traveling through an absorber produce electron-

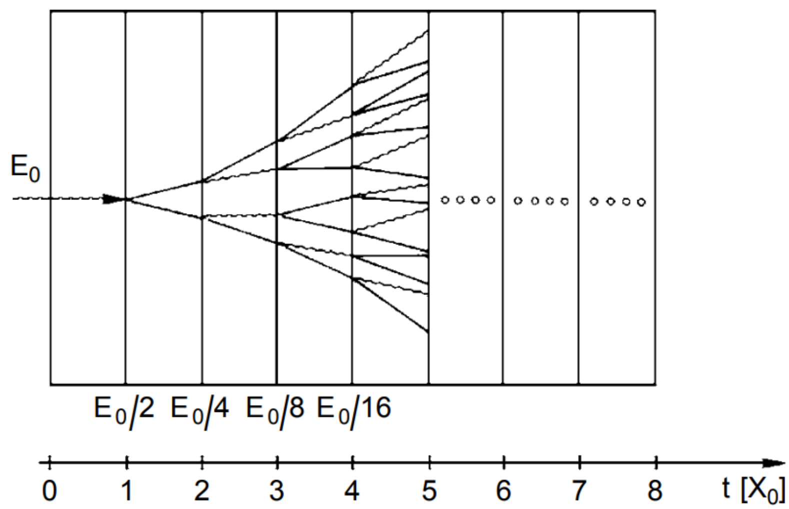

Figure 3.3: Longitudinal development of an electromagnetic shower for several radiation lengths X_0 of absorber material. The energy of the secondary particles is also stated for each step in terms of the initial photon's energy E_0. Obtained from [9].

positron pairs which can then produce bremsstrahlung radiation. If the energies of the secondary photons are high enough, these can transform into electron-positron pairs.

The process continues, given that the energies of the secondary particles are above the critical energy for electrons and the energy threshold for pair production. The repetition of this sequence produces what is called an electromagnetic shower or cascade. The cascade ends after the secondary particles decrease in energy, favoring the loss of the electrons' energy by atomic collisions, and the photons' through the photoelectric effect and Compton scattering [8].

A few of the parameters mentioned in the past sections are of use to describe the behavior of the cascades, such as the radiation length X_0 and the critical energy E_c. It is convenient to express the distances traveled by the particles as $t = x/X_0$. A schematic of the longitudinal development of electromagnetic showers is shown in Figure 3.3. The energies as fractions of E_0 represent the initial energy of the secondary particles. In this simplified process, each electron and positron in a pair have half of the energy of the initial photon. Assuming the symmetric energetic behavior shown for each step of the shower, the total number of particles at distance t can be calculated in the following way

$$N(t) = 2^t \ . \tag{3.14}$$

Then, the energy of the particles at distance t is written as

$$E(t) = E_0 2^{-t} \ . \tag{3.15}$$

Using Equation 3.15, the maximum longitudinal development of the shower can be calculated by setting $E_c = E_0 2^{-t_{max}}$, where t_{max} represents the distance at which the energy of the individual particles reaches the critical energy. Then, the shower maximum is located at

$$t_{max} = \frac{ln(E_0/E_c)}{ln(2)}. \tag{3.16}$$

When an electromagnetic cascade develops in a material, there is a traverse profile associated with the angle between the electron-positron pair, multiple scattering, and the angle of emission of the bremsstrahlung photons. Multiple scattering of low-energy electrons is the main component of the lateral dispersion [11]. The lateral shower profile is then characterized by the Molière radius [9]

$$R_M = \frac{21 \ MeV}{E_c} X_0 \ [g/cm^2]. \tag{3.17}$$

This simple model for the lateral and longitudinal profiles of electromagnetic showers acts as the basis for the design of electromagnetic calorimeters.

3.5.2 Hadronic showers

The longitudinal development of hadronic showers or cascades is determined by the interaction length λ_I. This characteristic distance acts similarly to the radiation length X_0 in the case of electromagnetic showers. A main difference is that the nuclear interaction length tends to be much larger than the radiation length X_0 for most materials commonly used in particle detectors [9]. The thickness of hadronic calorimeters is therefore larger than that of electromagnetic calorimeters of the same material.

Hadrons produce secondary particles through inelastic hadronic processes. The modeling of hadronic showers is much more complex given the wide variety of strongly interacting secondary particles produced. The secondary particles are mainly charged and neutral pions, but other types of hadrons are also produced [9]. About a third of the pions are neutral pions π^0. These decay into two photons which, given that they have enough energy, can then produce subsequent electromagnetic cascades. According to this, about one third of the energy from the initial hadron is in average deposited into the detector as an electromagnetic shower. Of course, the calculation is much more complicated since the interactions are all of statistical nature and there are wide fluctuations in the electromagnetic components.

Since all hadron cascades have an electromagnetic part to them, the lateral development is in part associated to multiple scattering. However, most of it is due to large transverse momentum transfers in nuclear interactions [9]. These interactions make hadronic showers larger than the electromagnetic ones in the lateral profile.

It is more difficult to define the length of a hadronic shower, given the statistical processes involved. An easier way used to model the longitudinal development for calorimeter designs is to calculate the depth at which 95% of the shower is contained for specific absorber materials. For iron, this distance can be approximated by [9]

$$L(95\%) = (9.4\, ln(E/GeV) + 39)\; cm \tag{3.18}$$

for an incoming hadron of energy E in GeV. The distance L can be scaled for other materials using their nuclear interaction lengths. The lateral containment of 95% of the shower can be approximated as [11]

$$R(95\%) \approx \lambda_I\ . \tag{3.19}$$

Chapter 4

Calorimetry

A calorimeter is a device that measures the energy deposition of particles going through an absorber material. This means that the material must absorb the complete energy from the particle by stopping it in order to measure it. As explained in Chapter 3, high-energy particles lose energy by a variety of processes when passing through matter. The study of these processes makes it possible to measure this energy and use it in different areas of high-energy physics.

When interacting with matter, high-energy photons, electrons, and hadrons produce secondary particle showers, this makes the energy deposition in the material more efficient [9]. The main type of process studied with calorimetry in high-energy physics is the energy deposition of particle showers in different absorber materials. Measuring the energy deposition of particle showers is of high importance for energy resolution studies, as well as for particle identification.

Energy and space resolutions, as well as linearity of the response, are the main properties taken into account for the design of calorimeters. The segmentation of the active material of a calorimeter improves these properties. The spatial resolution of a detector is characterized by the granularity. This resolution is a measurement of the calorimeter's ability to identify two particles in one event [11]. The granularity requirement varies according to the applications of the calorimeter and the physical processes expected to be observed at the experiment. Calorimeters are being designed with increasingly high granularity for each new generation of high-energy experiments. Especially for future e^+e^-

colliders, very high granularity calorimeter prototypes are being developed to improve jet energy resolution. This is a requirement for the physics programs of these future experiments since they are designed to perform precision measurements of high-multiplicity final states [11].

Apart from granularity, the size of the calorimeters is dictated by the specific longitudinal and lateral profiles of hadronic and electromagnetic showers. Full containment of particle showers is expected from the calorimeter design.

In particle physics experiments the calorimeters are usually separated into an electromagnetic calorimeter (ECAL) and a hadronic calorimeter (HCAL), due to the size difference between hadron and electromagnetic showers. It is also possible to combine the two types into one detector.

4.1 Homogeneous calorimeters

Homogeneous calorimeters are a technology in which the full material of the detector acts as both absorber and active medium. These detectors are usually based on scintillators, ionization detectors, and Cherenkov light measurements [9]. The materials mentioned above have long radiation lengths compared to usual absorber materials. To fully contain a high-energy hadronic shower, the length of the detector would have to be very large unless a denser material is used. This is not ideal for high-energy experiments where the calorimeters are encapsulated by the magnet and therefore have to be as thin as possible. As stated before, electromagnetic calorimeters tend to have a smaller number of radiation lengths of thickness than a hadronic one for the same energy range. Therefore, the homogeneous type of detector is most commonly used for electromagnetic calorimeters [11] rather than for hadronic calorimeters. Homogeneous calorimeters are the most precise type for the measurements of electromagnetic showers. The granularity of homogeneous calorimeters is restricted by the read-out systems. These detectors are of high volume, therefore a high spatial segmentation highly increases the total number of read-out channels.

4.2 Sampling calorimeters

Even if on one hand, using the full material of a calorimeter as an absorber and active medium gives an excellent energy resolution, the requirements (size and cost) for calorimeters in high energy physics strongly favors the use of calorimeter designs with alternating layers of active media and absorber [9]. This type is called a sampling calorimeter. This design allows using absorber materials with short radiation lengths, cutting on the thickness and overall cost of the detector. The energy of the shower is measured at fixed intervals using an active material. The sensitive layers of sampling calorimeters are usually ionization detectors, such as plastic scintillators, liquid argon, multiwire proportional chambers, or gas [11]. Sampling calorimeters perform direct energy measurements only of a small fraction of the particle showers, through the deposition of energy in the sensitive area. The energy deposition in the absorber can be reconstructed with this information after a suitable calibration using test beams or in-situ methods. Another one of the main advantages of sampling calorimetry is that high granularity is more easily achievable, as only the active area has to be segmented.

Chapter 5

The international Linear Collider and CALICE Calorimeters

As seen in the past chapters the discovery of the first three subatomic particles: the electron, proton and neutron, gave rise to the creation of experimental methods for their studies. In the same matter of importance as is detecting the subatomic particles, there is the matter of producing them. Notably, the first subatomic particles other than the components of the atom were found by detecting cosmic rays. This was the case for the muon for example, as well as several mesons such as the pion. Physicists began discovering more and more elementary particles, and therefore, started to build theories to explain their interactions. After discovering the so-called "Zoo of particles", experimental particle physicist started to build particle accelerator experiments to produce heavier particles and measure their characteristics. An example was CERN's Super Proton Synchrotron (SPS) Proton-Antiproton Collider, in which the bosons $W^{\pm}$ and Z^{0} were discovered in 1983 [12, 13]. The most recent boson discovered was the Higgs boson in 2012 at CERN's LHC [14].

Some collaborations are now focusing on the area of precision measurements of the Standard Model. This area proposes a new generation of electron-positron colliders to study the Higgs boson and top quark at a precision that cannot be achieved at the very high backgrounds of hadron colliders [7]. The International Linear Collider is an $e^{+}\,e^{-}$ accelerator proposed to be built initially to perform precision measurements of the already discovered Higgs boson and to potentially discover new processes beyond the Standard Model.

5.1 The International Linear Collider

The ILC is a proposed linear electron-positron collider at high luminosity. The design has an initial center-of-mass energy of 200 to 500 GeV to ensure the production of the Higgs boson. The center-of-mass energy will be extendable to 1 TeV [7]. The main subsystems of the ILC are:

- A polarized electron source, producing an electron beam by illuminating a photocathode in a Direct Current (DC) gun using a laser.
- A polarized positron source delivering positrons obtained from the electron-positron pair production of high-energy photons created by passing the main electron beam through an undulator.
- Two $3.2\ km$ circumference electron and positron damping rings.
- Two main $11\ km$ linear accelerators with 1.3 GHz superconducting radio-frequency accelerating cavities producing $1.6\ ns$ long pulses.
- Two $2.2\ km$ long beam-delivery systems to bring the beams into collision with a $14\ mrad$ crossing angle.
- A single interaction point occupied by two detectors in a ″push-pull″ system to be used one at a time while the other detector is accessible for maintenance and upgrades.

A schematic view of the full ILC complex with positioning and sizes of the mentioned subsystems can be found in Figure 5.1.

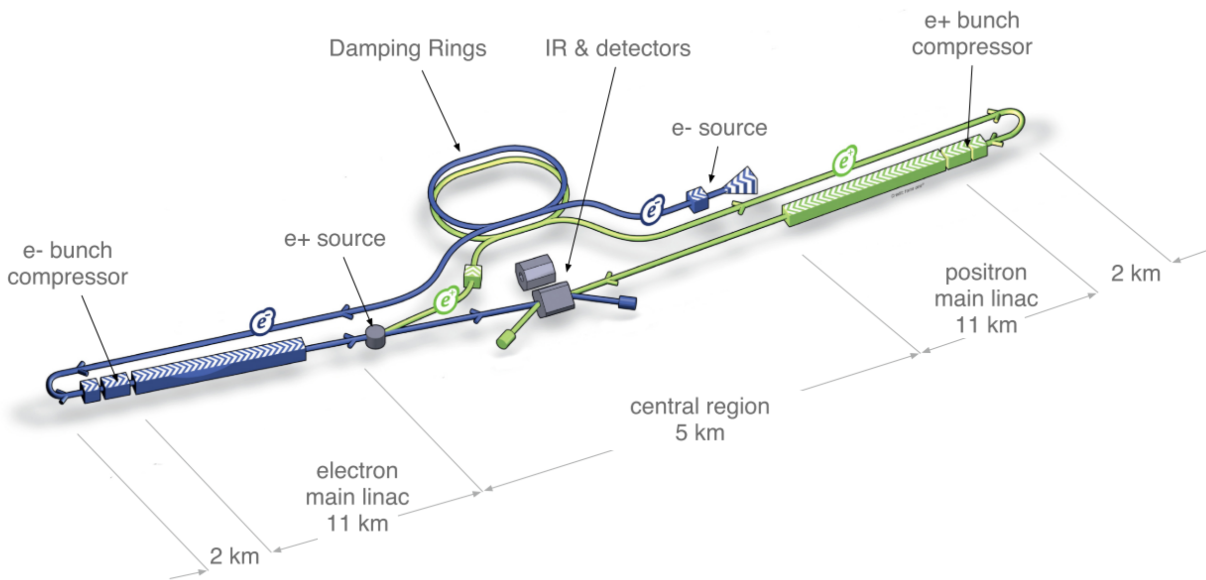

Figure 5.1: Schematic layout of the ILC. Obtained from [7].

5.1.1 Particle Flow Algorithm

A Particle Flow Algorithm (PFA) calorimetry is a technique developed for the improvement of the jet energy reconstruction in high-energy physics experiments. The technique refers to the proper association of energy deposits from the calorimeter system to the charged particle momenta from the tracker and separating them from the energy deposits created by neutral particles [15]. The separation of the neutral and charged particles' energies allows for a more precise energy measurement of jets.

The main limiting factor of this technique is confusion between energy deposits from individual particles within the calorimeter. This motivates the development of high-granularity calorimeter systems. These calorimeters have imaging capabilities similar to those of the tracker, therefore allowing for the reconstruction of the four-vectors of most visible particles in an event [16]. The jet energy can be reconstructed by adding the individual energies of all the particles. PFA energy reconstruction techniques can be used to achieve jet energy resolutions of 3-4% at the ILC [7]. The typical stochastic term of the energy resolution for traditional hadronic calorimeters ($\geq 55\%\sqrt{E/GeV}$) is not enough to achieve the desired jet energy resolutions. These resolutions are more likely to be achieved with the use of hadronic calorimeters with a stochastic term $\leq 30\%\sqrt{E/GeV}$, something only possible with the use of high-granularity calorimeters [16].

5.1.2 Experiments for the International Linear Collider

The ILC is designed to allow the use of two experiments. The two experiments will share one interaction region through a ”push-pull” configuration, therefore, they will not take measurements simultaneously. The two-detector approach was thought of as a way to cross-check and confirm results while reducing costs with the two detectors using the same interaction point [7]. A summary of the description of the two experiments follows.

SiD

The Silicon Detector (SiD) is a multi-purpose experiment designed specifically for precision measurements at the ILC. The detector system consists of a silicon pixel vertex detector, a silicon tracker, a silicon-tungsten electromagnetic calorimeter and a highly segmented hadronic calorimeter [7]. The use of mainly silicon throughout the subsystems of the SiD ensures robustness to beam backgrounds, a high charged-particle momentum resolution, and compactness of the detector [7]. The full tracking and calorimetry systems are contained within a 5 T field strength solenoid. A scintillator-based muon identification system surrounds the magnet. The tracking and calorimetry systems are designed to be used within the PFA approach. A quadrant section of the traverse profile of the SiD detector can be seen in Figure 5.2.

ILD

The International Linear Detector (ILD) concept consists of a high precision vertex detector, tracking detectors based on silicon with a time-projection chamber, an electromagnetic calorimeter, and a hadronic calorimeter. These detectors are located inside a 3.5 T solenoid [7]. An iron return yoke is set on the outside of the solenoid as a muon system and tail-catcher calorimeter. Figure 5.3 shows the quadrant view of the ILD detector.

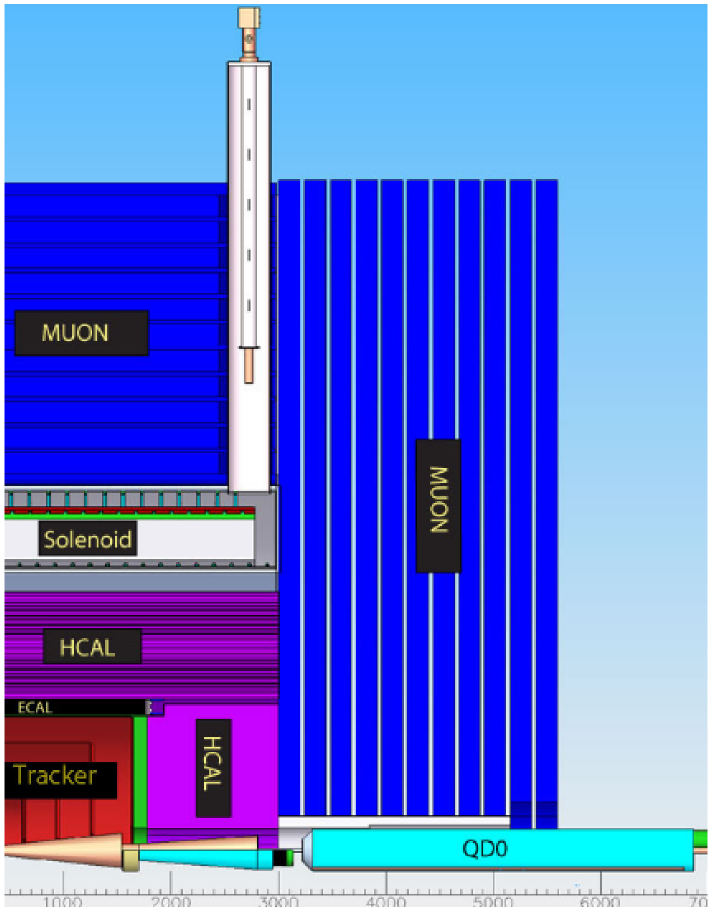

Figure 5.2: Profile view of the SiD detector describing the positioning of the main subsystems of the experiment. Obtained from [7].

The electromagnetic and hadronic calorimeters designs emphasize high granularity, both longitudinal and transverse [16]. This makes the detectors optimal for the use of PFA.

5.2 CALICE Calorimeter prototypes for ILC

Calorimetry represents one of the main concepts of experimental high energy physics. The study of the energy of particles is of fundamental importance for future particle physics experiments. Future electron-positron colliders offer the possibility of measurements with unprecedented precision levels. Therefore, the detectors' performances are constrained by specific requirements to accurately perform the measurements [15]. The

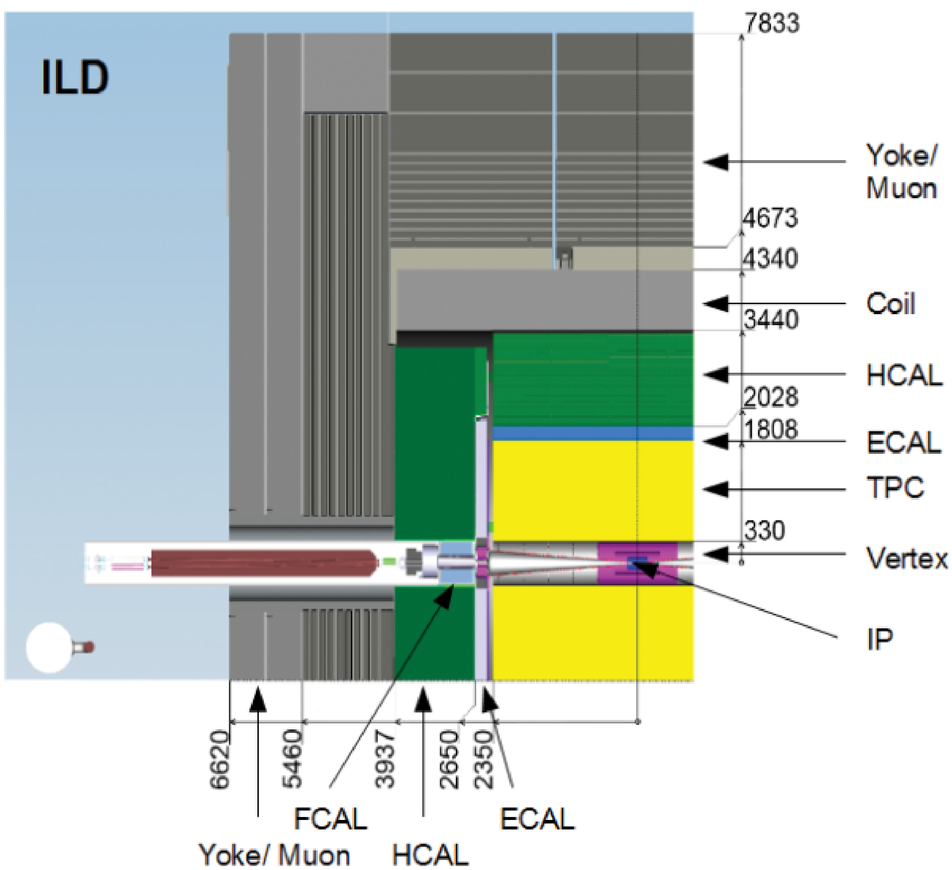

Figure 5.3: Profile view of the ILD detector describing the positioning of the main detector systems as well as the coil. All measurements are in millimeters. Obtained from [7].

requirements to achieve high precision measurements push R&D collaborations to come up with new detector technologies.

Calorimetry oriented toward Particle Flow Algorithms promises to deliver unprecedented jet energy resolution for future high-energy colliders [16]. The application of the Particle Flow approach to the experiments at the ILC introduces new challenges to the area of calorimetry, by imposing the finest possible lateral and longitudinal segmentation. Therefore, the detector designs require detection techniques suitable for high segmentation.

The CALICE Collaboration was originally dedicated to the calorimetry at the ILC. The start of the construction phase of the ILC is still waiting to be approved, therefore the CALICE Collaboration has now expanded its reach to the development of generic high-

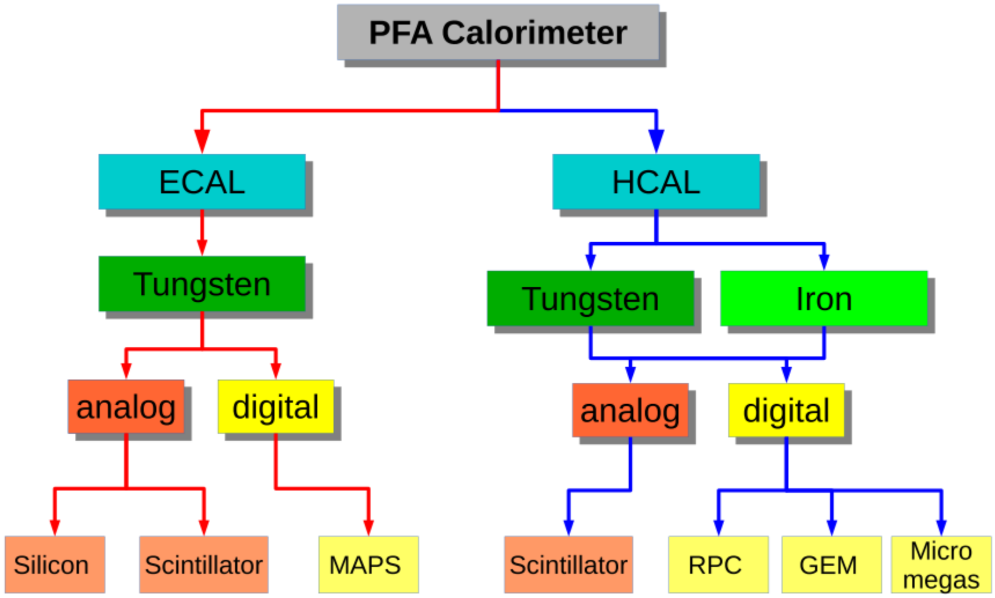

Figure 5.4: Conceptual map of calorimeter technologies for PFA Calorimeters. Obtained from [15]

granularity calorimetry. The main signature of the CALICE Collaboration is the design of high-granularity calorimeters with which particle flow algorithms can be implemented. One of the goals of the calorimeter design in CALICE is to achieve an energy resolution sufficient to separate W and Z bosons' hadronic decays [16]. Another advantage of highly granular calorimeters is the possibility to perform particle identification with tracking techniques.

A number of calorimeter candidates are being developed by the CALICE collaboration. The electromagnetic and hadronic calorimeters designs by CALICE are all sampling calorimeters with either tungsten or iron for the absorber layers. The designs use a variety of detection techniques, such as scintillators, silicon, and gas. The concept map in Figure 5.4 shows all studied options in calorimetry technologies for the implementation of PFA. In this map, options for analog or digital calorimetry are connected to their associated suitable detection technologies.

The main characteristics of the detectors developed by CALICE will be explained in the following subsections of this chapter. Greater emphasis will be put into the description of the DHCAL and the Si-W ECAL as they are the subject of this thesis.

5.2.1 AHCAL

The Analogue Hadron Calorimeter (AHCAL) is a design proposed by the CALICE Collaboration. A physics prototype of the AHCAL was completed in 2007 and put to test using the test beams at DESY and CERN [17]. The tested design had 38 steel absorber layers, each $17.4\ mm$ in thickness. The active layers consisted of scintillator tiles with dimensions of $3 \times 3\ cm^2$ in a $30 \times 30\ cm^2$ central core region. Outside of the core, there were three rings of $6 \times 6\ cm^2$ tiles, followed by a final $12 \times 12\ cm^2$ tile ring. The placement of the different tile sizes can be better observed in Figure 5.5. All tiles had a thickness of $5\ mm$. Each $6 \times 6\ cm^2$ and $12 \times 12\ cm^2$ tile had a circle carved into it in which a wavelength shifting optical fiber was inserted. In the case of the $3 \times 3\ cm^2$ tiles, only a quarter a the circle was carved since the minimum bending radius was too large to achieve a full circle without losing the light signal. The scintillation light was collected by the fiber,

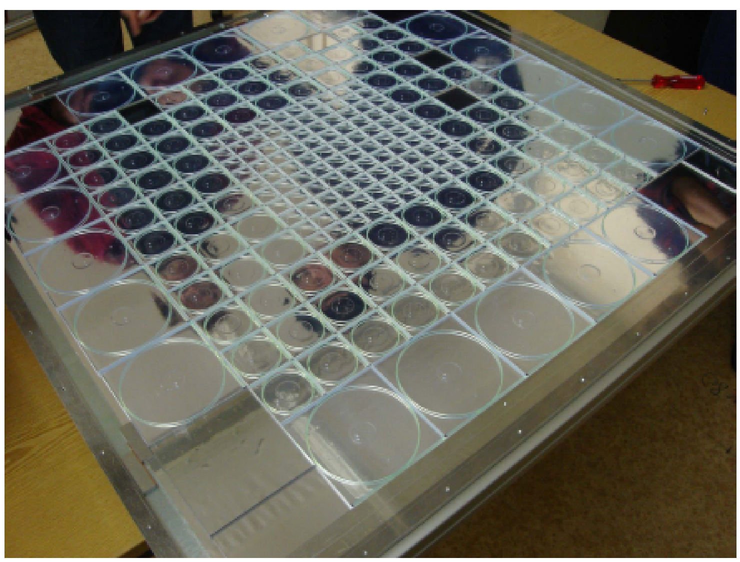

Figure 5.5: Example photograph of the segmented active layer for the AHCAL physics prototype. The circular shapes show the carved regions in which the optical fibers were inserted. Obtained from [17].

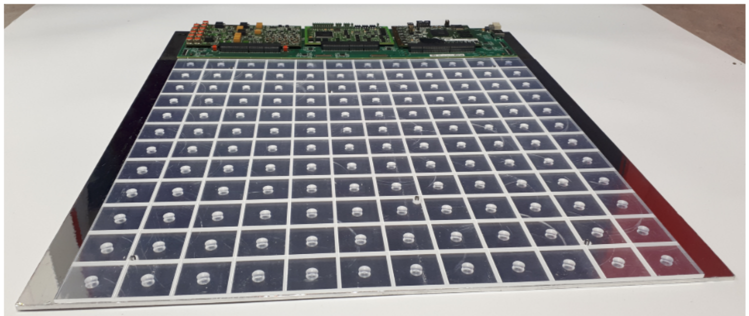

Figure 5.6: Example photograph of the segmented active layer before wrapping for the AHCAL technological prototype. Obtained from [20].

wavelength shifted, and then sent to a Silicon Photomultiplier (SiPM). An initial intrinsic energy resolution of this prototype for pions was found to be $\sim 58\%/\sqrt{E/GeV}$ [18]. From 2017 to 2018, a technological prototype was built after the successful testing of the physics prototype [19]. The technological prototype has a few differences with respect to the physics prototype. One of them is the use of in-tile SiPMs for readout. Although this removes the need for optical fibers, each tile has to be individually wrapped with a reflective foil to guide the light into the SiPM [20]. The size of the cell throughout the active layers also varies from one prototype to another, with the technological prototype having a $30 \times 30 \times 3\ mm^3$ cell size all over. Figure 5.6, shows the scintillator tiles for an active layer before wrapping, the small circles in the center of each tile are actually small cavities for the placement of the SiPMs .

Other designs for the active layers are being studied by the AHCAL groups in the CALICE Collaboration. The alternatives aim at easing the assembly of the readout and still ensure the high lateral segmentation of the AHCAL.

5.2.2 SDHCAL

The Semi Digital Hadron Calorimeter (SDHCAL) is an alternative hadron calorimeter proposed by CALICE. This design uses Glass Resistive Plate Chamber (GRPC) as sensitive medium with embedded readout electronics. A technological prototype was built and has been tested in several test beam campaigns.

The active layer of the prototype has about $1\ m^2$ in area and the produced ionization is read out by 96×96 copper pads of $1\ cm^2$ area connected to the electronics [21]. Steel plates were used for the absorber layers. The cells of the detector record energies based on three charge thresholds. For this prototype, the thresholds were $110\ fC$, $5pC$, and $15pC$ which respectively correspond to one, few, and many charged particles going through the pad in an assigned time interval [21]. This readout only requires a 2-bit signal per channel.

The three threshold approach reached an energy resolution of 7.7% at 80 GeV for hadronic showers of the data-taking period at CERN's test beam [22].

5.2.3 DHCAL

The Digital Hadron Calorimeter is a Resistive Plate Chamber (RPC) based calorimeter developed by the CALICE Collaboration as a PFA-optimized calorimeter.

Design description

The DHCAL is a sampling calorimeter, which alternates RPCs and absorber plates to measure the energies of hadronic showers. The absorber plates chosen for the prototype were either tungsten or steel, depending on the testing site.

An active layer of the DHCAL consists of three separated RPCs with dimensions of $32 \times 96\ cm^2$, placed vertically on top of each other. Therefore, the full active area of one layer is $96 \times 96\ cm^2$. Each layer has 9216 $1 \times 1\ cm^2$ pads on the back of the RPC for readout, similar to the SDHCAL. A total of six readout boards contain the readout pads and Front-End electronics [23]. The three RPCs were contained inside a cassette structure along with the six readout boards, this facilitated the transportation process and provided protection during installation [24].

Readout Format

Each readout cell on the detector was set to a single threshold of $180\ fC$, giving the detector its signature digital readout. The threshold is set to measure only the passage of a particle in the gas gap. The cells do not record any measurement of the energy deposited.

A "hit" is defined as a cell recording a particle passing through it. The digital calorimetry concept estimates the energy of a full particle shower by counting the total number of hits recorded in an event.

The data recorded by the DHCAL is presented in the following format for each hit:

$$t \ x \ y \ z$$

where t is the timestamp of the hit signal, x and y are the hit pad coordinates, therefore going from 0 to 95, and z is the layer coordinate of the hit.

Testing configurations

A physics prototype was built between 2008 and 2010 and was later used at Fermilab and CERN. The configurations tested at the two sites varied in numbers of layers and absorber materials.

The configuration tested at Fermilab in 2011 consisted of two structures. First, a 38-layer structure of RPCs with $17.4\ mm$ thick steel plates. This is called the Main Stack. The distance between layers in the Main Stack was $3.17\ cm$.

A second separated structure consisted of 14 RPC layers. The first eight layers are separated by $2\ cm$ thick steel plates and the rest by $10\ cm$ thick steel plates. This structure is set at the back of the Main Stack and it acts as a Tail Catcher and Muon Tracker (TCMT). The TCMT was placed 40.1 cm after the last layer of the Main Stack to allow rotating space for the Main Stack.

The two structures have the same RPC design for the active layers, therefore maintaining the same lateral granularity throughout the detector.

Another structure was used for data taking. This one consisted of 50 layers of RPCs without absorber plates. The cassettes with the RPCs were placed at a $2.54\ cm$ distance from each other. This configuration is referred to as the Minimal Absorber DHCAL (MinDHCAL). This configuration was used for measurements of low energy positrons [2].

Structure	Number of Layers	Thickness in X_0	Thickness in λ_I
Main Stack (Fe)	38	48.6	5.23
TCMT	14	47.3	5.00
MinDHCAL	50	14.4	1.69

Table 5.1: Summary of the number of layers and thicknesses in radiation lengths X_0 and nuclear interaction lengths λ_I for the DHCAL structures. Obtained from [24].

Final setups of the described structures can be observed in Figure 5.7. The thicknesses of the three structures in terms of radiation lengths and nuclear interaction lengths are stated in Table 5.1.

Preliminary results for the energy resolution of DHCAL show an energy resolution of $\sim 24.9\%/\sqrt{E/GeV}$ for positrons and $\sim 55\%/\sqrt{E/GeV}$ for pions [15]. This thesis focuses on the Main Stack + TCMT configuration with steel plate absorbers used in the April 2011 and June 2011 testing periods at Fermilab.

5.2.4 ScECAL

The Scintillator strip-based ECAL (ScECAL) is one of ECAL proposals for the ILC by the CALICE Collaboration. This calorimeter is the first one of its kind, using high-granularity plastic scintillator strips [25]. It is a cheaper alternative to the silicon-based electromagnetic calorimeters also studied by CALICE.

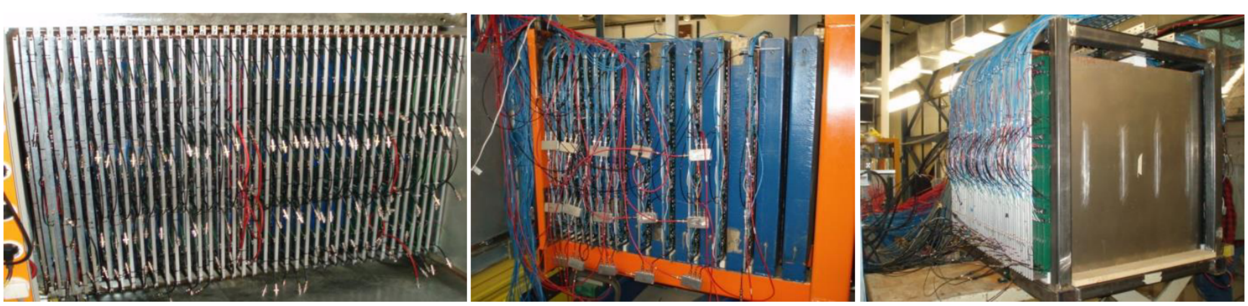

Figure 5.7: DHCAL Configurations obtained from [24]. On the left: Main Stack before cabling, in the middle: TCMT, and on the right: the MinDHCAL.

Tungsten was chosen as the absorber material for the design. The short Molière radius of tungsten is of high importance for the implementation of PFA to separate particle showers effectively.

A first prototype consisting of 26 scintillator-tungsten layers was constructed in 2007 [25]. The active element of one layer was formed by two plastic scintillator ”mega-strips” with dimensions of $45 \times 90\ mm^2$. Each mega-strip consisted of a $3\ mm$ thick plate separated into nine strips measuring $45 \times 10\ mm^2$ in area. The individual strips were created by drilling their shape into the mega-strip tile and then inserting Polyethylene terephthalate (PET) film between grooves to optically isolate the strips. The mega-strip design presents optical cross-talk between strips. Although this complicates the reconstruction of the events, the mega-strip was still used to ease any future production of a large-scale detector with millions of channels [25]. The scintillation light of each strip is measured by an individual on-strip Multi Pixel Photon Counter. The scintillator layers were placed in two alternating orientations to achieve a granularity of $10 \times 10\ mm^2$ [25]. The prototype was tested at energies of 1 to 6 GeV using positron beams at the DESY-II electron synchrotron. The energy resolution of the prototype was studied for this beam energy range and it was found to be between $13\%/\sqrt{E/GeV}$ and $14\%/\sqrt{E/GeV}$ [25].

5.2.5 Si-W ECAL

The Silicon-Tungsten Electromagnetic Calorimeter is one of the most extensively studied ECAL designs by the CALICE Collaboration. It is a high-granularity silicon-based detector with tungsten plates as absorbers.

Design description

The first Si-W ECAL prototype finalized was the so-called physics prototype [26]. It consisted of sampling layers with an active area of $18 \times 18\ cm^2$. The active area of a layer was separated into nine 6×6 cell readout boards. The silicon-based cells had an area of $1 \times 1\ cm^2$ and a thickness of $525\ \mu m$. The nine readout boards were separated into two modules, a bottom one made out of a row of three readout boards, and a top one with 3×2 boards.

The detector had a total of 30 active and passive layers which, at normal incidence, corresponded to 24 radiation lengths (X_0) and 0.8 nuclear interaction lengths (λ_I). Tungsten was chosen as the ideal absorber material for the ECAL due to its short radiation length and small Molière radius. These two characteristics ensured compact electromagnetic showers. The chosen absorber also has a large ratio of interaction length to radiation length, which makes hadronic and EM showers easier to be resolved from one another by their length [16]. The 24 radiation lengths design of the detector ensured the containment of 99.5% of 5 GeV electron showers and more than 98% for 50 GeV showers [26].

The tungsten plates varied in thickness along the layers as follows: first, ten layers of $1.4\ mm$ ($0.4\ X_0$) thickness, followed by ten $2.8\ mm$ ($0.8\ X_0$) thick layers, and lastly another ten layers with a thickness of $4.2\ mm$ ($1.2\ X_0$). The layout of the absorber layers can be seen in Figure 5.8.

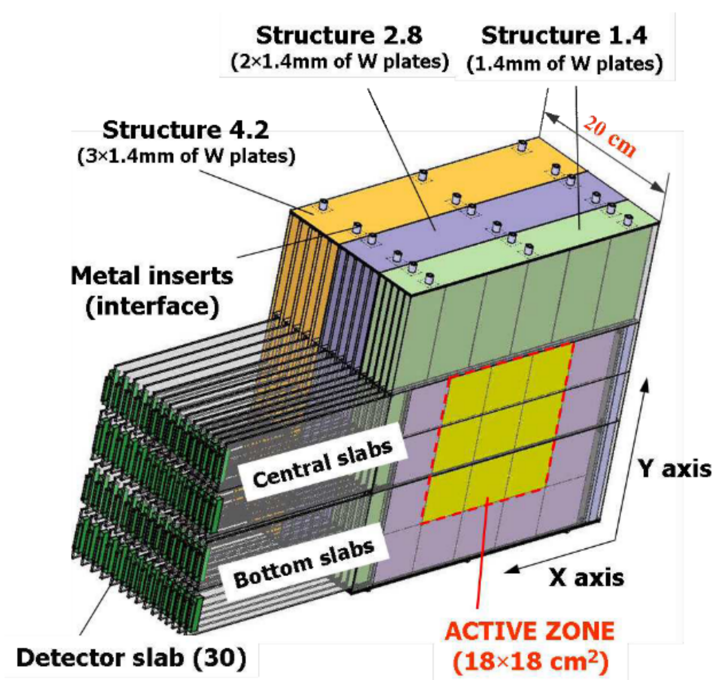

Figure 5.8: Schematic 3D view of the Si-W ECAL physics prototype. Obtained from [26].

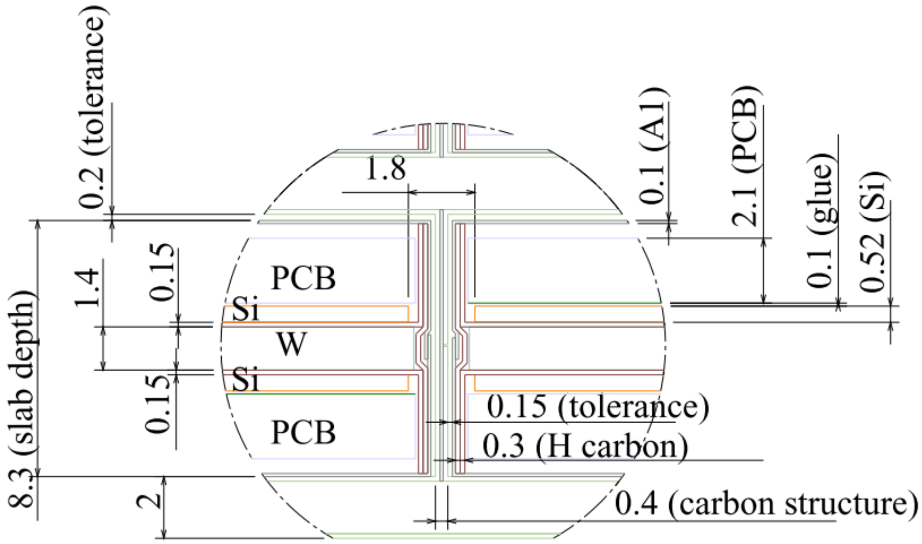

Figure 5.9: Detailed measurements of one ECAL slab, showing an absorber (tungsten) layer sandwiched between two active (silicon) layers. All measurements are in millimeters. The separation between two silicon layers is composed of either only a tungsten layer or of two PCB, carbon structure, and aluminum glue in addition to the tungsten layer. Obtained from [27].

The separation between active layers in ECAL can be found in Figure 5.9. As it can be seen in the schematic shown, the tungsten plate was set between two silicon layers and passive material needed for support of the structure. One of these absorber + active medium + support material structures was given the name of an ”ECAL slab”. Another absorber plate was set between two ECAL slabs.

Testing configurations and results from test beams

The physics prototype has been extensively tested at DESY, Fermilab, and CERN from 2005 to 2011. The ECAL was tested along with CALICE HCALs, such as the DHCAL and AHCAL. In a combined Si-W ECAL Physics Prototype + AHCAL + TCMT testing period, the energy resolution was measured to be $\sim 54.25\%/\sqrt{E/GeV}$ with a constant term of 4.6% [28].

In April 2011, the 30-layer physics prototype was tested in conjunction with the DHCAL Fermilab configuration (see Section 5.2.3). This testing period is the main subject of this thesis. Studies of the energy resolution of the combined Si-W ECAL + DHCAL system, alignment of the detectors, and linearity will be presented.

After the successful tests of the physics prototype, a 7-layer technological prototype with $5 \times 5\ mm^2$ cell size was built. In June 2017 it was tested for calibration at the DESY beam line in the beam energy range from 1 to 6 GeV [29]. The technological prototype has now been expanded to a total of 15 functional layers which were recently tested in test beam facilities at DESY and CERN. The tests took place in 2021 and 2022 and the data collection is currently being analyzed by the CALICE Collaboration [30].

Chapter 6

Event selection and Particle ID

The data studied in this analysis corresponds to two testing periods using DHCAL at the test beam facilities in Fermilab.

In the period from October 2010 to December 2011, the DHCAL had five data-taking periods at the Fermilab Test Beam Facilities. At the time, the Fermilab facilities offered 120 GeV proton beam and secondary beam which were variable in energy, ranging from 1 to 66 GeV [24]. The secondary beam had different particle percentages at different energies. At energies below 6 GeV, the secondary beam was dominated by positrons. The beam presented equal fractions of positrons and pions at a momentum close to 6 GeV. At energies above 32 GeV, pions represent the majority of the beam [24]. Table 6.1 shows

Testing period	**Configuration**	**Combined detector layers**	**Collected μ events**	**Collected secondary beam events**
October 2010	DHCAL	38	1.4M	1.7M
January 2011	DHCAL+TCMT	38+13=51	1.6M	3.6M
April 2011	Si-W ECAL+DHCAL+ TCMT	30+38+14=92	2.5M	5.1M
June 2011	DHCAL+TCMT	38+14=52	3.3M	2.7M
November 2011	MinDHCAL	50	0.6M	1.3M
Total			**9.4M**	**14.4M**

Table 6.1: Summary of testing periods with DHCAL at the Fermilab Test Beam Facilities. Obtained from [24].

a summary of the testing periods with experimental configurations and number of collected events using the primary and secondary beams.

Tables 6.2 and 6.3 show the distribution of events and test runs for the June 2011 and April 2011 testing periods, respectively. The listed number of events are the total data sample used in the analysis of this project.

The main focus of the project corresponds to the data taken in April 2011. In this testing period, the Si-W ECAL prototype and the DHCAL prototype were tested at beam energies ranging from 4 GeV to 120 GeV. The 4 GeV test runs for the April 2011 period

June 2011		
Beam energy (GeV)	**Runs**	**Number of events**
8	5	264770
16	4	312021
32	5	306665
40	8	379803
50	8	336071
60	6	306083
120	9	490413
Total	45	2395826

Table 6.2: Summary of available test runs and number of events for each beam energy in the June 2011 testing period.

April2011		
Beam energy (GeV)	**Runs**	**Number of events**
8	2	506095
12	5	216052
16	4	355449
25	2	183466
32	5	410833
40	5	386994
50	4	390220
60	5	157051
120	3	123693
Total	35	2729853

Table 6.3: Summary of available test runs and number of events for each beam energy in the April 2011 testing period. In the full data sample only eight test runs contained ECAL data: one for 50 GeV, the five 60 GeV test runs, and two 120 GeV test runs.

were removed from the study due to the small number of hadronic events at this beam energy.

The second data set was taken in June 2011. This testing period includes a DHCAL-only experimental setup. The June 2011 data was mainly analyzed for a comparison of the performance of DHCAL with and without the presence of an electromagnetic calorimeter. This testing period was chosen due to its similar setup and closeness in time to the April 2011 period.

After analyzing the data, it was observed that in some of the available test runs some sections of the layers were either counting a large number of hits or not recording any hits throughout the run. Therefore, a ”good” test run was selected to be a run without noticeable faulty layers on either detector. The faulty layers can be identified as dark and light rectangular sections in the X-Z and Y-Z Distribution of the detectors. For the Si-W ECAL an example of a test run presenting faulty layers can be observed in Figure 6.1. As mentioned in section 5.2, the ECAL layers are composed of two modules set on top of each other vertically. The top module covers two thirds of the sensitive area while the bottom one covers the remaining one third of the area. Each individual faulty module can be observed on the Y-Z Distribution from Figure 6.1.

For all data sets, only good test runs were selected for the study by analyzing a set of plots called Standard Plots. The Standard Plots represent the main aspects of a test run by plotting histograms of various parameters which can be obtained from the data. An example of the Standard Plots set for a 50 GeV DHCAL+ECAL run can be seen in Figures 6.2 and 6.3.

6.1 Run parameters

The run parameters listed below were chosen to represent important characteristics of the events in a test run. The Standard Plots consist of 1D histograms or 2D scatter plots of combinations of these run parameters. These are displayed in Figure 6.2 for the DHCAL.

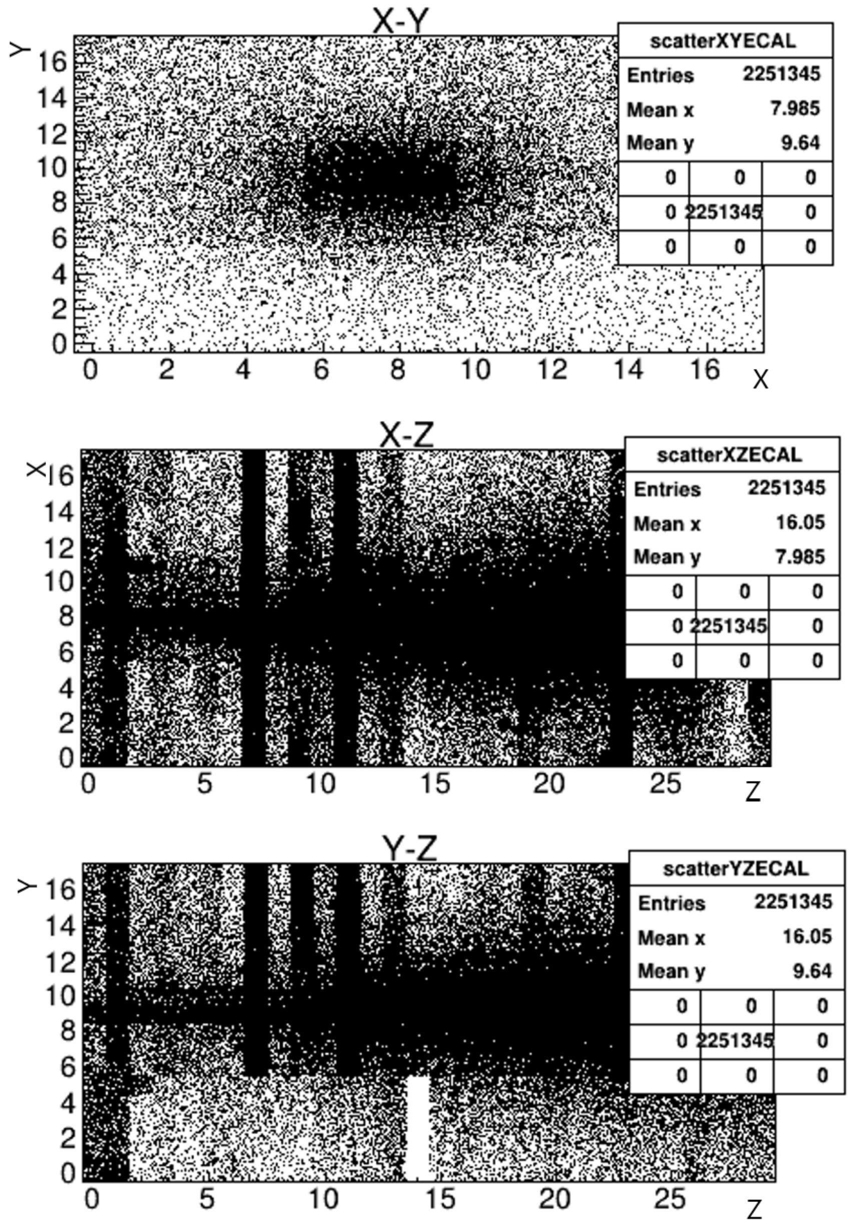

Figure 6.1: Example of the X-Y, X-Z, and Y-Z Distribution Standard Slots for Si-W ECAL for run 630098 at 120 GeV. The scatter plots show many faulty modules which are easily recognizable as light and dark stripes along Z. The light stripe corresponds to modules that were off during the run and the dark stripes to constantly misfiring modules.

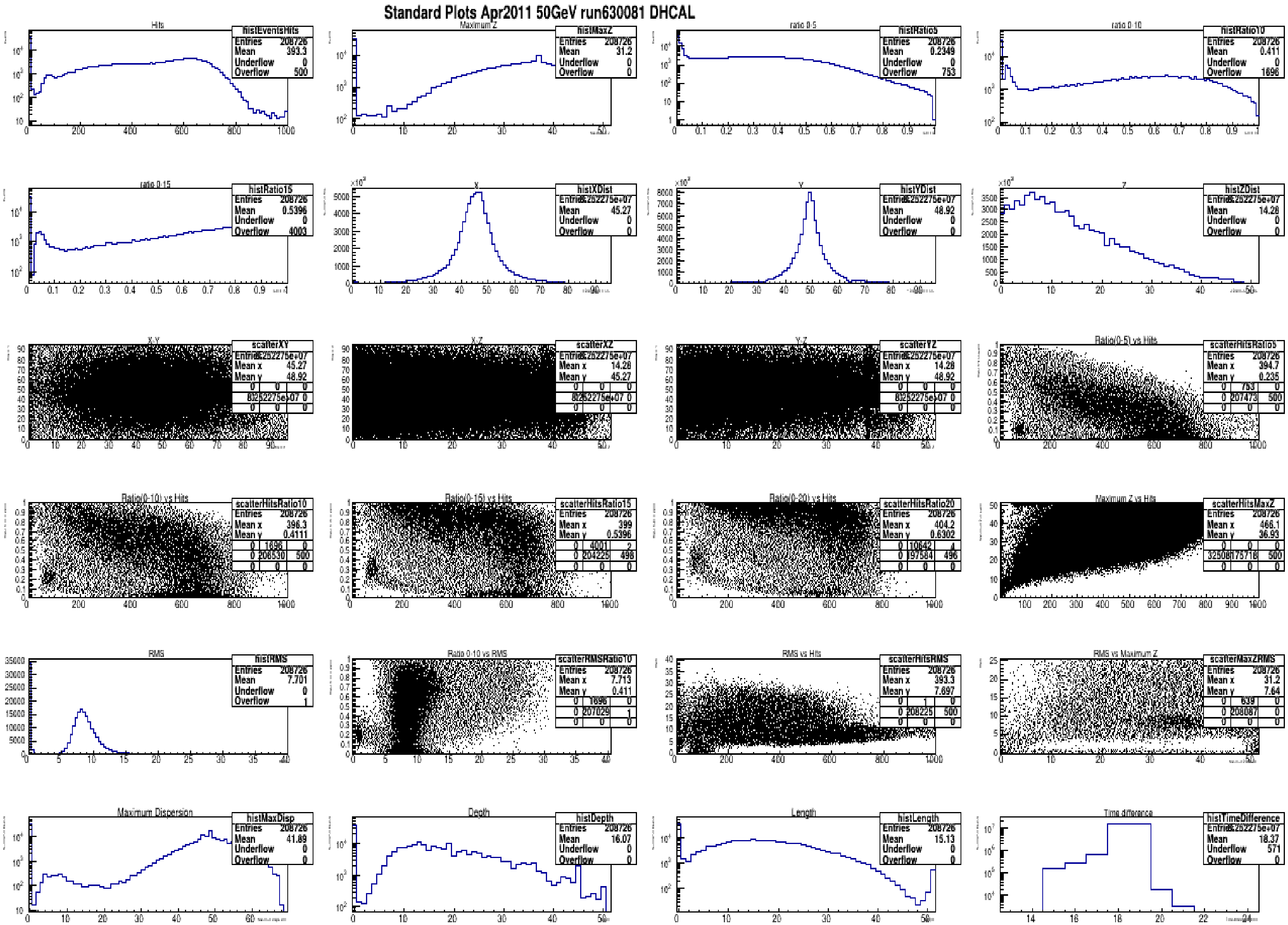

Figure 6.2: Example of the Standard Plots for DHCAL for a test run at 50 GeV in the April 2011 testing period.

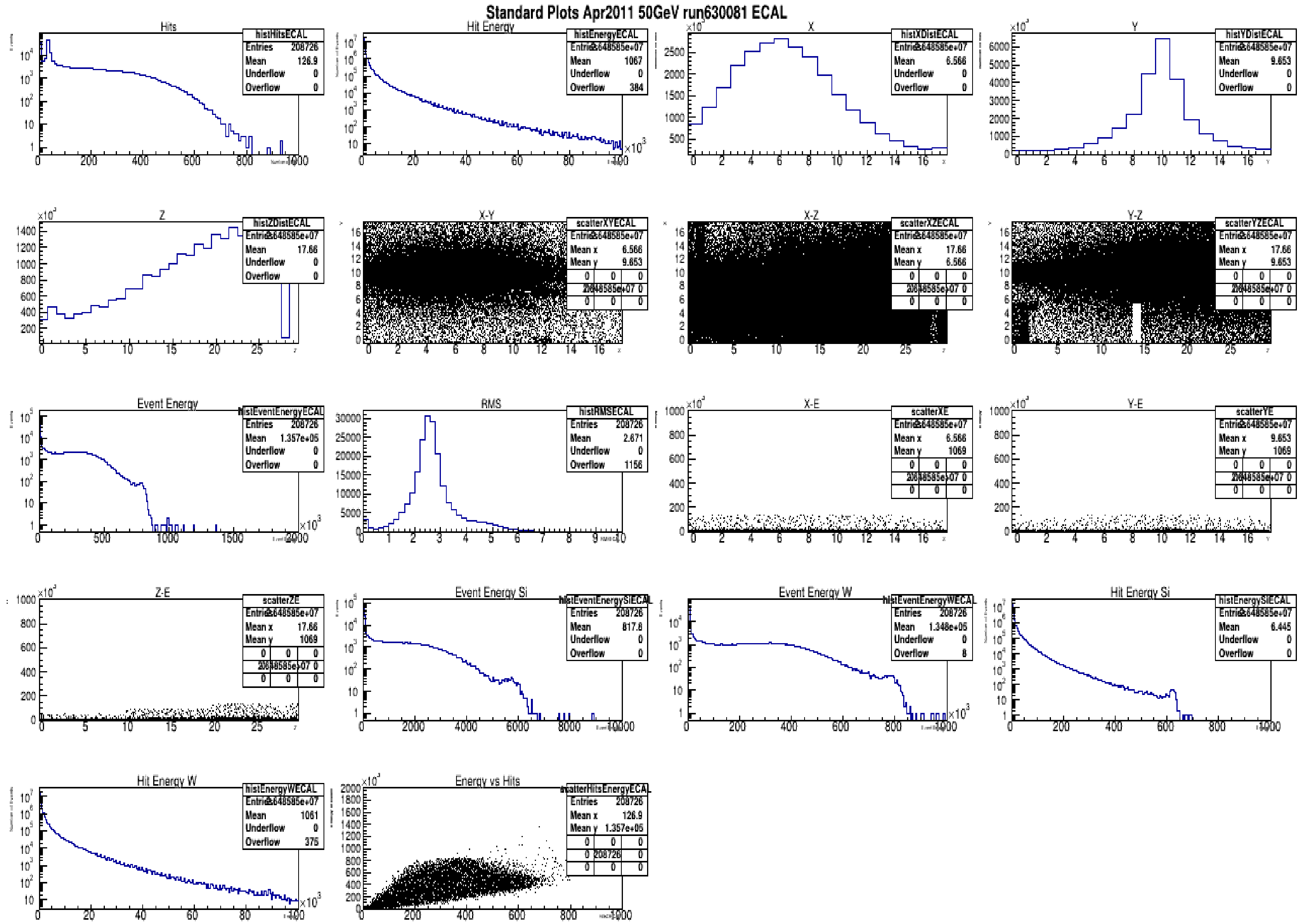

Figure 6.3: Example of the Standard Plots for ECAL for a test run at 50 GeV in the April 2011 testing period.

6.1.1 Run parameters for DHCAL

Number of hits The total number of hits recorded in DHCAL cells for an event. This parameter is one of the main components to perform particle identification. Using this parameter the muons can be easily separated from the rest of the particles.

Maximum Z Maximum layer reached by the event particles (shower or single particle). The expected characteristics of the muons and the two types of showers can be corroborated with this parameter after performing the particle identification.

Ratio 0-5 Ratio of hits recorded in the first 5 layers with respect to the total number of hits in the event. The ratios are used as the main tool to separate electromagnetic and hadronic showers.

Ratio 0-10 Ratio of hits recorded in the first 10 layers with respect to the total number of hits in the event. This is used in particle identification in the same way as Ratio 0-5 but for higher beam energies.

Ratio 0-15 Ratio of hits recorded in the first 15 layers with respect to the total number of hits in the event. This is used for separation of hadronic and electromagnetic showers at the highest beam energies.

RMS RMS value of the event distribution in the XY plane of the detector. This parameter helps visualize the lateral dispersion of the hits in one event.

Maximum Dispersion Maximum value of lateral dispersion (XY plane) reached by the particle shower. It is useful to separate muons and showers.

Depth Last layer reached by a particle coming from the test beam before showering. It can be implemented in particle identification between positron and pion showers using the ratio between radiation length and nuclear interaction length of the absorber material.

Length Total length in layers of the particle shower. It gives a measurement of the longitudinal development of a shower.

Time Difference Number of time bin in which the cell hit was recorded. The parameter is useful to separate hits from an actual particle from hits due to noise. The noise hits from remnants of past events are outside of the main distribution of time bins.

6.1.2 Run parameters for Si-W ECAL

Number of hits The total number of hits recorded in Si-W ECAL cells for an event.

RMS RMS value of the event in the XY plane of the detector.

Hit Energy Si Energy measured by a cell's silicon pad. This parameter represents the direct measurement from the silicon in arbitrary units.

Hit energy Energy measured by a cell's silicon pad plus the calculated energy lost in the tungsten for that layer in arbitrary units. The calculation of this parameter from the Hit Energy Si is explained in Section 9.1.

Hit Energy W Energy deposited in a Tungsten layer for a hit in a cell in arbitrary units. It is calculated as a function of the Hit Energy Si parameter and the number of layer of the hit. The calculation is shown in Equation 9.2.

Event Energy Si Sum of all Hit Energies in Silicon pads for an event.

Event Energy W Sum of all Hit Energies in Tungsten layers for an event. calculated from the energy measured in the cell's silicon pad.

Event Energy Sum of all Hit energies for an event. The parameter could be implemented in the particle identification to separate muons from shower events.

6.1.3 Combined Run parameters for ECAL + DHCAL

Total hits The total number of hits recorded in ECAL and DHCAL for the same event. Since the segmentation is similar for the two detectors, the total number of hits shows the separation between noise, muons, and showers. The separations can be seen on the Total Hits histogram from Figure 6.4.

Ratio ECAL Number of hits recorded in ECAL divided by the Total Hits of the event. Gives a visualization of the shower distributions in the combined ECAL-DHCAL system. It is used in particle identification for the April 2011 testing period.

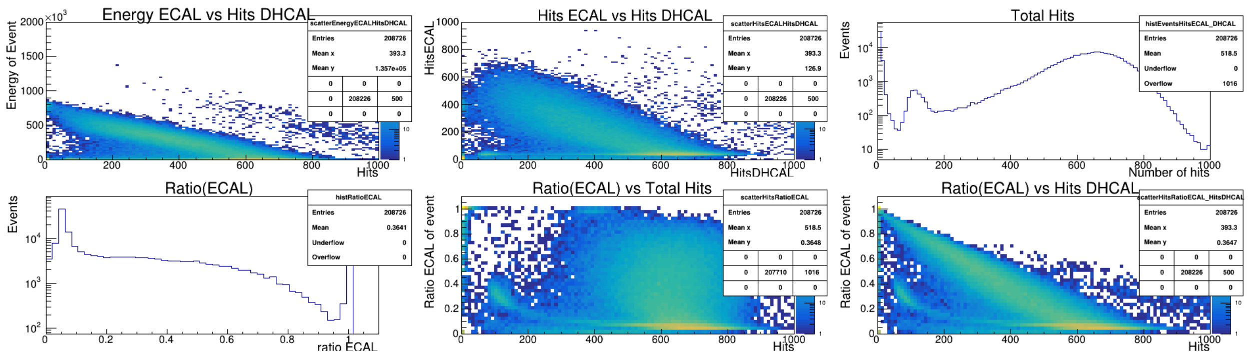

Figure 6.4: Example of the Standard Plots for a combination of ECAL and DHCAL parameters for a test run at 50 GeV in the April 2011 testing period. Top row: The plot on the left is a 2D histogram of Event Energy in ECAL (in arbitrary units) vs the number of hits in DHCAL, this shows how the energy of events is shared between the two detectors; the center plot shows the distribution of how the hits in a shower are shared between the two detectors; on the right the distribution of Total Hits is shown. Bottom row: Histogram of the Ratio ECAL parameter; the center plot is a 2D histogram of the Ratio ECAL vs Total Hits parameters, it shows clear separation between the three types of particles measured and it is the main plot used for the particle ID in the April 2011 period; the plot on the right shows a 2D histogram of the Ratio ECAL vs the number of hits in DHCAL.

6.2 Sets of cuts for particle identification

A Cherenkov counter was placed in front of the DHCAL during its testing at Fermilab to perform particle identification. Unfortunately, the Cherenkov counter was not working during the two periods used in this study. The alternative particle ID method is presented next.

The test beam at Fermilab is a combination of muons, pions and positrons. From the beam composing particles, the muons act as minimum ionizing particles (MIP) through both detectors leaving from zero to at most four hits per working layer of the detectors. An example of a typical muon event is shown in Figure 6.5. The pions and positrons will travel some distance into the detectors and start a shower. Examples of typical hadronic and electromagnetic showers are shown in Figures 6.6 and 6.7, respectively.

Hadronic and electromagnetic showers differentiate from each other by the average distance traveled by the initial particle before showering. Electromagnetic showers generally start earlier and are mostly contained within Si-W ECAL, which has a total depth of $24X_0$. On the other hand, pions can travel longer and can start their shower in the Si-W ECAL or DHCAL. The number of hits left by an electromagnetic or a hadronic shower is very similar, with no clear distinction in the Standard Plots.

The most useful way of combining the run parameters to proceed with particle identification was to make correlation plots of the parameters. For example, by plotting the different ratios against the number of hits one can observe three main accumulations of points: one at a low ratio and low hits, another one at a high ratio and higher hits than the first one, and the last at very low ratio and high number of hits. An example of these scatter plots is shown in Figure 6.8, the three mentioned accumulations of points are sectioned with different colored squares. In the case of a DHCAL-only test run, the first accumulation corresponds to the muons because these have a low ratio and low number of hits due to their MIP behavior. In the same plot, it can be seen that the muons leave a constant number of hits throughout the layers of DHCAL which makes the ratios low and leaves them at the same location for all energies. As mentioned before, the number of hits is very low since muons hit from zero to four cells at most in every layer.

The second accumulation corresponds to the positrons. Electromagnetic showers start earlier in the DHCAL, which means that most of their hits are on the first layers of the DHCAL. Therefore, the ratios for an electromagnetic shower are higher.

Hadronic showers have a similar number of hits to electromagnetic ones, but a much lower ratio since most of their hits are recorded later in the detector. Hadronic showers compose the third accumulation in the ratio vs hits Standard Plots.

In Figure 6.9 it can be observed that the positron and pion events form two distinguishable peaks in the Ratio plots. The two distributions cannot be completely disentangled

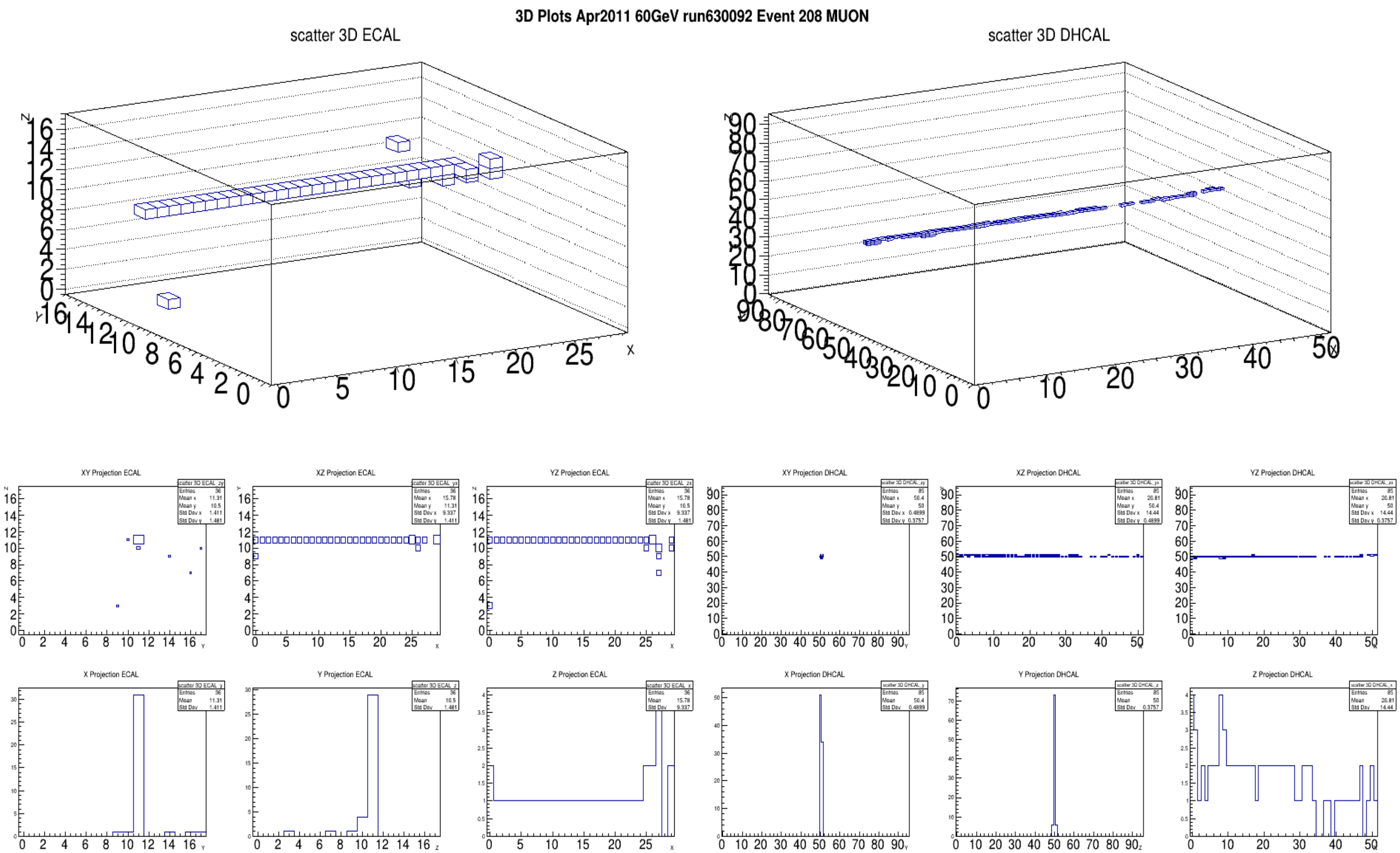

Figure 6.5: Example of a typical muon event for an April 2011 test run at 60 GeV. The top plots show the path of a muon starting on the left (first layer of Si-W ECAL and continuing all through the detector until reaching DHCAL (right plot) and again continuing its path until the last layer of DHCAL. The first three histograms on the second row show the XY, XZ, and YZ projections of ECAL respectively. The next three histograms of the second row show the XY, XZ, and YZ projections of DHCAL respectively. The bottom row shows 1D histograms of the X, Y, and Z distributions of hits in the event respectively. The first three histograms correspond to the ECAL 1D projections and the following three to DHCAL.

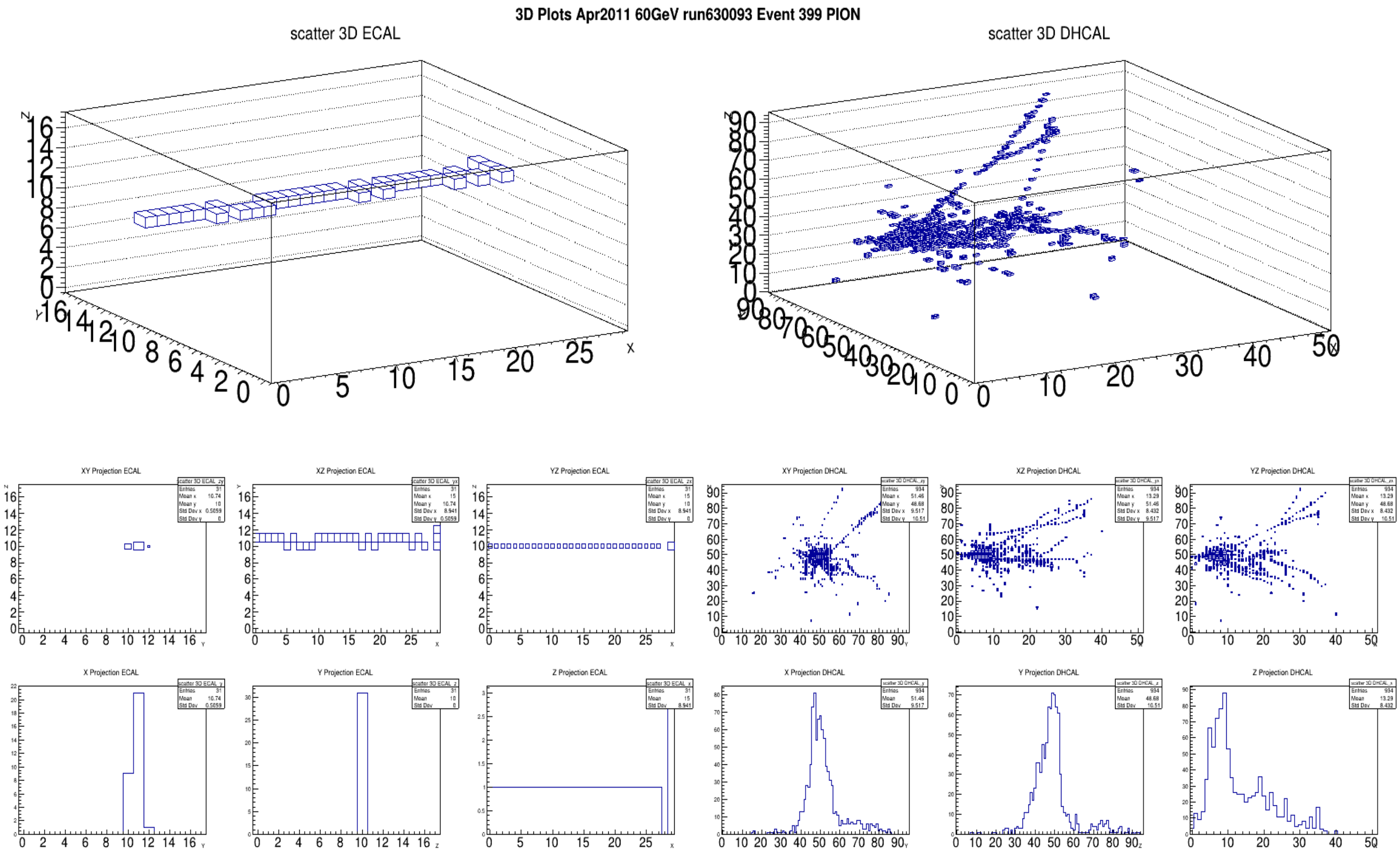

Figure 6.6: Example of a typical late showering pion event for an April 2011 test run at 60 GeV.The top plots show the path of the incoming pion starting on the left (first layer of Si-W ECAL and continuing all through the detector until reaching DHCAL (right plot) and again continuing its path until it starts a shower. The shower is fully contained in DHCAL. The first three histograms on the second row show the XY, XZ, and YZ projections of the hits in ECAL respectively. The next three histograms of the second row show the XY, XZ, and YZ projections of the hits in DHCAL respectively. The bottom row shows 1D histograms of the X, Y, and Z distributions of hits in the event respectively. The first three histograms correspond to the ECAL 1D projections and the following three to DHCAL.

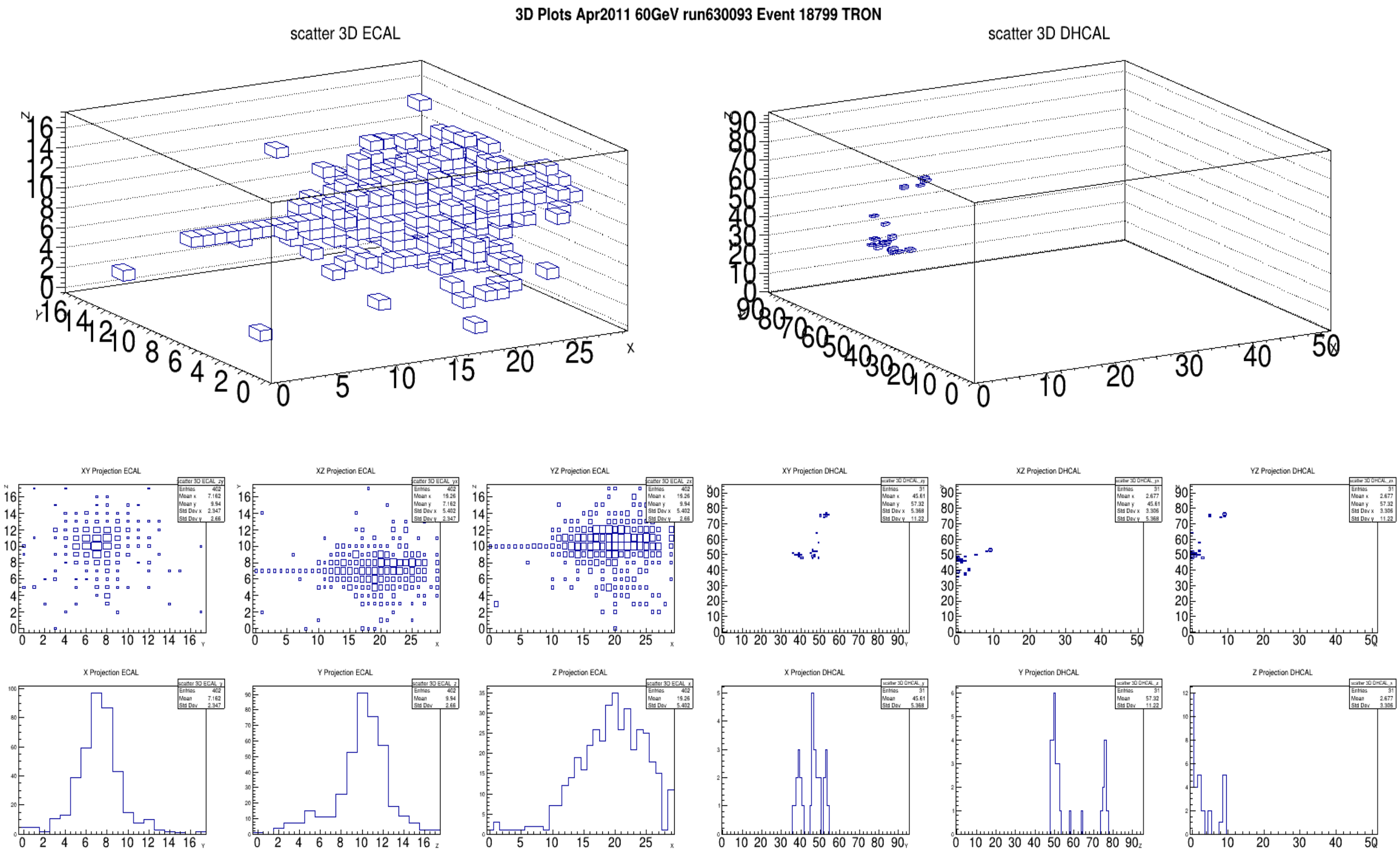

Figure 6.7: Example of a typical positron event for an April 2011 test run at 60 GeV. The top plots show the path of the incoming positron starting on the left (first layer of Si-W ECAL and continuing a straight trajectory until reaching starting a shower. The shower is mostly contained by ECAL and only a few particles deposit energy in the first layers of DHCAL, which is shown on the plot on the right. The first three histograms on the second row show the XY, XZ, and YZ projections of the hits in ECAL respectively. The next three histograms of the second row show the XY, XZ, and YZ projections of the hits in DHCAL respectively. The bottom row shows 1D histograms of the X, Y, and Z distributions of hits in the event respectively. The first three histograms correspond to the ECAL 1D projections and the following three to DHCAL.

in the region between them (between the red lines in Figure 6.9), this region represents a mixture between hadronic and electromagnetic events. The events in this region were therefore rejected from the analysis to reduce contamination in the samples.

Given the characteristics of the tracks and showers of each particle, it was possible to find cuts in the run parameters to perform particle identification while keeping the contamination from the other types of particles low. The cuts for particle identification made for the June 2011 period can be found in Table 6.4, which was made using the information from all sets of Standard Plots available for each energy.

Up to this point, only the data from DHCAL was used to separate the three types of particles, which is only useful for testing periods with DHCAL alone. After analyzing the Standard Plots with Si-W ECAL data (Figure 6.3 and Figure 6.4), the characteristics of showers and the properties of each detector were used to determine a new set of cuts combining Si-W ECAL and DHCAL data.

From the April 2011 test runs, only the runs for 50, 60 and 120 GeV contained both ECAL and DHCAL data. Therefore, the particle ID for all three particles was performed only to the available complete data sets. For energies below 50 GeV, the ECAL is ex-

June 2011 Particle ID Cuts							
e^+	8 GeV	16 GeV	32 GeV	40 GeV	50 GeV	60 GeV	120 GeV
Number of hits	>50	>150	>200	>200	>250	>300	>500
Ratio(0-10)	>0.5	>0.5					
Ratio(0-15)			>0.5	>0.5	>0.5	>0.5	>0.5
π^+	8 GeV	16 GeV	32 GeV	40 GeV	50 GeV	60 GeV	120 GeV
Number of hits	>200	>200	>200	>200	>250	>300	>500
Ratio(0-10)	<0.3	<0.3					
Ratio(0-15)			<0.2	<0.2	<0.2	<0.2	<0.2
μ^+	8 GeV	16 GeV	32 GeV	40 GeV	50 GeV	60 GeV	120 GeV
Number of hits	60<hits<120		60<hits<130				
Ratio(0-10)	0.1<ratio10<0.4						
Ratio(0-15)			0.2<ratio15<0.5				

Table 6.4: Set of particle ID cuts for the June 2011 testing period.

pected to contain all electromagnetic showers, this was used to separate the positrons from muons and pions.

For the April 2011 testing period, a part of the shower will be measured by the electromagnetic calorimeter, which affects mainly the distribution of number of hits and the different ratios in the DHCAL Standard Plots. In electromagnetic events, the number of hits in ECAL has to be higher than the hits left by a minimum ionizing particle to ensure the presence of a shower. According to the structure of ECAL, a MIP event will have at most 120 hits in ECAL, 4 for each one of the 30 layers in the detector.

Another condition set on the positrons is the containment in ECAL, which is measured by the parameters Ratio ECAL and number of hits in DHCAL. In the plot Ratio ECAL vs Total Hits from Figure 6.4, the positrons are localized as the accumulation at Ratio ECAL closer to 1 and Total hits between 300 and 500.

In the case of the pions, these are not expected to be fully contained by the ECAL, therefore, the Ratio ECAL is lower than for positrons. For this analysis, the hadronic showers were selected as any event with a high number of hits in DHCAL and less containment of the shower in ECAL in comparison to positrons of the same energy.

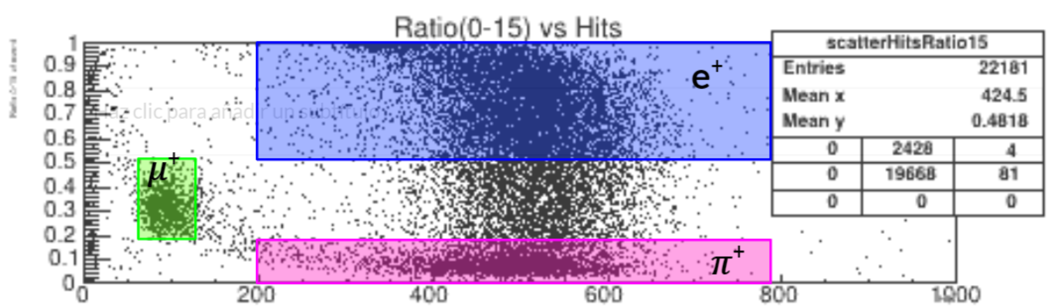

Figure 6.8: Example of the Ratio(0-15) vs Hits plot for a June 2011 test run at 32 GeV. The color squares represent the cuts for particle ID from Table 6.4. The color blue section corresponds to the positrons, the magenta section to the pions, and the green section to the muons. The gap between the pion and positron cuts in the vertical direction represents a mixture of hadronic and electromagnetic events. These events were discarded to reduce pion contamination in the positron sample and vice versa.

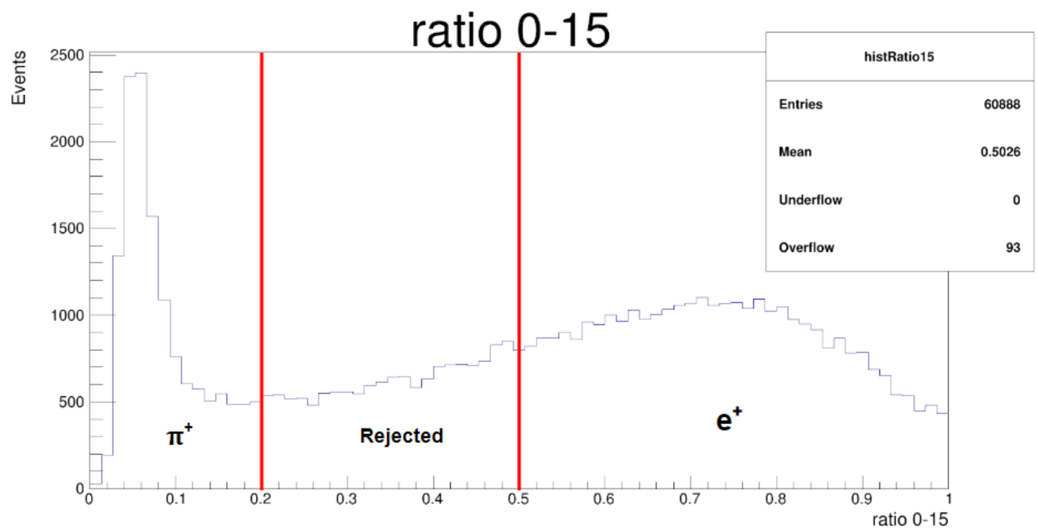

Figure 6.9: Example of the Ratio(0-15) plot after removing the muon events for a test run at 40 GeV from the June 2011 period. The first peak represents the pions, which start the shower later in the detector. The wider peak to the left corresponds to the positrons. The red lines represent the cuts for particle identification. The events between the red lines are discarded to minimize pion contamination in the positron sample and vice versa.

In the same way as for the DHCAL-only cuts, the muons can be found always in the same range of Ratio ECAL and number of hits for all energies.

All the particle identification cuts for the April 2011 testing period are shown in Table 6.5. The particle identification allowed the performance of individual analyses of the detector setup using each type of particle, which will be discussed in the following three chapters.

The late showering pions are the only type of shower that can be identified using only DHCAL data. Particle ID to find the late showering pions in the remaining data sets for April 2011 which did not include ECAL data was performed using the cuts listed in Table 6.6.

April 2011 Particle ID Cuts			
e^+	50 GeV	60 GeV	120 GeV
Number of hits DHCAL	<25	<75	<150
Number of hits ECAL	>120	>120	>120
Ratio ECAL	>0.95	>0.85	>0.8
π^+	50 GeV	60 GeV	120 GeV
Number of hits DHCAL	>50	>110	>200
Number of hits ECAL			
Ratio ECAL	<0.9	<0.75	<0.7
μ^+	50 GeV	60 GeV	120 GeV
Number of hits DHCAL	60<hits<100		
Number of hits ECAL	<120		
Ratio ECAL	0.2<ratioECAL<0.5		

Table 6.5: Set of particle ID cuts for the April 2011 testing period.

April 2011 Particle ID Cuts for Late showering pions					
π^+	12 GeV	16 GeV	25 GeV	32 GeV	40 GeV
Number of hits DHCAL	>120	>120	>120	>120	>150
Ratio(0-15)	<0.15	<0.2	<0.2	<0.2	<0.2

Table 6.6: Set of particle ID cuts for late showering pions in energies of 40 GeV and below in the April 2011 testing period.

Chapter 7

Alignment

With the particle identification done, each different type of particle was used for separate parts of the analysis. This section explains the procedure used to perform an analysis on the alignment of the Si-W ECAL and DHCAL with respect to each other. In this project, the alignment was measured using the tracks of muons coming from the secondary beam in the April 2011 testing period. In Table 6.1, it is stated that a total of 2.5M muon events were recorded from dedicated muon test runs. Unfortunately, the data sets from these runs were missing the Si-W ECAL part of the hits. The track analysis was therefore performed using the muon events from the test runs in which the secondary beam was used.

In the secondary beam at the Fermilab Test Beam facilities, the relative number of muons decreases as a function of the energy of the beam, while the number of pions increases. This means that for the available energies of 50 GeV, 60 GeV, and 120 GeV only a total of 945 muons were used to test the alignment, with 50 GeV having the highest number of muons events. A total of 792 events after cuts for the single 50 GeV test run. The number of muon tracks available for the two 120 GeV test runs was too small, therefore, these were discarded and the analysis was only done to the 50 GeV and 60 GeV muon tracks. The distribution of the number of muon events between the used test runs can be seen in Table 7.1.

The alignment of each individual detector (alignment between layers of the same detectors) as well as the alignment between the two detectors is not measured by any physical mechanism within the design. The initial alignment was performed manually using

Beam energy	Run	Number of muon events
50 GeV	630081	792
60 GeV	630090	47
	630091	13
	630092	21
	630093	53
	630094	19
120 GeV	630095	3
	630097	3

Table 7.1: Distribution of number of muon events for the April 2011 test runs.

rulers. Alignment studies between the Front-End Boards (FEBs) of each layer have been performed using the muon test beam at Fermilab. The analysis was done for the DHCAL Main Stack right after construction in October 2010. The average relative misalignment between the FEBs was found to be $0.0003 \pm 0.22\ cm$ in X and $-0.0001 \pm 0.12\ cm$ in Y [1] for the testing period. Results on the alignment of FEBs can only be used within a same testing period of the DHCAL to ensure that there was no replacement of layers or physical movement of the detector. Therefore, the results from the October 2010 commissioning were not included in this project's analysis.

When muons pass through the material of the detectors they act as minimum ionizing particles. This makes them be able to travel straight through both detectors without showering and leaving only the minimum ionizing energy in the material. An example of a straight track left by a muon can be seen in Figure 7.1.

7.1 Cuts for noise and track quality

In Figure 7.1 it can be observed that for the Si-W ECAL there can be random cells with hits outside of the muon track. These hits are a type of noise for this detector which is observed in all types of events, including empty events. The noise was later eliminated by applying a set of conditions to ensure clear muon tracks in the two detectors.

All the muon events extracted from the particle identification were then filtered to find clean straight tracks. The first condition was to discard any layer with more than four hits from the analysis. These were observed to be faulty layers in the detectors as a muon can

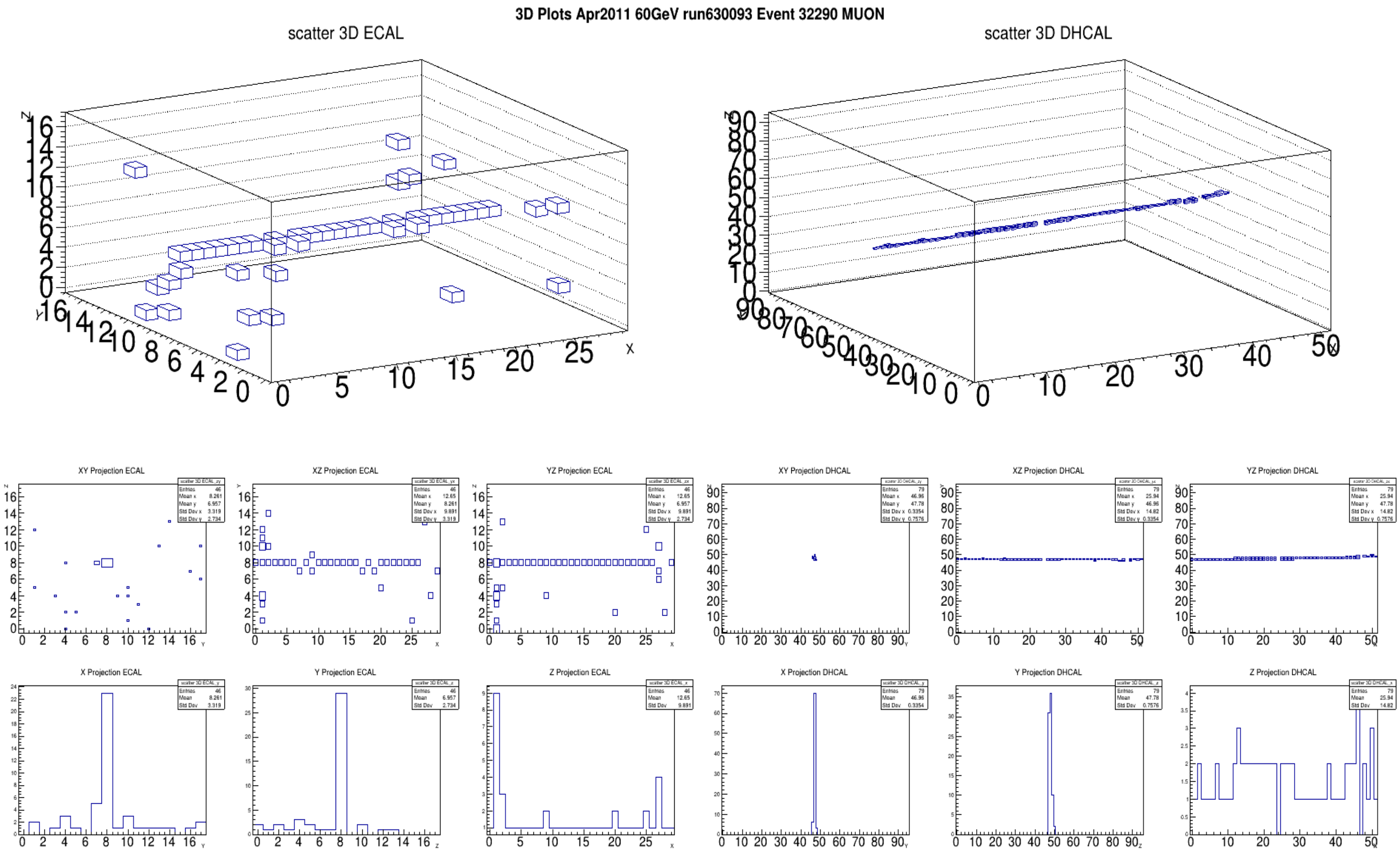

Figure 7.1: Example of a muon event with a considerable amount of noise in ECAL hits for an April 2011 test run at 60 GeV before clearing for noise. The top plots show the path of a muon starting on the left (first layer of Si-W ECAL and continuing all through the detector until reaching DHCAL (right plot) and again continuing its path until the last layer of DHCAL. The first three histograms on the second row show the XY, XZ and YZ projections of ECAL respectively. The next three histograms of the second row show the XY, XZ and YZ projections of DHCAL respectively. The bottom row shows 1D histograms of the X, Y and Z distributions of hits in the event respectively. The first three histograms correspond to the ECAL 1D projections and the following three to DHCAL.

only interact with at most four neighbouring cells since the cross talk between cells is low. The mentioned condition also helps to discard layers with more than one muon recorded in the same event. The condition was applied to both detectors.

After cutting out faulty layers, it was necessary to ensure a straight track and clear noise. The second cut filters out hits outside of the cells directly neighboring the main track. This was done for both detectors using the same 1 cell radius since both detectors have the same cell size. A third and last loose condition was implemented to completely discard events with less than 10 layers with hits in one of the calorimeters.

7.2 Measurement of misalignment procedure

After the cuts and discarding of layers and hits, the remaining muon tracks were fitted a linear function in the XZ and XY profiles separately. An example of a clean track with fits is shown in Figure 7.2. Unlike Figure 7.1 where the Z coordinate shows the number of layer, the Z axis of Figure 7.2 is in units of centimeters to show the actual physical spacing between the active layers of the detectors. The fits for DHCAL exclude the last 14 layers of the DHCAL structure which correspond to the TCMT. Therefore the alignment was analyzed only between the Si-W ECAL and the Main Stack of DHCAL. The linear fits were applied individually to each track in the same test run.

The linear fits gave initial measurements of the misalignment between the detectors. The following parameters were calculated individually for each track to measure the misalignment between the two detectors:

X Distance Obtained from subtracting the X coordinates of the linear functions from the fits to the Si-W ECAL and DHCAL track points at Z equal to the equidistant point between the detectors.

Y Distance The same procedure from the X Distance was performed to obtain the Y Distance measurements, using the YZ Profile fits.

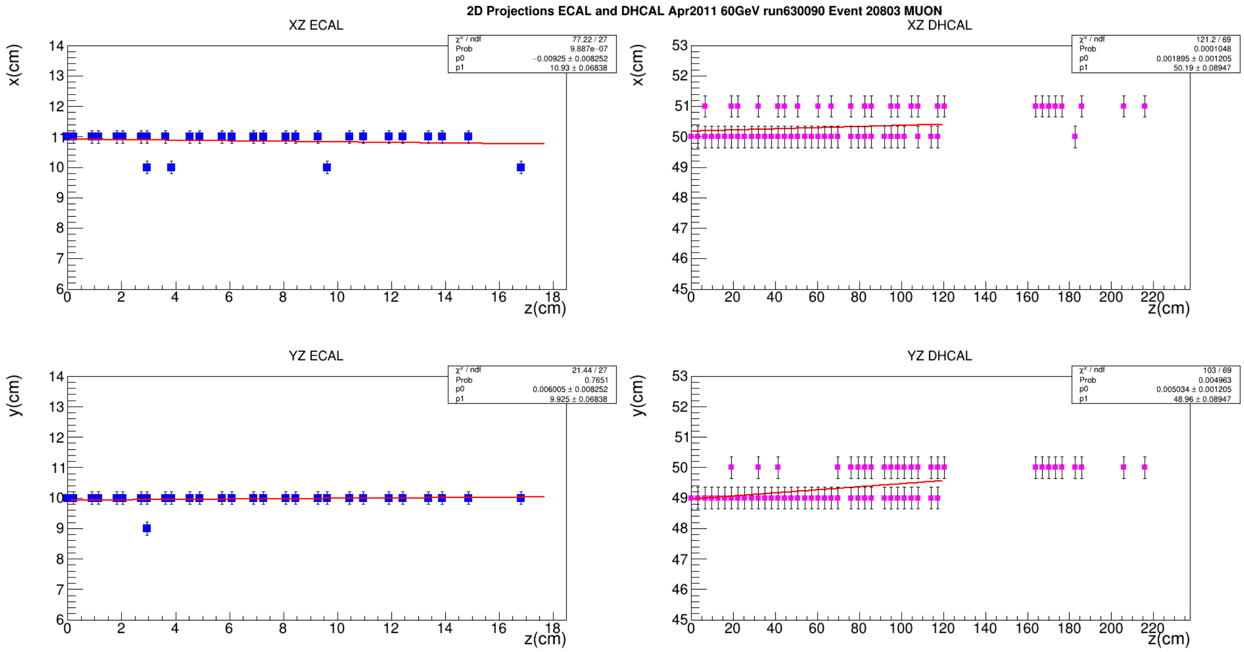

Figure 7.2: 2D Representation of a muon event with linear fits on XZ and YZ profiles of the detector Si-W ECAL+DHCAL system for a 60 GeV test run. The top left plot shows XZ projection of the muon's trajectory through Si-W ECAL until reaching its last layer and continuing on the DHCAL which is shown in the plot to the top right. The bottom left and bottom right plots show the same sequence but for the YZ projections. All fits are linear fits with p0 as the slope and p1 as the intercept to the vertical axis.

XZ and YZ Angle The measurements correspond to subtracting the slope of the DHCAL track from the slope of the Si-W ECAL track. Two angles were calculated, one for each side profile of the detectors setup.

An example of the X Distance distribution for all the good muon tracks in the 50 GeV test run can be observed in Figure 7.3.

A weighted average of each one of the aforementioned parameters was calculated for each test run. The results on the average alignment parameters for the studied test runs can be seen in Table 7.2. It is observed that the DHCAL is slightly shifted horizontally (in X) to the right with respect to the Si-W ECAL. This is found for all runs of the two studied energies. In the Y direction (vertical) the detectors are better aligned. The first five runs the DHCAL can be observed as being set lower than the ECAL. The opposite is observed

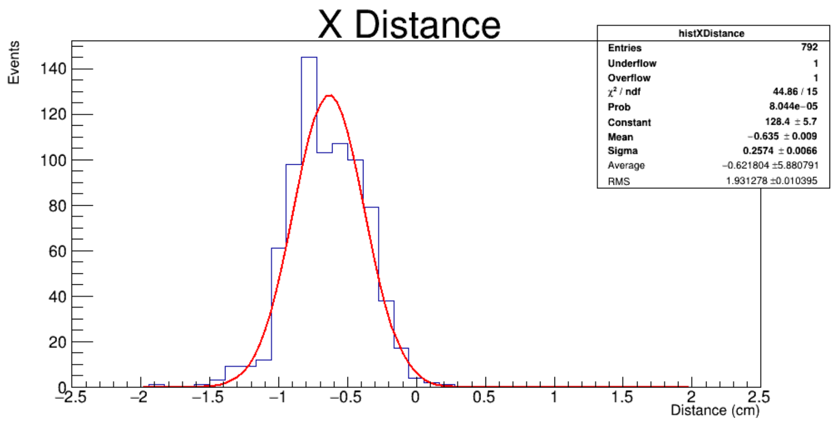

Figure 7.3: X Distance distribution for the 50 GeV test run muon tracks before moving DHCAL.

Energy	**Run**	**X Distance (cm)**	**Y Distance (cm)**	**XZ Angle (degrees)**	**YZ Angle (degrees)**
50 GeV	630081	-0.618 ± 0.007	0.107 ± 0.007	-0.644 ± 0.018	0.124 ± 0.018
60 GeV	630090	-0.695 ± 0.030	0.131 ± 0.030	-0.595 ± 0.075	0.082 ± 0.075
	630091	-0.764 ± 0.059	0.019 ± 0.059	-0.747 ± 0.145	0.247 ± 0.145
	630092	-0.687 ± 0.045	0.068 ± 0.045	-0.603 ± 0.111	0.281 ± 0.111
	630093	-0.687 ± 0.029	0.126 ± 0.029	-0.765 ± 0.071	0.091 ± 0.071
	630094	-0.677 ± 0.049	-0.014 ± 0.049	-0.696 ± 0.121	-0.040 ± 0.121
	Average 60 GeV	-0.695 ± 0.017	0.093 ± 0.017	-0.680 ± 0.042	0.111 ± 0.042

Table 7.2: Results for the misalignment parameters of the original muon tracks. The data points represent the averages of the alignment parameters from all tracks in the same test run. All runs belong to the April 2011 testing period. All errors are purely statistical. The average for the 60 GeV runs was weighted by their number of events to properly compare to the 50 GeV results.

for run 630094. The angle measurements corroborate the direction of the misalignment found in the X and Y distances. In general for all the runs, the detectors have less than 1° difference in slope and are all roughly consistent with each other. The sum average of the misalignment parameters was also calculated to get an estimate of the systematic uncertainties, these estimated are shown in Table 7.3. The results of each test run from Table 7.2 were plotted together in Figure 7.4.

Before moving DHCAL Systematic Uncertainties					
Energy	**Run**	$\delta_{XDistance}$ **(cm)**	$\delta_{YDistance}$ **(cm)**	$\delta_{XZAngle}$ **(degrees)**	$\delta_{YZAngle}$ **(degrees)**
50 GeV	630081	0.002	0.024	0.019	0.020
60 GeV	630090	0.010	0.001	0.007	0.014
	630091	0.003	0.040	0.006	0.033
	630092	0.008	0.014	0.018	0.025
	630093	0.000	0.004	0.007	0.014
	630094	0.001	0.009	0.008	0.001
Average 60 GeV		0.005	0.008	0.009	0.015

Table 7.3: Systematic errors from the misalignment parameters before moving DHCAL for each analyzed run. The average for the 60 GeV runs' systematic errors was weighted by their number of events.

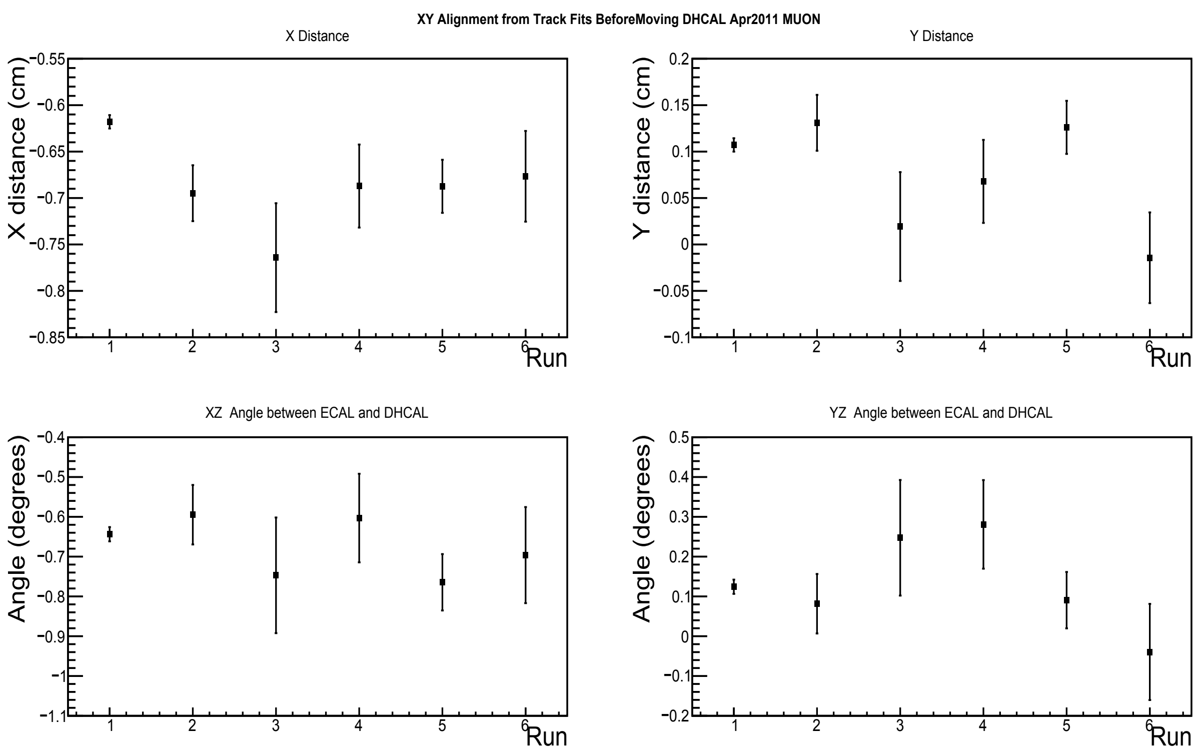

Figure 7.4: Results for the average alignment parameters before moving the DHCAL. For all plots, the runs are in the following order: 1=630081, 2=630090, 3=630091, 4=630092, 5=630093, and 6=630094. The data points are listed in Table 7.2.

The errors showed in the Table 7.2 are calculated from the average to the alignment parameters. The sizes of the errors for the data points of each parameter are associated to the number of tracks used in the analysis of the test run. The 50 GeV run has the smallest uncertainty in all the alignment results due to the large number of events in comparison to the 60 GeV test runs. However, the results show a good agreement between the two energies. The misalignment of the last 60 GeV test run (last row of Table 7.2) has the opposite direction as the rest of the runs for the Y Distance and YZ Angle, this can be the result of a small movement of the detectors between test runs. Unfortunately, there is no available information about any modification in the experimental setup. In any case, the deviation of one run from the rest of the is not very significant given the size of the uncertainties.

7.3 Correction of misalignment

Using the initial alignment measurements for all the runs with Si-W ECAL and DHCAL data, the tracks in DHCAL were "moved" to account for the average offset and angle difference in both profiles of the experimental setup.

If the misalignment between the detectors happens to be large enough, the detectors can be physically moved to correct using the tracks from the muon runs taken usually at the beginning of the testing periods. In a case where the detectors cannot be moved, the correction can be performed using a software which moves the coordinates of all the DHCAL hits in a data set.

In this project a program was created to move the coordinates of the DHCAL hits using the averages from Table 7.2. It can be observed in Figure 7.4 that the average misalignment of the detectors is not perfectly compatible between different beam energies or between all test runs of the same beam energy. These results can be related to the time between the data taking for each test run. The 60 GeV test runs were taken three to six days after the analyzed 50 GeV run. An adjustment of the detectors might have been done in the time between test runs of different beam energy. This information is not available. Therefore, it was decided that the best approach in this analysis was to study each test

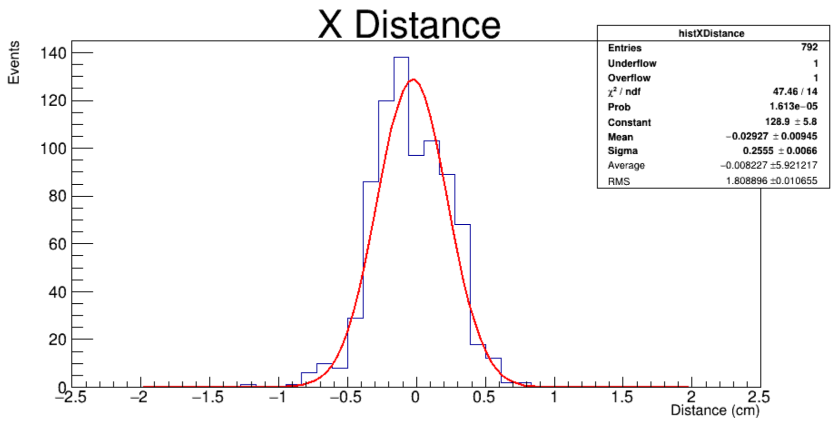

Figure 7.5: X Distance distribution for the 50 GeV test run muon tracks after moving DHCAL.

run individually. The procedure used by the alignment correction software is explained next.

First, every point in the DHCAL track was rotated by the average XZ and YZ Angle. The physical center of the first layer of DHCAL was taken as the pivot point for the rotation of both angles. This pivot of the rotation was chosen because it is a point from which the detector can be manually moved in a lab setting to correct for the misalignment. Given the chosen pivot point, the average X and Y offsets between the detectors change after the rotation. To fix this, the X and Y Distances from Table 7.2 were corrected by a factor of the sine of the average rotation angle at the equidistant point between ECAL and HCAL.

Lastly, the points were translated by adding the corrected X and Y Distances respectively for each profile of the experimental setup. A linear function was fitted to the moved tracks in the same way as the original tracks in the past section. An example of the X Distance distribution for corrected tracks in the 50 GeV run can be observed in Figure 7.5.

The alignment parameters found from the linear fits to the moved tracks were then averaged for each individual test run. The results on the average alignment parameters after moving DHCAL can be found in Table 7.4. The systematic uncertainties were calculated in the same way mentioned in the past section, the results can be seen in Table 7.5. The data points from Table 7.4 are also plotted on Figure 7.6 to better compare each test run. The correction procedure was performed individually to each muon track using the average distances and angles obtained for the test run of the track. For this reason,

Energy	Run	X Distance (cm)	Y Distance (cm)	XZ Angle (degrees)	YZ Angle (degrees)
50 GeV	630081	-0.005 ± 0.007	-0.004 ± 0.007	0.003 ± 0.018	0.003 ± 0.018
60 GeV	630090	-0.004 ± 0.030	-0.005 ± 0.030	0.002 ± 0.075	0.004 ± 0.075
	630091	-0.005 ± 0.059	-0.005 ± 0.059	0.002 ± 0.145	0.004 ± 0.145
	630092	-0.004 ± 0.041	-0.007 ± 0.045	0.002 ± 0.111	0.005 ± 0.111
	630093	-0.006 ± 0.029	-0.003 ± 0.029	0.004 ± 0.071	0.002 ± 0.079
	630094	-0.007 ± 0.049	0.006 ± 0.049	0.005 ± 0.121	-0.005 ± 0.121
	Average 60 GeV	-0.005 ± 0.017	-0.003 ± 0.017	0.003 ± 0.042	0.002 ± 0.043

Table 7.4: Results for the alignment parameters of the muon tracks after moving the DHCAL with respect to the Si-W ECAL using the results from Table 7.2. All runs belong to the April 2011 testing period and correspond to the same events used for Table 7.2. The average over the 60 GeV runs was weighted by their number of events.

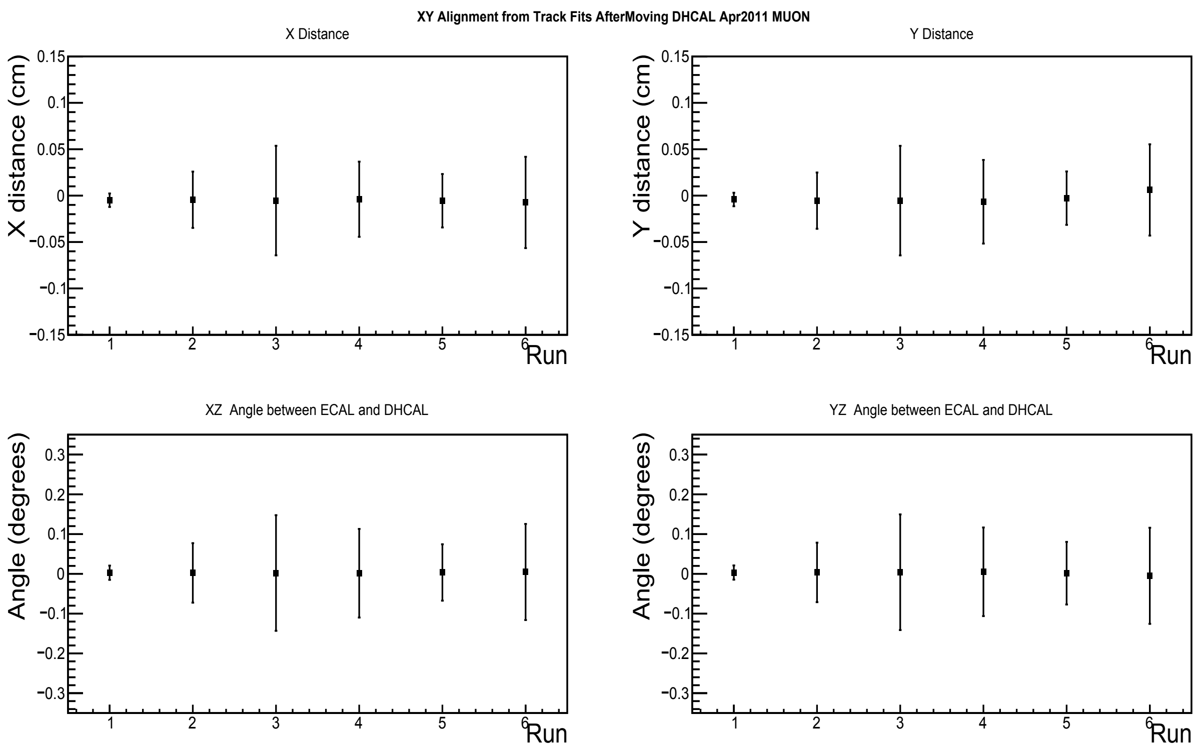

Figure 7.6: Results for the average alignment parameters after moving the DHCAL with respect to the Si-W ECAL. For all plots, the runs are in the following order: 1=630081, 2=630090, 3=630091, 4=630092, 5=630093, and 6=630094. The information of the data points is listed in Table 7.4.

After moving DHCAL Systematic Uncertainties					
Energy	**Run**	$\delta_{XDistance}$ **(cm)**	$\delta_{YDistance}$ **(cm)**	$\delta_{XZAngle}$ **(degrees)**	$\delta_{YZAngle}$ **(degrees)**
50 GeV	630081	0.002	0.024	0.019	0.020
60 GeV	630090	0.010	0.001	0.007	0.014
	630091	0.009	0.001	0.007	0.014
	630092	0.008	0.015	0.018	0.025
	630093	0.000	0.004	0.007	0.013
	630094	0.001	0.009	0.008	0.001
Average 60 GeV		0.005	0.005	0.009	0.014

Table 7.5: Systematic errors from the alignment parameters after moving DHCAL for each analyzed run. The average over the 60 GeV runs was weighted by their number of events.

the alignment parameters from Table 7.4, are not exactly equal to zero after moving the DHCAL. Although, they are consistent with zero within uncertainties, therefore the correction of the alignment was correctly performed individually for the analyzed test runs. The systematic errors associated to particle identification cuts for the muons and track selection cuts were not calculated as that part of the statistical analysis was out of the scope of the project.

7.4 Global Fit

Another step of the analysis was performed next in which not only the tracks in the DHCAL were moved to be aligned to the Si-W ECAL tracks but both tracks were aligned to the center of the detectors. This procedure was done to measure the straightness of all the individual tracks in a test run after aligning the detectors. The procedure for the movement of the tracks is explained next.

First, the DHCAL tracks were moved in the same way as it was explained in section 7.3. This procedure aligns the DHCAL to the Si-W ECAL. Having the detectors aligned, Si-W ECAL hit coordinates were fitted to a linear function to find the offset of the start of the track with respect to the center of the first layer of the detector. This measurement was calculated for X and Y directions. The slope of the Si-W ECAL track was also cal-

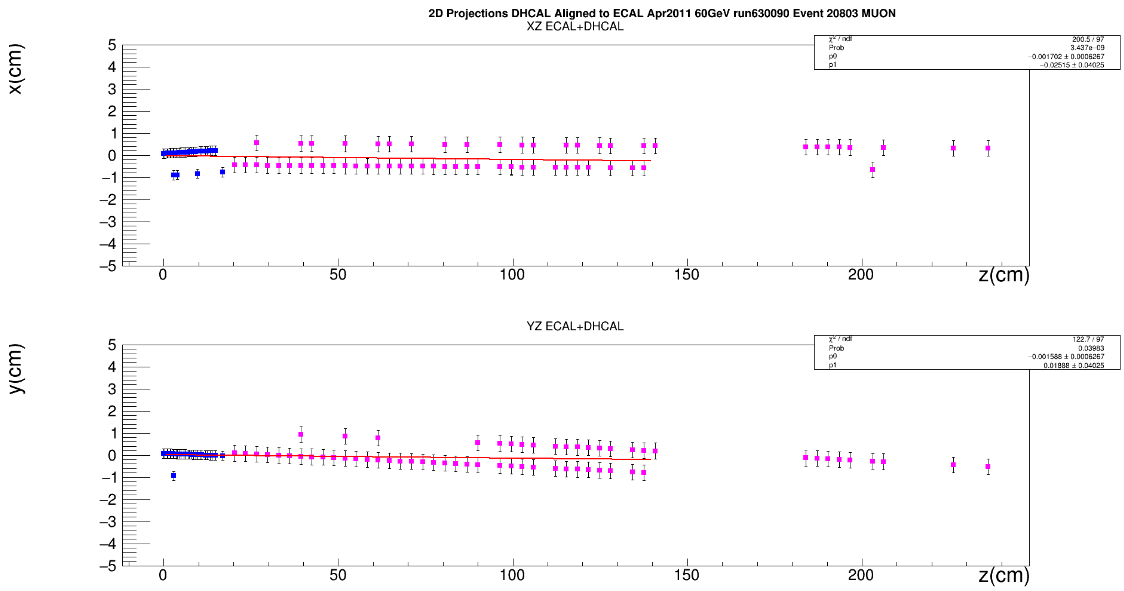

Figure 7.7: Profile hit representations of a muon event with Global Fit for a 60 GeV test run track after moving the track points of DHCAL (in magenta) with respect to the Si-W ECAL (in blue) and translating the full track to the horizontal axis. The first layer of the Si-W ECAL is placed at $z = 0$ and the first layer of DHCAL at $z = 20.225$ equivalent to the depth of ECAL plus $2\ cm$ of space between the two detectors. The top plot shows the XZ profile of the detector setup. The bottom plot shows the YZ profile. The error bars assigned to the hits are arbitrary, but they are the same for every hit of the same track.

culated for both side profiles. Each individual Si-W ECAL+DHCAL track was moved according to this offset and angle to be aligned to the geometric center of the first layer of the Si-W ECAL. After moving both tracks a linear function was fitted to the full Si-W ECAL+DHCAL muon track, i.e. a fit from the first layer of ECAL to the last layer of the Main Stack of DHCAL. The name Global Fit was given to this fit. An example of the full muon track with the fit is shown in Figure 7.7. The track points were given the same weight per detector. This was to account for the difference in the number of layers between the two detectors. To achieve this, the errors for the track points of ECAL were multiplied by a factor of N_{ECAL}/N_{Total}, where N_{ECAL} is the number of track points from ECAL and N_{Total} are the total number of points in the track (ECAL+DHCAL points). The DHCAL track point errors were multiplied by the factor N_{DHCAL}/N_{Total}.

Energy	Run	X Distance (cm)	Y Distance (cm)	XZ Angle (degrees)	YZ Angle (degrees)
50 GeV	630081	-0.001 ± 0.002	0.006 ± 0.002	0.017 ± 0.001	0.000 ± 0.001
60 GeV	630090	-0.008 ± 0.006	0.004 ± 0.006	0.018 ± 0.006	-0.001 ± 0.006
	630091	-0.011 ± 0.013	0.004 ± 0.013	0.000 ± 0.013	-0.064 ± 0.013
	630092	-0.002 ± 0.009	0.006 ± 0.010	-0.037 ± 0.009	0.046 ± 0.009
	630093	-0.010 ± 0.006	0.002 ± 0.006	0.020 ± 0.006	0.021 ± 0.006
	630094	-0.016 ± 0.010	-0.005 ± 0.011	0.051 ± 0.010	0.043 ± 0.010
	Average 60 GeV	-0.009 ± 0.004	0.002 ± 0.004	0.014 ± 0.004	0.013 ± 0.004

Table 7.6: Results for the alignment parameters from the Global Fits to the moved Si-W ECAL+DHCAL muon tracks. All runs belong to the April 2011 testing period. The average over the 60 GeV runs was weighted by their number of events.

Global Fit Systematic Uncertainties					
Energy	**Run**	$\delta_{X Distance}$ **(cm)**	$\delta_{Y Distance}$ **(cm)**	$\delta_{XZ Angle}$ **(degrees)**	$\delta_{YZ Angle}$ **(degrees)**
50 GeV	630081	0.001	0.001	0.103	0.001
60 GeV	630090	0.000	0.000	0.004	0.010
	630091	0.001	0.001	0.003	0.002
	630092	0.005	0.003	0.042	0.005
	630093	0.001	0.002	0.012	0.004
	630094	0.001	0.002	0.014	0.017
Average 60 GeV		0.001	0.001	0.013	0.007

Table 7.7: Systematic errors from the alignment parameters of Global Fit for each analyzed run. The average over the 60 GeV runs was weighted by their number of events.

In the Global Fit analysis, the X and Y distances now represent the distance between the geometrical center of the Si-W ECAL and the track at the middle point between the two detectors ($z = 19.025$). The XZ and YZ angles were also redefined, so they now represent the slopes of the linear fits. An average of each alignment parameter was found for each test run.

The results for the averages values of the alignment parameters from the Global Fits of all available runs are given in Table 7.6. The data is also plotted in Figure 7.8 for a visual representation. The systematic errors associated to the weighted average of each Global Fit parameter are shown on Table 7.7.

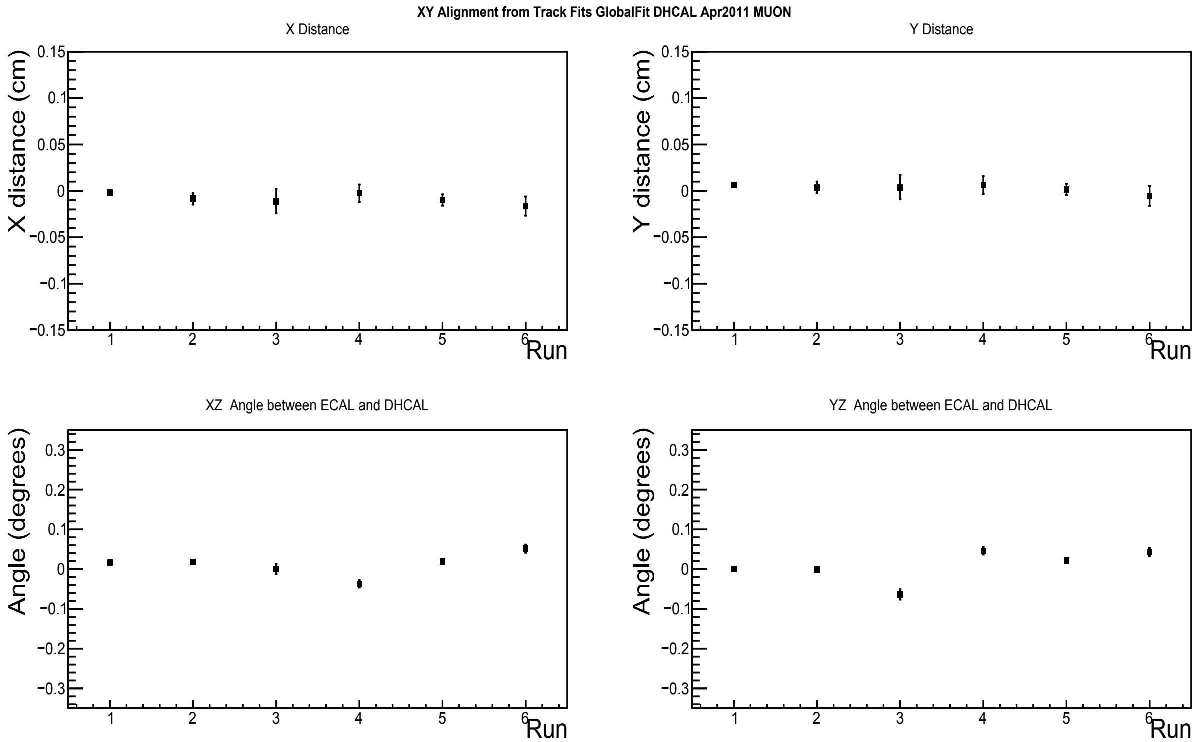

Figure 7.8: Results for the average alignment parameters from the Global Fit after moving the DHCAL and Si-W ECAL to align the track to the center of the detector system. For all plots, the runs are in the following order: 1=630081, 2=630090, 3=630091, 4=630092, 5=630093, and 6=630094. The information of data points are listed in Table 7.6.

From the X and Y distances' uncertainties in Table 7.6, it can be observed that the tracks can be resolved to distances better or equal to $0.013\ cm$ in X or Y, even when the cell size of the calorimeters is $1 \times 1\ cm^2$. These are statistical errors only. A general systematic error estimate for the method could be done with the $0.016\ cm$ as the maximum deviation observed in X, with $0.006\ cm$ in Y, with $0.037°$ in the XZ angle, or with $0.064°$ in the YZ angle.

Chapter 8

Linearity for DHCAL

For analog calorimeters, the dependence between the measured signals and the beam energy is mostly non-linear [9]. For all calorimeter technologies, the non-linearity comes from different factors corresponding to the technology itself.

The non-linearity observed in a digital calorimeter comes from two or more particles of one shower triggering the same cell at the same time. This phenomenon is called saturation, since the number of cells hit does not reflect the amount of energy deposited in the calorimeter. It is important to measure the linearity of detector systems to properly characterize the calorimeter's energy response.

The linearity of the DHCAL prototype was analyzed for two separate testing periods at Fermilab: April and June 2011. The beam energy range for both testing periods goes from 4 GeV to 120 GeV. The experimental set up for the testing period of June 2011 consisted on the DHCAL 38-layer Main Stack and the 14-layer TCMT, a total of 52 layers. The testing period of April 2011 had the same DHCAL configuration as June 2011, placed behind a 30-layer Si-W ECAL prototype. For June 2011, the linearity was analyzed for both hadronic and electromagnetic showers.

In the case of April 2011, the Si-W ECAL contains 95% of electromagnetic showers for beam energies below 50 GeV, as explained in section 5.2. Given this, the DHCAL data for this period on test runs below 50 GeV in beam energy has no hits from electromagnetic showers. Therefore, the linearity analysis was only performed for hadronic showers.

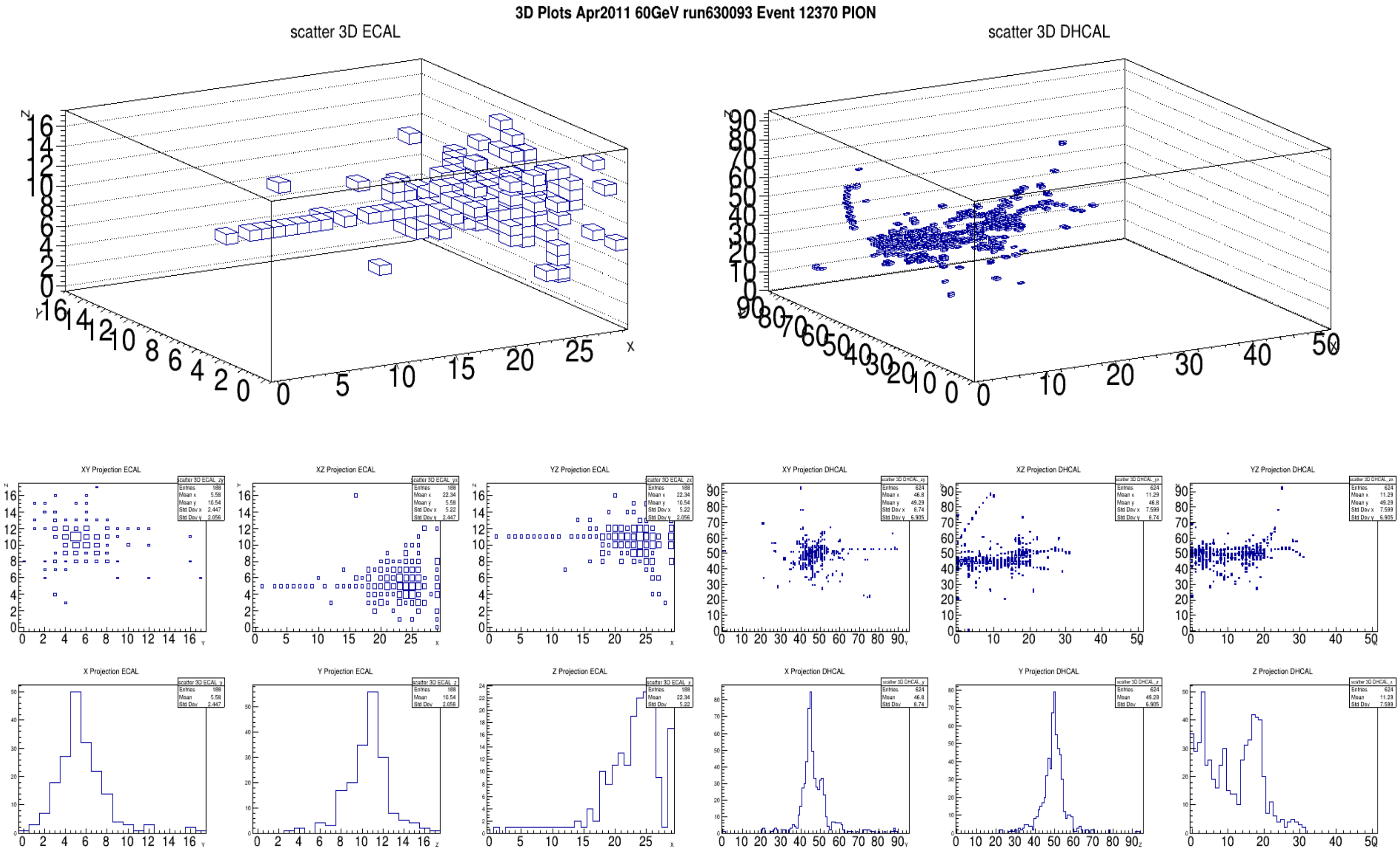

Figure 8.1: Example of a typical early showering pion event for an April 2011 test run at 60 GeV. The top plots show the path of the incoming positron starting on the left (first layer of Si-W ECAL and continuing a straight trajectory until reaching starting a shower. The shower is partly contained by ECAL and continues its development until reaching the first layers of DHCAL, which is shown on the plot on the right. The rest of the shower is then fully contained in DHCAL. The first three histograms on the second row show the XY, XZ and YZ projections of the hits in ECAL respectively. The next three histograms of the second row show the XY, XZ and YZ projections of the hits in DHCAL respectively. The bottom row shows 1D histograms of the X, Y and Z distributions of hits in the event respectively. The first three histograms correspond to the ECAL 1D projections and the following three to DHCAL.

8.1 Types of hadronic showers for the April 2011 testing period

After separating the particles using the cuts explained in section 6.2, the hadronic showers can be separated into two types. These can be easily identified in the ECAL+HCAL Standard Plots. The first type which we have named "Early showering pions" are the hadronic showers which start within ECAL, so that their counted hits are distributed between the two detectors. A typical event for this type of shower can be seen in Figure 8.1.

The second type of event are the "Late showering pions" in which the hits in ECAL are only attributed to the minimum ionizing track of the particle and the hits in DHCAL contain the totality of the shower (shown in Figure 6.6). Due to this behaviour of the hadronic particle, the particle ID has to be performed setting cuts in a mix of parameters from both detectors. This was not possible since the ECAL data was not available for energies below 50 GeV. The only particle ID doable at these energies was to separate muons and late showering pions from the rest of the events which are known to have left part of their energy in the ECAL.

8.2 Linearity analysis

The following analysis was performed for both testing periods. For each run, a Gaussian function was fitted to the hit distribution of DHCAL after selecting only contained showers. An example of the fitted distribution can be found in Figure 8.2. For hadronic showers, which penetrate deeper into the detector, the containment condition was to have less than two hits in the last two layers of DHCAL, while for electromagnetic showers the condition was applied for the last ten layers. With the containment condition, the sample for 120 GeV was reduced by 40% for pions and 50% for positrons.

After plotting the histograms for the hits distribution, it was noticeable that at energies below 16 GeV the number of pion events was too small to be able to fit a Gaussian function. These energies were therefore discarded from the linearity analysis.

The Gaussian fits were performed to all runs from all remaining energies. The mean number of hits for each run was found, as well as the standard deviation of the distribution. These parameters were then analyzed separately for each energy after confirming that all runs of the same energy gave results compatible with each other. A final average of the mean hits was obtained for each energy group given by linear fits to the mean hits distribution of all runs with the same energy, this distribution is shown in Figure 8.3 for the 40 GeV set of data.

The average mean number of hits for positrons and pions in the June 2011 testing period was plotted against the beam energy in Figure 8.4. It can be observed that both distributions have signs of saturation effects for large energies. The data points were fitted to a linear function (Equation 8.1) only in the beam energy range of 0 to 60 GeV, then, the function was projected to 120 GeV to guide the eye. An exponential fit following Equation 8.2 was performed to the data points, this shows a measurement of the saturation in comparison to the linear fit expected for a detector without saturation at high energies. The results of the exponential fit can be seen in Table 8.1 for June 2011 and in Table 8.2 for April 2011. The April 2011 plot only contains information for hadronic events since these

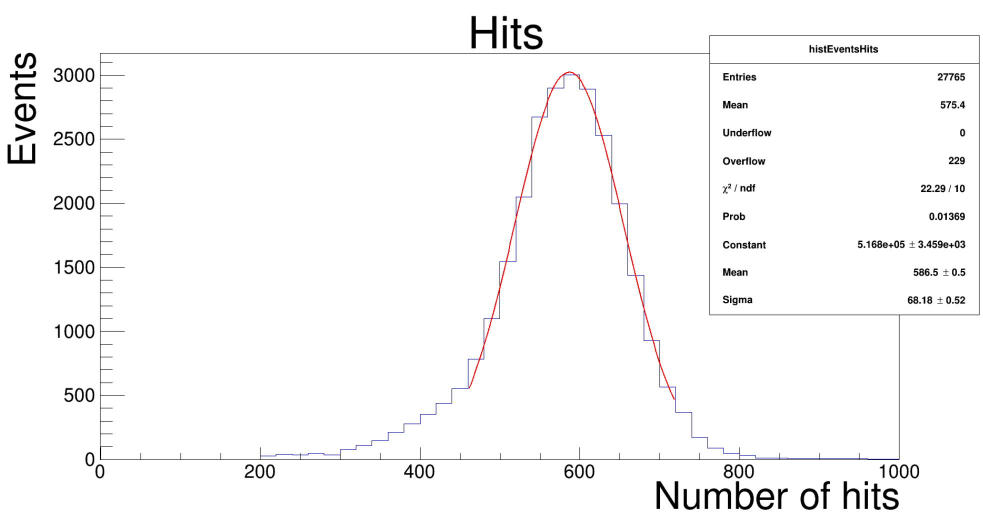

Figure 8.2: Example of a Gaussian fit to the hits distribution of electromagnetic showers for a 40 GeV test run from June 2011, the fit only covers bins higher than 15% of the height of the peak.

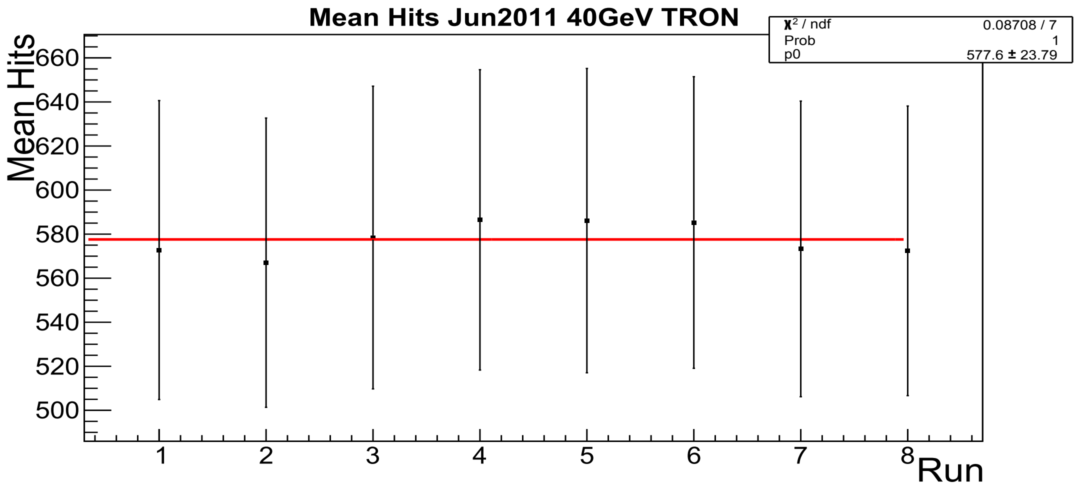

Figure 8.3: Distribution of mean number of hits for all available 40 GeV test runs from the June 2011 testing period. The error bars represent the standard deviation from the Gaussian fits to the hits distributions rather than the error on the mean as this was measured to be less than one hit.

were the only type of shower fully observable in the DHCAL when the Si-W ECAL was in front.

$$N_{Hits} = p_0 E_{Beam} \tag{8.1}$$

$$N_{Hits} = p_0 {E_{Beam}}^{p_1} \tag{8.2}$$

As explained before, the only events studied for the April 2011 testing period were hadronic events which start their shower in DHCAL.

It was not possible to study the linearity of the Si-W ECAL or the combined Si-W ECAL + DHCAL system due to the absence of an active ECAL data from most of the test runs. Saturation effects were observed at high beam energies in DHCAL in both studied data sets, which is expected for energies above 60 Gev.

Taking the linear fits as the "expected" behaviour of the detectors without saturation, the measured mean number of hits for positrons at 120 GeV represents 85 ± 4 % of the expected value, the same percentage was found for the pions of the same testing period. For the April 2011 late showering pions, the hits response at 120 GeV was calculated to be

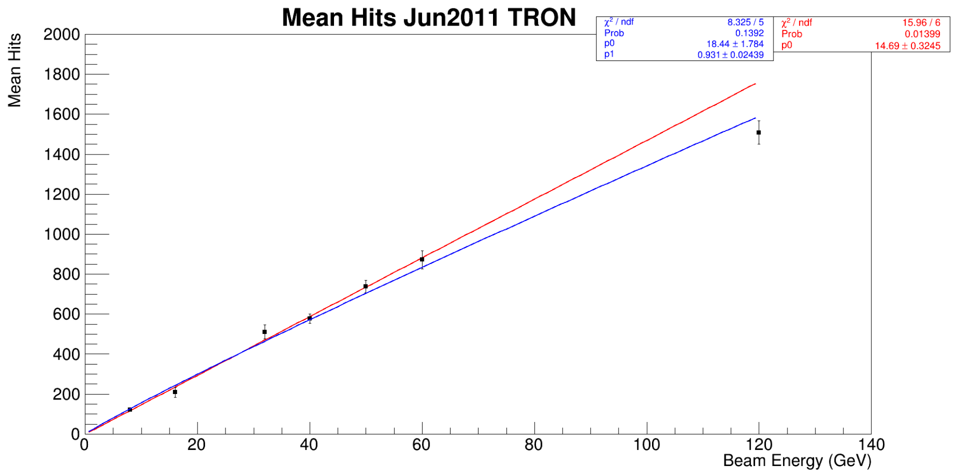

(a) Positrons

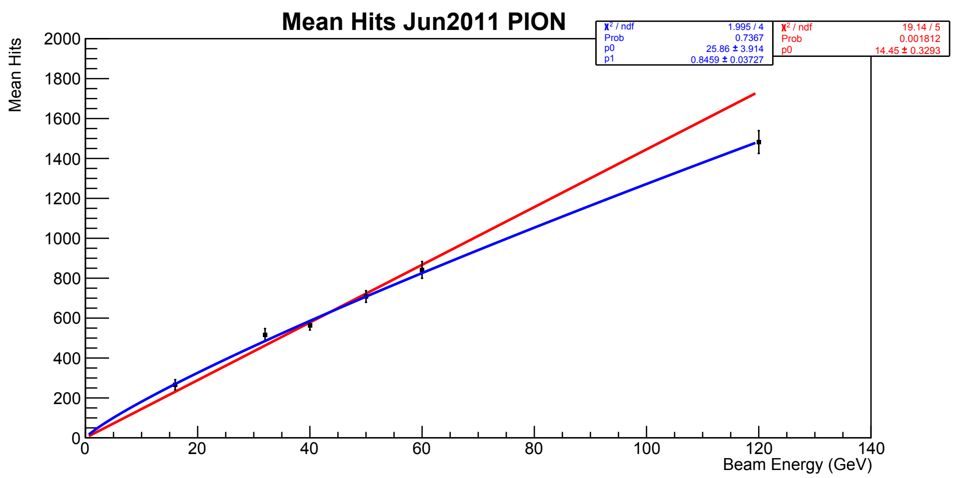

(b) Pions

Figure 8.4: Linearity for electromagnetic and hadronic showers in the June 2011 testing period. In both figures, the red line represents a linear fit from 0 to 60 GeV given by Equation 8.1 to guide the eye and the blue line represents an exponential fit given by the function in Equation 8.2

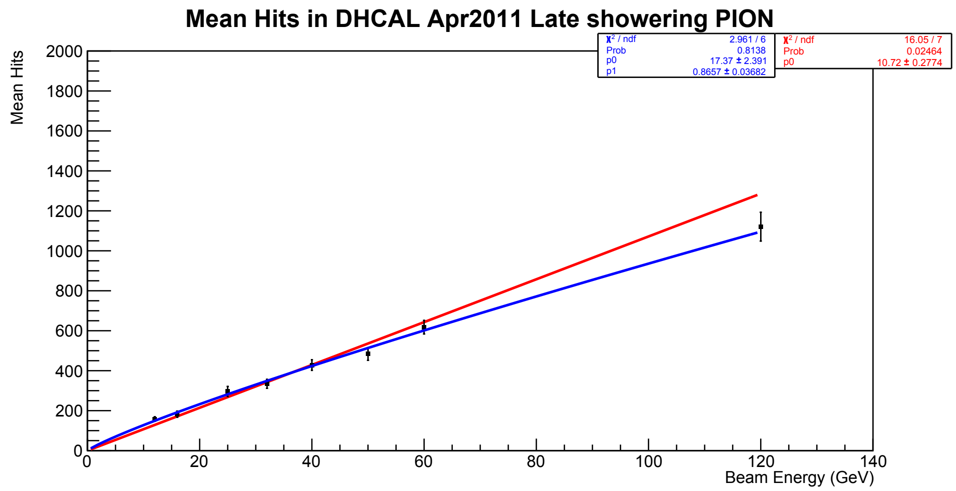

Figure 8.5: Linearity for hadronic events in the April 2011 testing period, which start their shower within DHCAL (late showering pions). The red line represents a linear fit given by Equation 8.1 and the blue line represents an exponential fit given by the function in Equation 8.2

Results Linearity June 2011		
Particle	p0	p1
Positron	18.4 ± 1.8	0.931 ± 0.024
Pion	25.9 ± 3.9	0.846 ± 0.037

Table 8.1: Linearity results for June 2011. The parameters p0 and p1 represent the variables constants from Equation 8.2 and were obtained by performing a fit to the data of Figures 8.4a and 8.4b.

87 ± 6 % of the expected value for an ideal linear calorimeter. These results show that the digital calorimeter has consistent saturation for the two types of particle showers at beam energies higher than 60 GeV. Typically, electromagnetic showers are expected to show a larger saturation effect than hadronic showers.

The saturation for the DHCAL physics prototype is also consistent within different testing periods. Overall, the saturation for hadronic showers in both testing periods are compatible with each other, which is expected since the same DHCAL configuration was used. A small reduction in the mean number of hits can be observed from the April 2011

Results Linearity April 2011		
Particle	p0	p1
Late showering Pion	17.4 ± 2.4	0.866 ± 0.037

Table 8.2: Linearity results for April 2011. The parameters p0 and p1 represent the variables constants from Equation 8.2 and were obtained by performing a fit to the data of Figure 8.5.

pions with respect to the pion events from June 2011, this can be attributed to the hits from the MIP track, where in the case of April 2011 these are detected mostly by the ECAL.

The results of the linearity for both testing periods will be used as a calibration for the detectors energy measurement in Chapter 9.

Chapter 9

Energy Analysis

As previously explained in Section 5.2.3, the Digital Hadronic Calorimeter (DHCAL) is a type of calorimeter which only counts the cells hit without providing any measurement of the energy deposited by the particles. The DHCAL records a time stamp of the ”hit” and the coordinates X, Y and Z of the cell, being Z the number of a layer in the detector configuration. The type of signal output from DHCAL is where it gets its name as a ”digital calorimeter”. Given that there is no direct measurement of the particles' energies, the main idea of the prototype is that the energy of a shower can be reconstructed from the total number of hits in one event. In the case of the April 2011 testing period, the energy measurement from the Si-W ECAL and the known beam energy will be used to improve the calibration factor to measure DHCAL energy from the number of hits in an event.

9.1 Calculation of energy deposited in ECAL absorber

The Si-W ECAL does measure the energy of the particles. Each hit in the Si-W ECAL has the information of the energy lost by the particle when passing through the silicon in the cell as well as the coordinates of the cell. The energy lost in the tungsten absorber can be estimated from the energy lost in the silicon. The Si-W ECAL has three sections of 10 layers with increasing thicknesses for the absorber, therefore, the energy lost in the tungsten is a function of the Z coordinate of the hit.

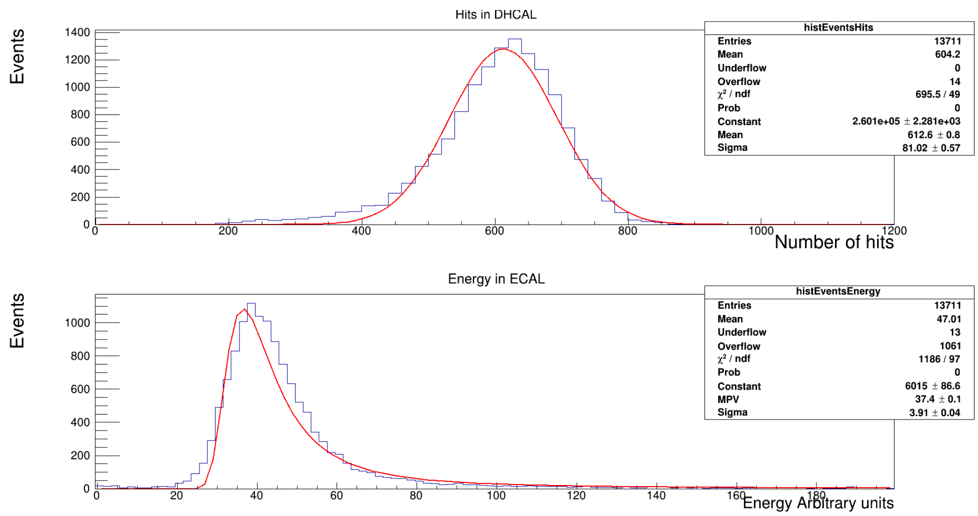

Figure 9.1: Hits distribution in DHCAL (top) and MIP Silicon energy distribution for Si-W ECAL (bottom) for a 50 GeV test run. The first is fitted a Gaussian function and the second a Landau function. The MIP Silicon energy distribution is presented in arbitrary units.

The radiation lengths, from [31], were used to estimate the energy lost in the tungsten from the energy lost in the silicon. The radiation length of silicon is $X_0^{Si} = 9.370$ cm, while the one for tungsten is $X_0^W = 0.3504$ cm. If we divide the radiation lengths of the materials to find the ratio between them we have

$$\frac{X_0^{Si}}{X_0^W} = \frac{9.370cm}{0.3504cm} = 26.74, \tag{9.1}$$

this means that a particle needs 26.74 times the distance traveled in tungsten to lose the same energy traveling through silicon. In other words, the energy is lost 26.74 times faster in tungsten than in silicon in terms of distance traveled by the particle in the material. Knowing this ratio of energy loss, we can find the energy deposited in the tungsten by the measurement of energy lost in the $525\ \mu m$ of silicon from the PIN diode (in arbitrary units at this stage). Let us call the energy measured by the silicon pad E_{Si}, then

$$E_W = \frac{1.4mm}{525\mu m} \times 26.74 E_{Si} = 73.344 E_{Si}, \tag{9.2}$$

where E_W is the average energy lost in 1.4 mm of tungsten. The three different thicknesses of absorber layers are multiples of 1.4 mm, therefore, to calculate the energy deposited by the a particle in the second or third stack of the ECAL layers the result from Equation 9.2 has to be multiplied by a factor of 2 or 3 respectively.

The total energy of a hit is calculated by adding E_{Si} and E_W.

9.2 Conversion of measured energy to MeV units

The hit data from the ECAL contains a measurement of the energy in arbitrary units. The conversion between these data units and actual energy units had to be established. To find the conversion factor the silicon energy distribution of late showering pions in a test run was studied. In Figure 9.1 we can observe that the silicon energy distribution for a 50 GeV test run has a peak around 38 data units. The peak corresponds to the minimum ionizing track of late showering pions. The minimum ionizing energy in silicon found in [31] is $3.876\ MeV cm^{-1}$, assuming that a MIP crosses the full length of the ECAL detector then the energy deposited by one MIP in 30 layers of $525\ \mu m$ of silicon is $E_{MIP} = 6.1047\ MeV$. The silicon energy distributions for all test runs were fitted a Landau function. An average of the most probable values was extracted from the linear fit in Figure 9.2. The result of the average MIP energy was found to be 37.55 ± 1.48 Data Units. The relation between the arbitrary data units and MeV is then

$$DataUnit = \frac{E_{MIP}}{Average_{MPV}} = \frac{6.1047 MeV}{37.55} = 0.1626 MeV \tag{9.3}$$

With the average MIP value, we can calculate the energy measured by the silicon in MeV for any hit in the detector. Using Equation 9.2, the total energy lost by the particle can be calculated.

After using equations 9.2 and 9.3, the energy distribution for ECAL can be plotted once again using the right units. In Figure 9.3 we observe an example for a 50 GeV test run which has all events for pions. The first peak on the left side of the ECAL energy distribution is associated to the MIP track of the late showering pions, while the second

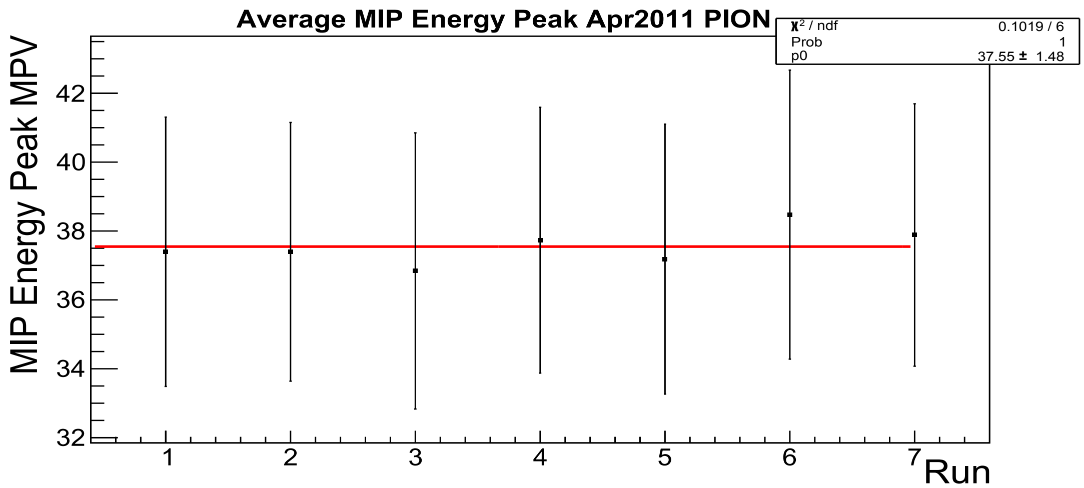

Figure 9.2: MPV from Landau fit to the silicon energy distribution of each available April 2011 test run. The first point from left to right corresponds to the 50 GeV test run: 630081; the following four points to 60 GeV runs: 630090, 630091, 630092, and 630093 respectively; and the final two points to 120 GeV runs: 630095 and 630097 respectively.

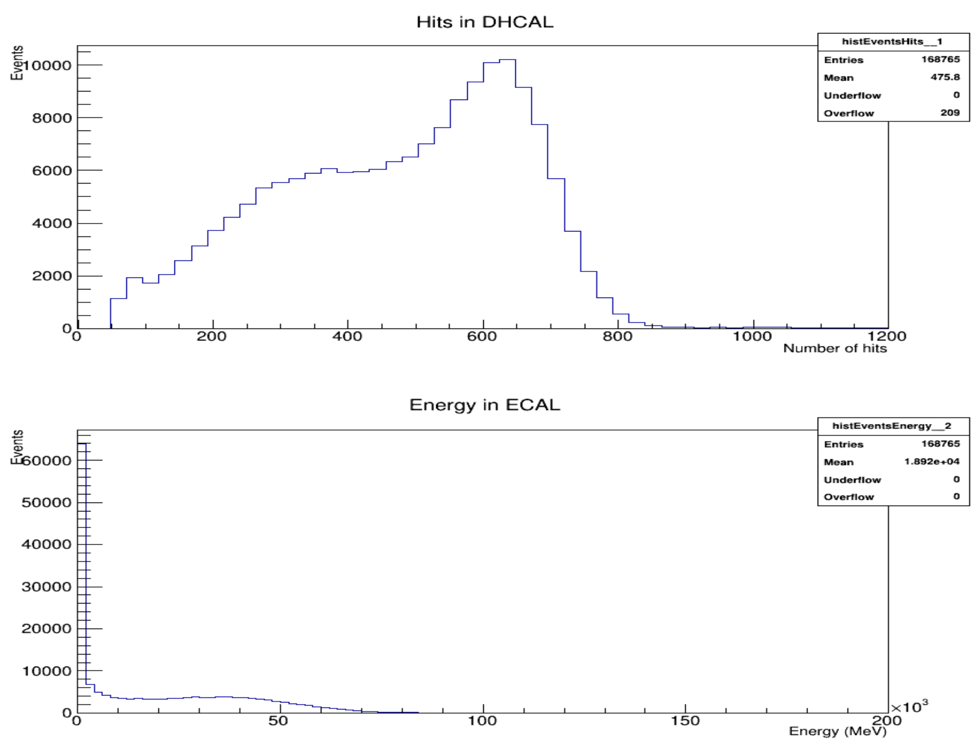

Figure 9.3: Hits in DHCAL (top) and Energy in ECAL (bottom) Distributions for all pions in the 50 GeV test run.

peak just below 50 GeV corresponds to the part of the shower deposited in ECAL by the early showering pions. It is also noticeable that the DHCAL hits distribution presents three bumps. The connection of the bumps in the hit distribution in DHCAL comes clear from the expected number of hits in a hadronic shower. The early showering pions will leave part of their shower in ECAL, therefore, it is expected to have a decrease in the number of hits in DHCAL (bump in the middle). The second peak, at a higher number of hits represents the events where the total shower is contained within DHCAL.

For the next section, the MIP track peak will be removed by a cut on the number of hits in ECAL. By applying this cut we will be able to study only the early showering pions and use them find the combined energy response of the Si-W ECAL + DHCAL system.

9.3 Calculation of energy deposited in DHCAL

Having proper energy units for the ECAL data, the next step is to find the energy deposited in the DHCAL.

For events were the shower hits are distributed between the two calorimeters, the total energy measured must be equal to the energy of the beam. From Figure 9.4, we can observe that after discarding the late showering pions both the hits in DHCAL and the energy in ECAL appear to be roughly Gaussian shaped. In the case of Figure 9.4, the mean of the energy distribution in ECAL sits at around 37 GeV which means that about 13 GeV of the energy are measured by hits in the DHCAL for the events around the mean.

Correlation plots like the one shown in Figure 9.5 were created to better understand the distribution of energy between the two calorimeters. In the scatter plot the coordinates of each point are the event total energy in ECAL and the Number of hits in DHCAL. From these plots it can be observed that the calibration for the energy in ECAL is still incomplete, as in the events without hits in DHCAL the energy distribution for ECAL is not centered around 50 GeV. The calibration of the energies in both calorimeters will be explained next.

It is clear that in an ideal experiment with no variation in the beam energy the plot in Figure 9.5 would be a straight line crossing the horizontal axis at 50 GeV and the vertical

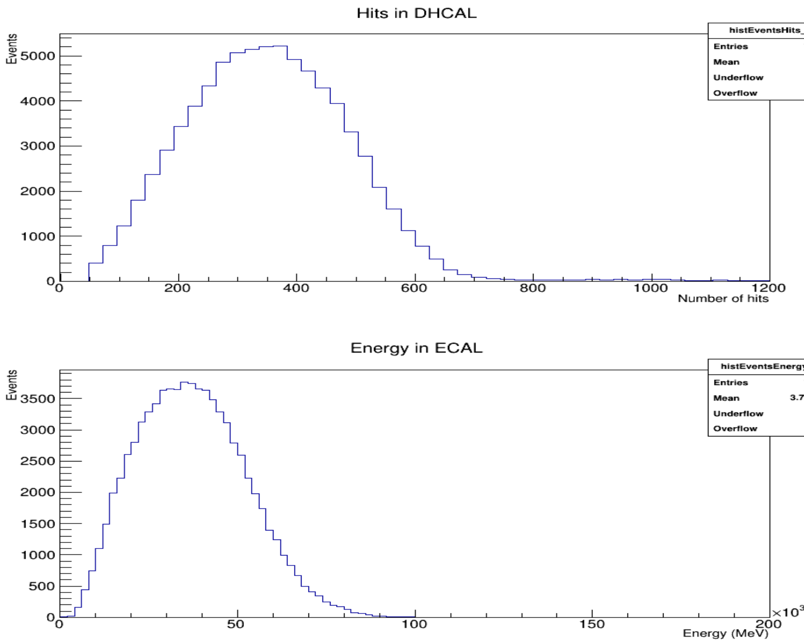

Figure 9.4: Hits in DHCAL (top) and Energy in ECAL (bottom) Distributions for early showering pions in the 50 GeV test run.

at a number of hits equivalent to 50 GeV. Of course, since both the hits in DHCAL and Energy in ECAL distributions (from Figure 9.4) are Gaussian shaped, there is a smearing in this line. The smearing in the distribution from the main line is where the energy resolution will be obtained from.

The scatter distribution on the left of Figure 9.5 has an elliptic shape in this color projection. If one takes the distribution and plots it as a regular 2D plot, then the shape of the distribution becomes the concave paraboloid seen on the right of Figure 9.5.

The shape of the distribution facilitated finding the two main axes of the paraboloid by applying a fit to a paraboloid function. The 2D function fitted to the distribution is shown in Figure 9.6. The equation of the fit is a rotated paraboloid function which is written as

$$z(x,y) = \frac{((x-h)\sin\theta + (y-k)\cos\theta)^2}{a^2} + \frac{((x-h)\cos\theta - (y-k)\sin\theta)^2}{b^2} \tag{9.4}$$

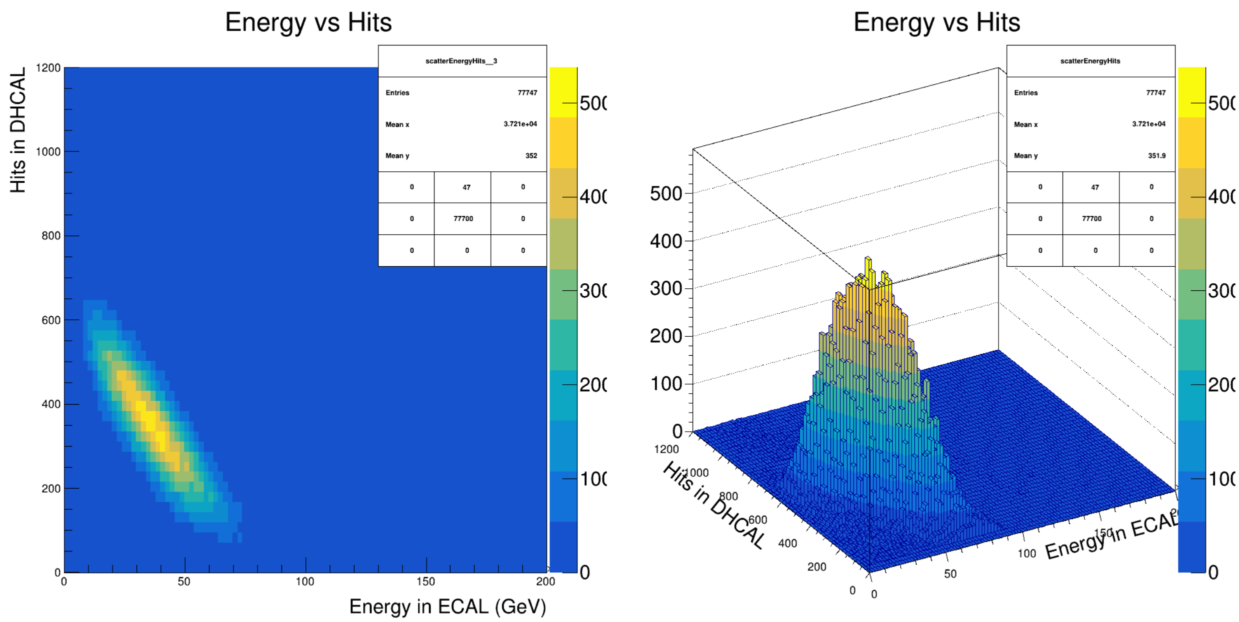

Figure 9.5: Scatter plot of the Hits in DHCAL vs Energy in ECAL Distributions for early showering pions in a 50 GeV test run. On the left is the color projection and on the right the LEGO view.

where the parameters h and k are the coordinates of the center in x (Energy in ECAL) and y (Hits in DHCAL) respectively, a and b are the semi-axes and θ is the rotation angle which is measured from the horizontal axis. From the parameters, only the center of the paraboloid and the rotation angle with respect to the horizontal axis were used. With these parameters a linear function was found for the major axis. The linear function was calculated as follows

$$Hits_{DHCAL} = \tan\theta\,(Energy_{ECAL} - h) + k \tag{9.5}$$

The intersections with the Energy in ECAL and Hits in DHCAL axes were calculated from Equation 9.5. They are shown in Table 9.1.

The fitted distribution and the contour projection of the fit are shown in Figure 9.7, in this type of projection it is easier to appreciate the main axes of the paraboloid by the ellipses formed by the contours at different z. It is also important to mention that the scatter points outside of the main distribution in the Energy vs Hits plot from Figure 9.7

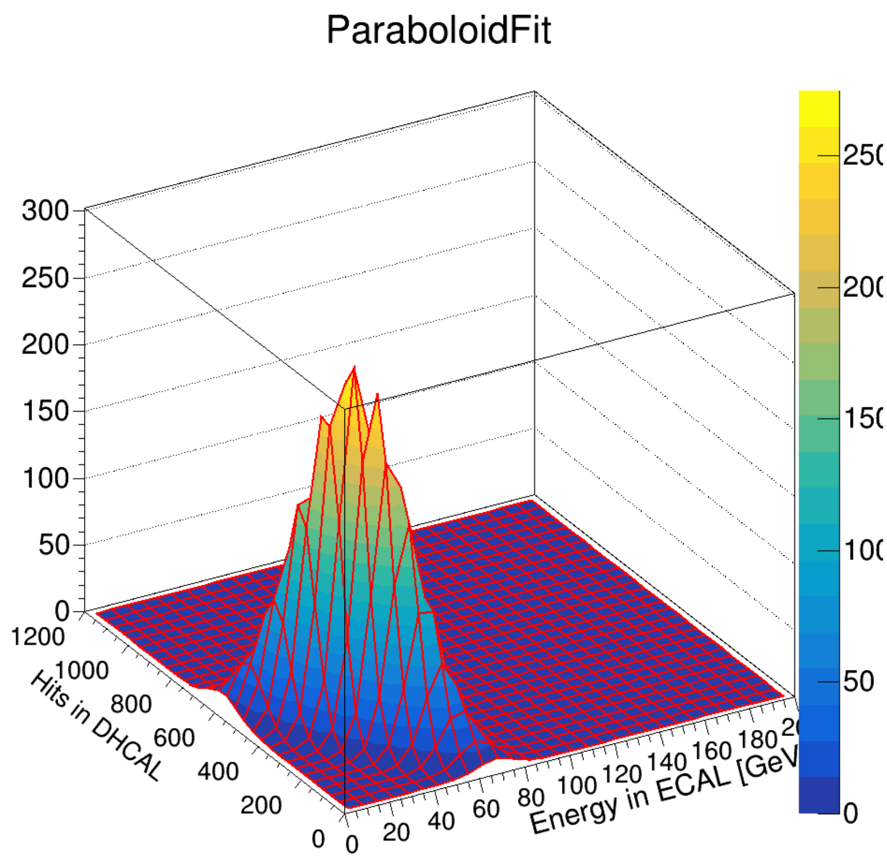

Figure 9.6: Paraboloid function fitted to the Scatter plot of the Hits in DHCAL vs Energy in ECAL Distributions for early showering pions in the 50 GeV test run. The plot shows the 2D function from Equation 9.4, the peaks at the top are due to the binning of the axes.

are related to double events which are events were two pions interacted with the detectors at the same time. These events are automatically discarded from the fit, as can be seen in Figure 9.6.

For the three energies studied the results are shown in Table 9.1, in which X is the intersect with the horizontal axis (Energy in ECAL) and Y is the intersect with vertical axis (Hits in DHCAL). The columns Beam Energy/X and Beam Energy/Y are the calculated correction factors which multiply every entry of number of hits in DHCAL and Energy in ECAL for an event.

After multiplying the run data by its respective correction factors, the Energy in DHCAL and the now completely calibrated Energy in ECAL distributions were found. The cali-

	Si-W ECAL		DHCAL	
Beam Energy	X (GeV)	Beam Energy/X (No units)	Y (Hits)	Beam Energy/Y (GeV/Hits)
50 GeV	77 ± 5	0.65 ± 0.04	677 ± 46	0.074 ± 0.005
60 GeV	95 ± 27	0.63 ± 0.18	841 ± 239	0.071 ± 0.02
120 GeV	208 ± 79	0.58 ± 0.22	1545 ± 588	0.078 ± 0.03

Table 9.1: The X and Y values are the intersections with horizontal and vertical axes for all available energies respectively. The correction factors used to calculate the energies of both detectors are also shown. The first row shows the parameters calculated for the 50 GeV test run, the second run shows averages of the parameters from the four 60 GeV test runs studied, and the last row shows the averaged parameters from the two 120 GeV test runs.

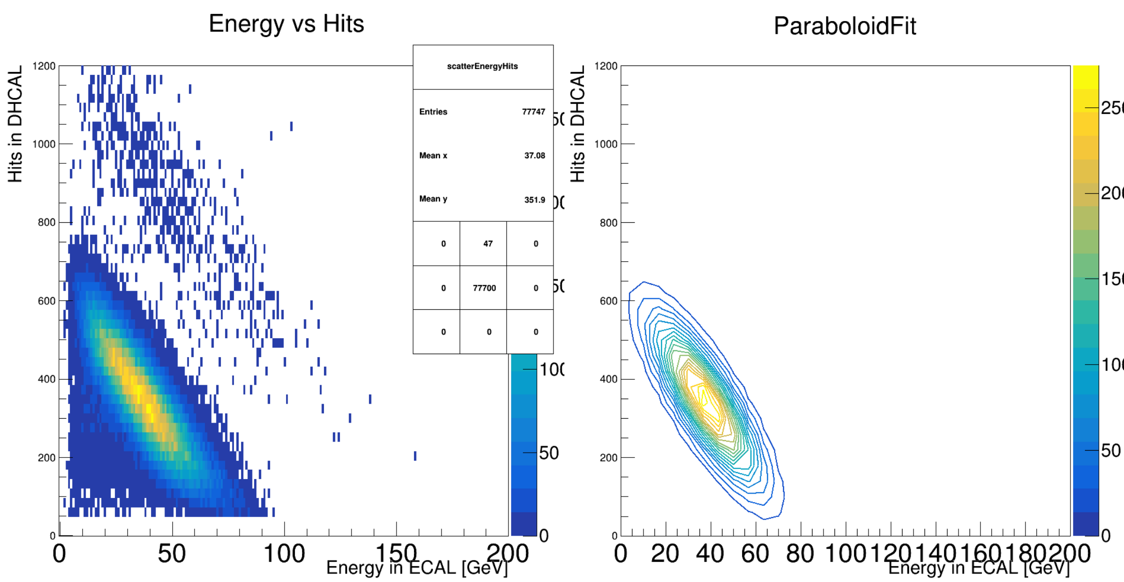

Figure 9.7: On the left: Scatter plot of the Hits in DHCAL vs Energy in ECAL Distributions for early showering pions in a 50 GeV test run. On the right: Contour projections of the paraboloid function fitted to the distribution on the left.

brated energy distributions are shown in Figure 9.8. These distributions tell us how the energy is distributed between the ECAL and HCAL.

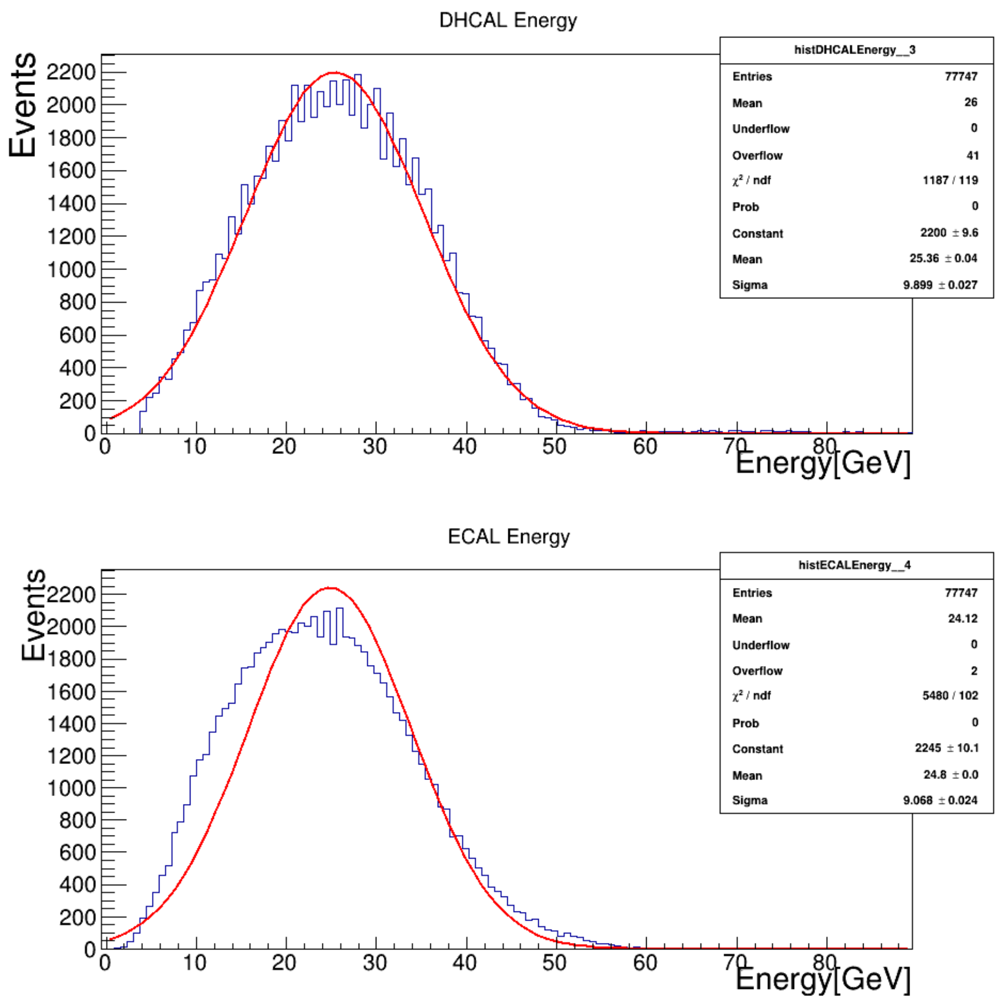

Figure 9.8: Energy in DHCAL and Energy in ECAL Distributions for early showering pions in the 50 GeV test run. Both red lines are Gaussian fits to guide the eye.

9.4 Hadronic and electromagnetic energy resolution for June 2011 data

The energy resolution is a parameter found to measure how precisely a detector can resolve energies or to measure the precision of energy measurements. Therefore it is a parameter which needs to be minimized with the creation of new particle detection technologies.

The energy resolution of the standalone DHCAL was studied using the June 2011 data. The method to find the conversion from hits to energy is completely different as the one for the April 2011 data, as there was no ECAL present in the testing period. Starting from the linearity results of Chapter 8. The energy of the shower as a function of the number of hits is calculated as

$$E = \left(\frac{N_{Hits}}{p_0} \right)^{\frac{1}{p_1}}, \tag{9.6}$$

where E is the energy of the event, N_{Hits} is the number of hits from the event, and the parameters p_0 and p_1 come from Equation 8.2, which is the inverse of this equation. Therefore, the saturation effect found for each type of particle is taken into account in this calculation. This equation was used to find the energy distribution of each available test run. An example of the energy distribution of positrons in a 50 GeV test run is shown in Figure 9.9.

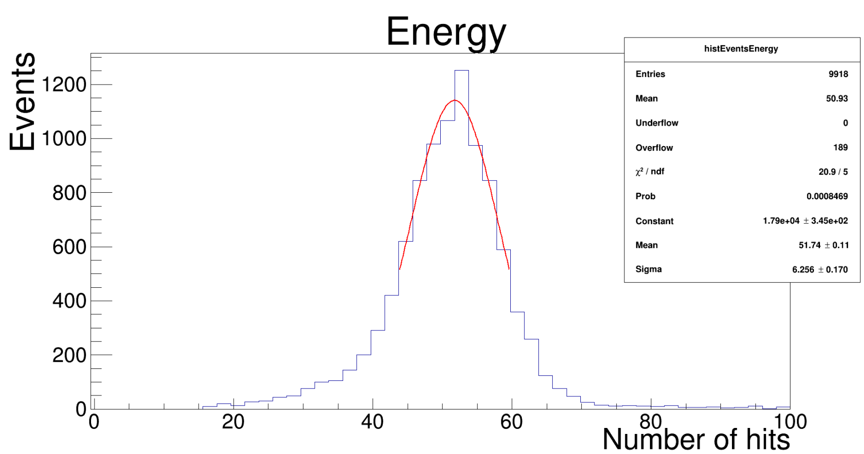

Figure 9.9: Energy distribution of positrons for a 50 GeV test run from the June 2011 testing period. The red line represents a Gaussian fit covering only bins higher than 30% of the height of the peak.

With the parameters of the fit to the energy distribution, the energy resolution was calculated as

$$Resolution = \frac{\sigma}{E_{Mean}}, \tag{9.7}$$

where σ and E_{Mean} are the standard deviation and mean from the Gaussian fit respectively. The overall resolution of a detector is affected by a number of factors. These include the fluctuations in ionization and electronics noise.[8]

The resolution of a detector as a function of the beam energy can in general be represented by the empirical equation

$$\frac{\sigma}{E} = \frac{a}{\sqrt{E}} \oplus \frac{b}{E} \oplus c \tag{9.8}$$

where the first and main term is of stochastic nature and the second and third terms represent the systematic and constant errors respectively. The systematic error is usually associated to electronics noise, leakage, dead material, and other similar phenomena. The energy resolution was calculated using Equation 9.7. The relevant parameters from the energy distribution are the standard deviation and the mean. The testing period consisted of a data set of 45 test runs, ranging from 8 GeV to 120 GeV, the number of test runs and number of events for each beam energy is available in Table 6.2. The standard deviation and mean for each energy were obtained by averaging over all the available test runs of the same energy after confirming that they were compatible with each other. The results of the energy resolution for this period are listed in Table 9.2 for positrons and pions. By comparing the resolution individually for the shared energies between the two

Results Energy Resolution June 2011		
Beam Energy	e^+Resolution	π^+Resolution
8 GeV	0.174 ± 0.004	
16 GeV		0.212 ± 0.003
32 GeV	0.148 ± 0.001	0.153 ± 0.002
40 GeV	0.123 ± 0.001	0.141 ± 0.002
50 GeV	0.120 ± 0.001	0.135 ± 0.002
60 GeV	0.126 ± 0.001	0.146 ± 0.002
120 GeV	0.119 ± 0.001	0.133 ± 0.002

Table 9.2: Energy resolution results for positrons and pions of the June 2011 testing period. The blank spaces represent energies which could not be fitted to Gaussian function properly. These energies were therefore excluded from the analysis.

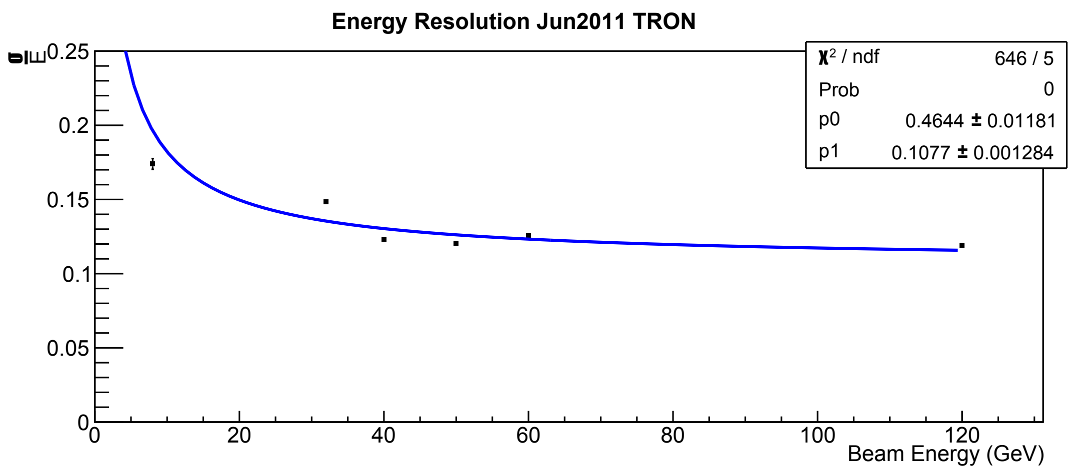

(a) Positrons

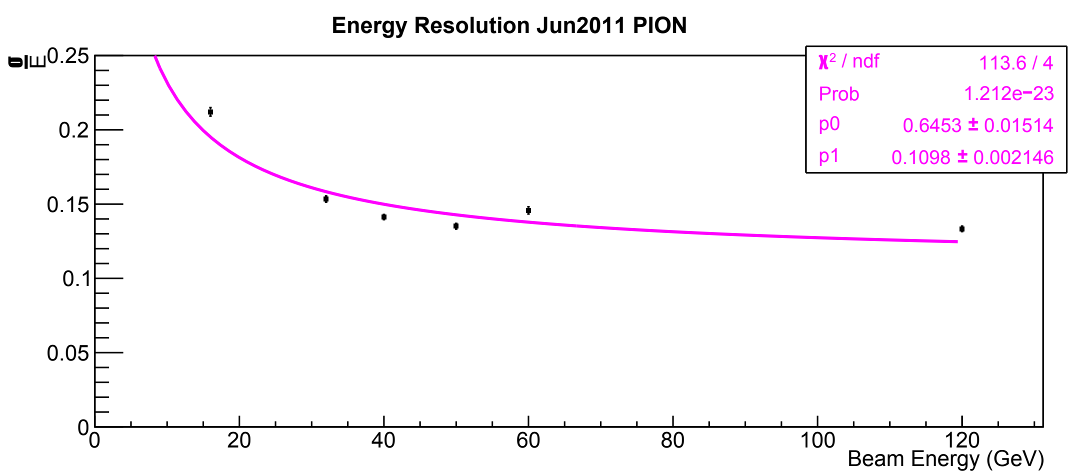

(b) Pions

Figure 9.10: Energy resolution for electromagnetic and hadronic showers in the June 2011 testing period. In both figures, the line represents the fit to Equation 9.8 setting the parameter b to zero.

data sets it can be observed that the DHCAL setup presents a better resolution for the electromagnetic showers.

The beam energies of 8 GeV for pions and 16 GeV for positrons were removed from the energy study. For low energies, the peaks in the number of hits distribution for particle showers were too close to the peak caused by the muons and could not be disentangled. Therefore, when making the cuts for the particle identification, the showers hits distributions are missing the left side of the Gaussian tail. In most cases, the missing left tail made it impossible to fit a Gaussian function to the top 85% of the height of the peak.

The data points for positrons and pions from Table 9.2 were each fitted to Equation 9.7 setting $b = 0$. At first, the energy resolution fits were performed for the two types of particles using all three parameters (a,b, and c) but in all fits the parameter b was found to be compatible with zero as can be deducted from the flatness of the high energy part of the distributions in Figures 9.10a and 9.10b. It was therefore decided to perform the fits once again setting $b = 0$. The resulting fit is shown in Figure 9.10a for positrons and Figure 9.10b for pions.

The energy resolution of the Si-W ECAL + DHCAL system will be discussed in the following section, for this data it was chosen to keep the parameter $b = 0$ due to the small amount of beam energies available (three energies). In this way, the two testing periods can be compared in terms of the other energy resolution parameters, a and c.

Table 9.3 shows the results of the fits to the distributions in Figure 9.10. The results show a better resolution of the electromagnetic showers compared to the hadronic showers. This results will be compared with the performance of the detector set up from April 2011 in the following section.

Table 9.3: Energy resolution parameters of the June 2011 testing period for positrons and pions.

Particle type	a($GeV^{\frac{1}{2}}$)	c
Positron	0.46 ± 0.01	0.108 ± 0.001
Pion	0.64 ± 0.02	0.110 ± 0.002

9.5 Hadronic energy resolution of the Si-W ECAL + DHCAL system

Two methods were used to calculate the combined energy resolution of the detectors.

9.5.1 Diagonal Fit Method

The first method used was to make a scatter plot like the one in Figure 9.5 but with the calibrated event energies. The scatter plot for the first method is shown on the left in Figure 9.11.

The plot on the right in Figure 9.11 is a projection of the distribution on the left across its main axis. The projection was fitted to a Gaussian function to estimate the smearing of the data points from the ideal straight line that crosses both axes at 50 GeV.

The results from the first method are listed in Table 9.4 for all available energies. The systematic errors were not calculated.

For the 50 GeV row in Table 9.4, the results come directly from the one available test run. The results for 60 GeV and 120 GeV row of the same table are averaged from the four and two available test runs for each energy respectively.

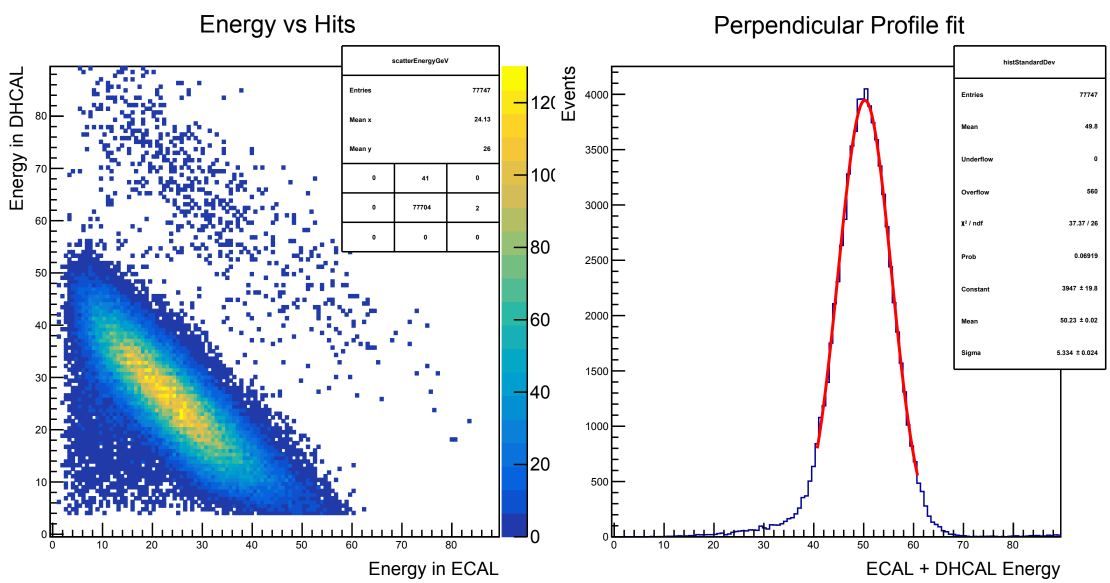

Figure 9.11: On the left: Scatter plot of the Energy in DHCAL vs Energy in ECAL Distributions for early showering pions in the 50 GeV test run. On the right: Histogram of the diagonal projection of the distribution on the left.

Beam Energy	Energy Resolution	a($GeV^{\frac{1}{2}}$)
50 GeV	0.1061 ± 0.0005	0.750 ± 0.004
60 GeV	0.095 ± 0.003	0.740 ± 0.006
120 GeV	0.071 ± 0.001	0.780 ± 0.008

Table 9.4: Energy resolution results for the Si-W ECAL + DHCAL system in the April 2011 test period from the diagonal fit method. The parameters b and c were set to zero.

9.5.2 Sum of Energies Method

The second method to calculate the energy resolution was to add the energies from both detectors. In this way, we can compare if the calibration of the energy scales for the two calorimeters coincide with the beam energy. The distribution of the total energy for the calorimeters is shown in Figure 9.12 for the 50 GeV test run. The results for the energy resolution using the second method are listed in Table 9.5. Comparing the results for the two methods, it is observed that the two are compatible with each other, as expected.

Beam Energy	Energy Resolution	a($GeV^{\frac{1}{2}}$)
50 GeV	0.1062 ± 0.0005	0.751 ± 0.004
60 GeV	0.097 ± 0.003	0.748 ± 0.007
120 GeV	0.072 ± 0.001	0.784 ± 0.008

Table 9.5: Energy resolution of the combined Si-W ECAL+DHCAL system for early showering pions in the April 2011 period, obtained from the sum of energies method. The parameters b and c were set to zero.

The energy resolution for early showering pions as a function of the beam energy is shown in Figure 9.13. Fitting the energy resolution points to Equation 9.8 with b=0, the general terms a and c were calculated for the April 2011 testing period. The resulting stochastic term for the period is $a = 0.723 \pm 0.008$, with $c = 0.026 \pm 0.004$. This general result is consistent with the individual stochastic terms for each one of the three available energies.

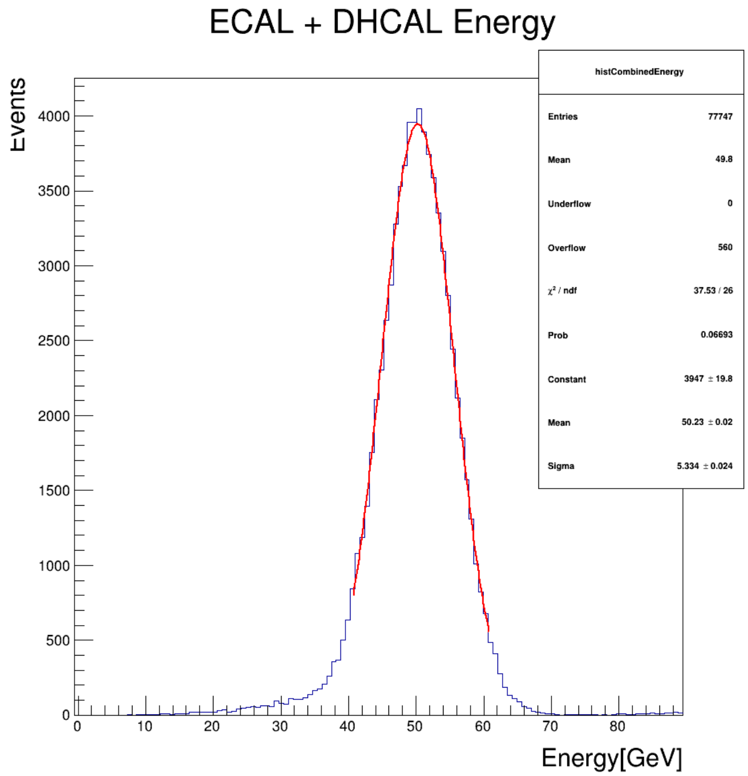

Figure 9.12: Total energy distribution for the 50 GeV test run from the April 2011 testing period. Each entry is calculated from adding the energies measured by ECAL and DHCAL in the same event.

9.5.3 Energy resolution comparison between the June 2011 and April 2011 data

To fairly compare the resolution results obtained for the June 2011 period with the April 2011 period, the energy resolution for late showering pions (DHCAL only) was calculated with two methods. The first one is the same used in section 9.4 for the June 2011 data. The parameters used for Equation 9.6 are the ones obtained from the exponential fit in Figure 8.5. The results of this method can be seen in Figure 9.14.

The second method consists on making the conversion from number of hits to energy using the correction factor from Table 9.1. The results from this method are shown on the plot from Figure 9.15. In Table 9.6, it can be observed that the second method gives the best energy resolution results. This means that the linear relation found between energy

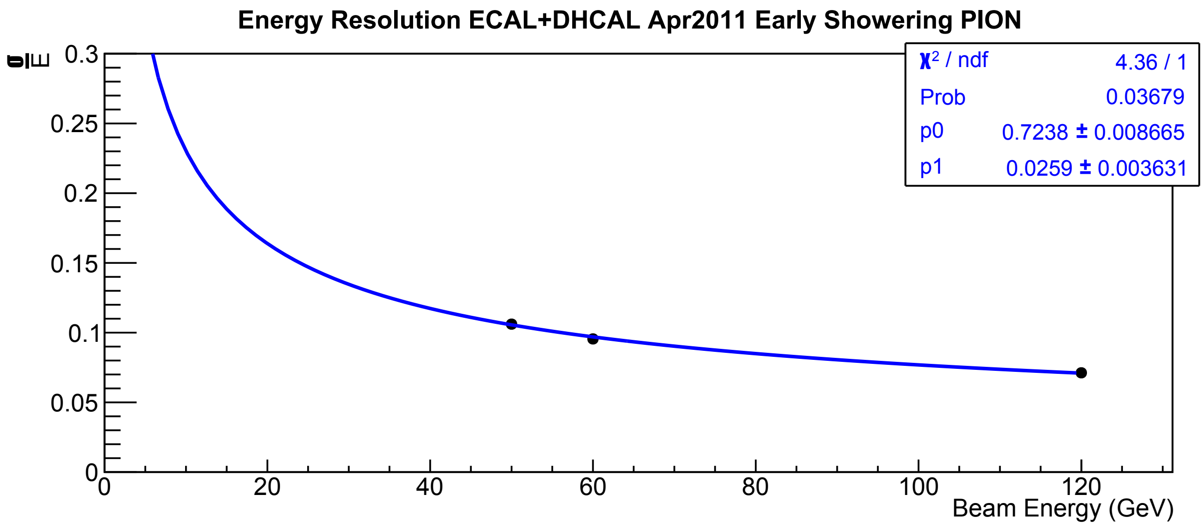

Figure 9.13: Hadronic energy resolution of the combined Si-W ECAL + DHCAL system. The fitted function is found in Equation 9.8. The parameter a is the stochastic term from Equation 9.8. The parameter b is set to zero in the fit.

and hits for DHCAL is a better correction factor than the exponential function from the linearity fit. The correction factor for DHCAL to convert hits to energy can be used for any hadronic shower measured in the detector of the same beam energy, whether it is partly shared with the ECAL or fully contained in DHCAL. Using the ECAL correction factor it was assumed that the hit to energy relation was the same for all energies, including the ones below 50 GeV. Unfortunately, this cannot be confirmed due to the missing ECAL data in test runs of 40 GeV and below.

The plots from Figures 9.14 and 9.15 are made only with DHCAL hits information, discarding the MIP track from the pion left when the particle passes through ECAL. One of the requirements in the study of late showering pions from April 2011 and pions in the June 2011 data was to have showers fully contained within DHCAL. The study of the energy resolution of late showering pions therefore serves as a direct comparison to the June 2011 data.

The June 2011 period is a DHCAL-only testing period, therefore, the only method available to measure the actual energy of the showers comes from the linearity fit in chapter 8. When this same method is used for the April 2011 late showering pions, the energy

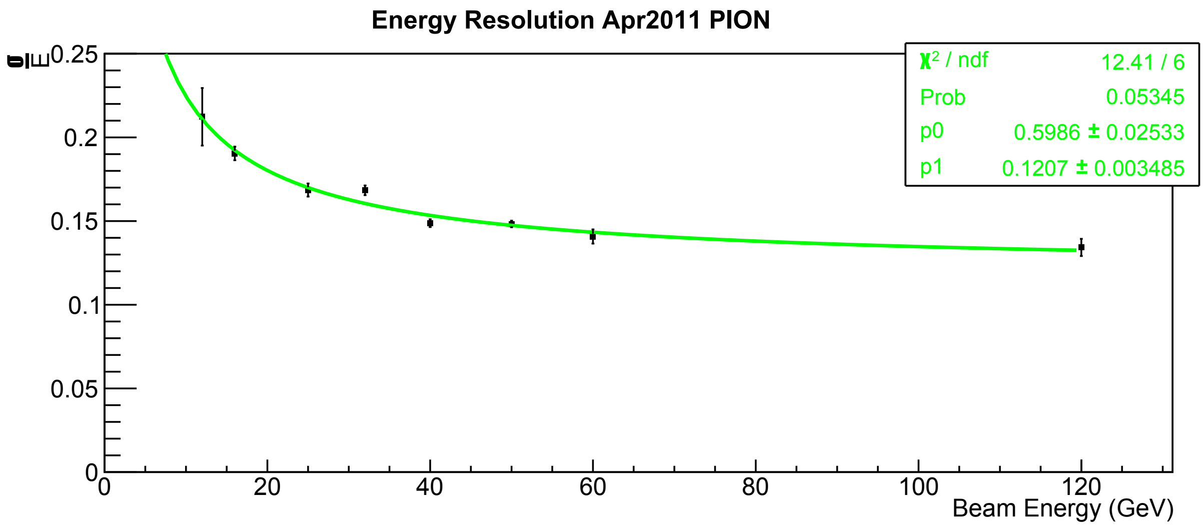

Figure 9.14: Energy resolution of DHCAL for late showering pions using the April 2011 data. The resolution was calculated using the linearity fit (same method used for the June 2011 data). The fitted function is found in Equation 9.8 and the parameter b was set to zero.

Results April 2011		
	DHCAL using Linearity fit	DHCAL using ECAL Correction
Beam Energy	Resolution	Resolution
12 GeV	0.210 ± 0.020	0.152 ± 0.009
16 GeV	0.190 ± 0.004	0.151 ± 0.003
25 GeV	0.169 ± 0.004	0.142 ± 0.003
32GeV	0.168 ± 0.003	0.14 ± 0.002
40 GeV	0.149 ± 0.002	0.127 ± 0.002
50 GeV	0.148 ± 0.002	0.125 ± 0.002
60 GeV	0.141 ± 0.004	0.118 ± 0.002
120 GeV	0.134 ± 0.005	0.113 ± 0.004

Table 9.6: Energy resolution results for late showering pions in the April 2011 testing period. Results are shown for both energy conversion methods.

resolution obtained is comparable for the two periods. In Figure 9.16, the data points for these two sets of data can be observed to be overlapping each other in the common beam energies. In Table 9.7, it can be observed that the lowest energy resolutions are obtained for the combined Si-W ECAL and DHCAL system. The data points for this set remain at resolutions below 11% for the three studied beam energies. The stochastic term a for the

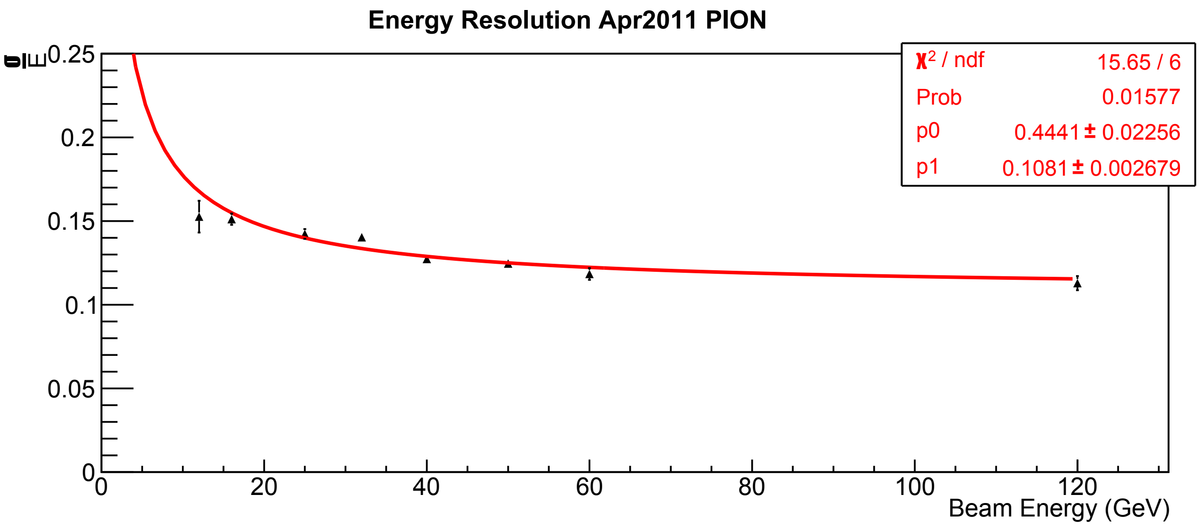

Figure 9.15: Energy resolution of DHCAL for late showering pions using the April 2011 data. The results were calculated using the correction factor from the paraboloid fit method. The fitted function is found in Equation 9.8. The parameter b is set to zero for the fit.

		Energy Resolution PION			
Period and Method	Marker	50 GeV	60 GeV	120 GeV	Average
DHCAL April 2011 Linearity fit	■	0.148	0.141	0.134	0.139
DHCAL June 2011 Linearity fit	◆	0.135	0.146	0.133	0.138
DHCAL April 2011 ECAL correction	▲	0.125	0.118	0.113	0.119
Si-W ECAL+DHCAL April 2011 Sum of energies	●	0.106	0.097	0.072	0.092

Table 9.7: Results for the energy resolution of pions in the two analyzed testing periods for all energy conversion methods. Only the energies 50 GeV, 60 GeV and 120 GeV are compared. The Marker column on the Table represents the markers of the data points in Figure 9.16.

fit of early showering pions resolution is still the highest of all of those studied. This is due to the small number of beam energies available. The energy resolution fit with only three data points does not give a good representation of the expected behavior for the energy resolution at beam energies lower than 50 GeV. Therefore, it cannot be properly

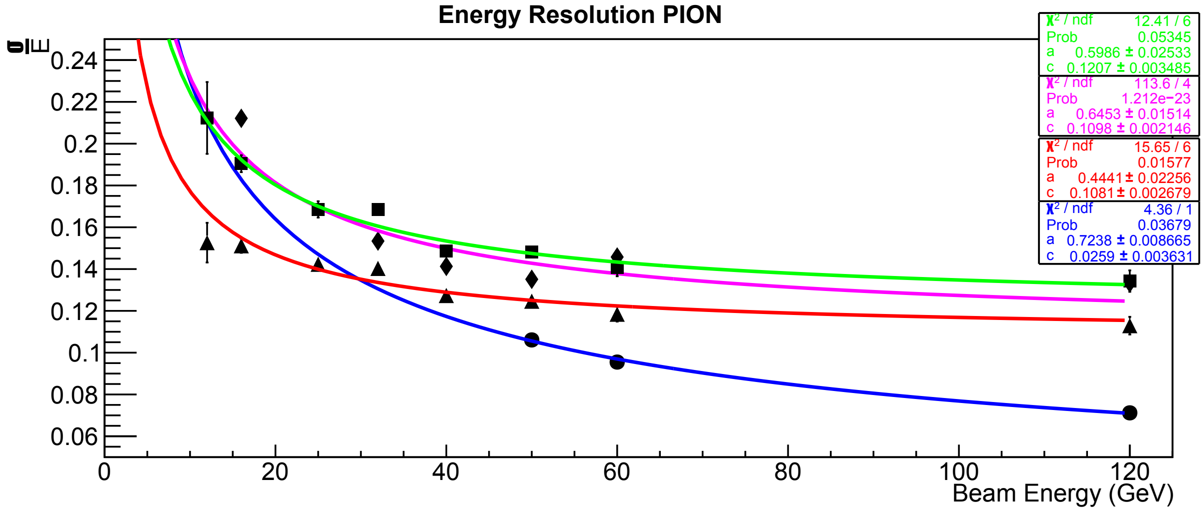

Figure 9.16: Hadronic energy resolution comparison between the June 2011 and April 2011 testing periods. The April 2011 results are shown for three methods of measuring the energy resolution. All of the lines represent fits to the data points following Equation 9.8 with b=0. Green and squares: Energy resolution of late showering pions for April 2011 calculated using the linearity fit. Magenta and diamonds: Energy resolution of pions in the June 2011 period, calculated from the linearity fit. Red and triangles: Energy resolution of late showering pions for April 2011 calculated using the correction factor from the paraboloid fit method. Blue and circles: Energy resolution of Early showering pions for the Si-W ECAL+DHCAL set up from April 2011.

compared to the results from other testing periods. However, the energy analysis was still used to improve the energy resolution for the late showering pions from the same period.

The presented energy analysis of the Si-W ECAL+DHCAL system demonstrates that the presence of the Si-W ECAL directly improves the energy resolution of DHCAL. Using the ECAL correction factor to calculate the energy of the showers of late pions contained within DHCAL shows an improvement on the energy resolution when compared to the June 2011 pions. This can be observed in Table 9.8. A major improvement is observed between the June 2011 pions and the April 2011 pions using the ECAL correction factor. The resolution decreases by 14% on average for the three beam energies. This is shown in Table 9.9. On the same Table, it can be seen that the energy resolution improves by 22.7% on average when part of the hadronic shower is measured by the Si-W ECAL.

		Energy Resolution Fit parameters	
Period and Method	Fit line color	a($GeV^{\frac{1}{2}}$)	c
DHCAL April 2011 Linearity fit	Green	0.599 ± 0.025	0.121 ± 0.005
DHCAL June 2011 Linearity fit	Magenta	0.645 ± 0.015	0.110 ± 0.002
DHCAL April 2011 ECAL correction	Red	0.444 ± 0.023	0.108 ± 0.003
ECAL+DHCAL April 2011 Sum of energies	Blue	0.724 ± 0.009*	0.026 ± 0.004

Table 9.8: Fit parameters from the fit of Equation 9.7 all the data points in Figure 9.16. The parameter b was set to zero for all fits. All the results in the table correspond only to hadronic showers. **This fit was performed with only three data points*.

	Difference between energy resolutions			
Compared periods	50 GeV	60 GeV	120 GeV	Average
DHCAL April 2011 Linearity fit to DHCAL June 2011 Linearity fit	-6%	4%	-1%	-1%
DHCAL June 2011 Linearity fit to DHCAL April 2011 ECAL correction	-7%	-19%	-15%	-14%
DHCAL April 2011 ECAL correction to ECAL+DHCAL Sum of energies	-15%	-18%	-36%	-23%

Table 9.9: Percentile difference between the data points of energy resolution for 50 GeV, 60 GeV and 120 GeV for pions in all studied testing periods and methods.

9.5.4 Systematic uncertainties

The results of this energy analysis have associated systematic errors. Only the errors associated to the containment cuts were estimated, these are discussed next.

Table 9.10 shows the percentage of hadronic events rejected by the containment in DHCAL conditions. The results show that the leakage in this detector setup is a function of the beam energy, as expected. The analysis of Section 9.5 was repeated without the containment condition to calculate an estimate of the systematic errors in the energy resolution associated to this cut, the results can be seen in Table 9.11. The estimated systematic errors are smaller than the statistical errors for the two studied methods (shown in Tables 9.4 and 9.5), with the exception of the results for 120 GeV. This could show a correlation between the percentage of discarded events and the size of the systematic uncertainties, as the 120 GeV test runs presented the most leakage.

Beam Energy	Run	Discarded events (%)
50 GeV	630081	0.7
60 GeV	630090	1.3
	630091	1.2
	630092	1.5
	630093	1.5
120 GeV	630095	4.5
	630097	4.6
Total		1.6

Table 9.10: Percentage of events discarded from each run by the DHCAL containment condition cut. All the events are hadronic events from the April 2011 sample.

	Systematic uncertainties from containment cut			
	Diagonal fit		Sum of Energies	
Beam Energy	Energy resolution	a($GeV^{\frac{1}{2}}$)	Energy resolution	a($GeV^{\frac{1}{2}}$)
50 GeV	0.0001	0.001	0.0001	0.0006
60 GeV	0.001	0.002	0.0005	0.002
120 GeV	0.002	0.017	0.004	0.015

Table 9.11: Systematic errors associated to the containment cuts for in the energy resolution study for the April 2011 testing period.

The rest of the systematic errors come from many factors distributed throughout the complete methodology of this project. An important contributor to the systematic uncertainties would be the cuts for particle ID from Chapter 6. Since the Cherenkov detectors did not work, the particle ID was done using the data itself, thus introducing a bias with a small but non-zero wrong-particle contamination. To estimate the associated systematic errors, the procedure would have been to vary the cuts, repeat the whole analysis for each variation and extrapolate the results to zero contamination. Time did not allow for this analysis, and it would not significantly change the energy resolution improvement results since the systematics would cancel at first order in the ratios from Table 9.9.

Another source of systematic errors would be the use of simple Gaussian forms to fit the hits and energy distributions in Chapters 8 and 9. The systematic uncertainty analysis could be done by varying the range of the Gaussian fits and repeat the analysis as it was explained above for the particle ID.

A large part of the systematic uncertainties in the energy resolution analysis comes from the unfortunately small data sample available, these were not estimated. These systematic errors could explain the difference in resolutions between the April 2011 late showering pions and the June 2011 pions. These two parameters are expected to be compatible with each other since the same methodology was applied to them. Unfortunately, the systematic error analysis of these factors was not further analyzed due to time constraints.

Chapter 10

Conclusions

A study of the combined performance of the DHCAL and the Si-W ECAL using April 2011 data from test runs at Fermilab was presented.

The high granularity of the two prototypes allowed for the identification of faulty layers in the test runs and the application of a particle identification method based on the shape of the showers and MIP tracks. This method, although proved to be functional for the scope of this project, could be improved by the addition of machine learning algorithms that take into account more of the run parameters calculated for each event. The high radiation length to nuclear interaction length ratio of the absorbers facilitated the separation of hadronic events from electromagnetic events.

As for the alignment results, the measurements after moving the DHCAL show that it is possible to do an offline correction to the misalignment between the detectors. The results can then be applied to the complete set of hits from the test runs. This was not done for the set of data used in this project since the correction of alignment does not improve the energy resolution of the detectors in test runs, but, this is not the case for in-situ jet energy resolution studies. Correcting the alignment using a larger sample of muons than the number available for this project, can improve the assignment of energy deposits of the same jet in the hadron calorimeter, electromagnetic calorimeter, and tracker. In-situ, the alignment procedure can be done using tracks from collision products, particles from jets or cosmic rays.

The linearity of the DHCAL was measured. The data shows that the saturation effect in the digital calorimeter is similar for electromagnetic and hadronic showers. It is also important to note that it was found that the saturation of hadronic showers is consistent with or without an ECAL positioned in front of the DHCAL. The only difference between the two sets of data was a decrease in the mean number of hits when ECAL is included. In future studies, the linearity could be studied only on the shower part of the event to confirm more precisely whether the decrease in the hits is due to the part of the MIP track left in the ECAL or to other processes.

The energy study for pions was successful, even for the limited data available for the Si-W ECAL+DHCAL test runs. It was shown that the conversion to energy from number of hits in DHCAL does improve by adding the energy measured by the ECAL in the equation. This is noticeable by the measured energy resolution of the April 2011 late showering pions when compared to the resolution of the June 2011 pions.

Unfortunately, the lack of lower-energy test runs made the energy resolution analysis of the Si-W ECAL+DHCAL system impossible to be properly compared to other combined CALICE calorimeter systems, such as the Si-W ECAL+AHCAL+TCMT commissioning results.

The methods developed for this thesis can be applied to the study of pion energies of the DHCAL in future testing periods with the Si-W ECAL or other CALICE ECAL prototypes. By applying the same methodology to a larger set of data, the results can be improved in terms of systematic errors.

List of Abbreviations

AHCAL Analogue Hadron Calorimeter. 29

DC Direct Current. 23

DHCAL Digital Hadron Calorimeter. 2

ECAL Electromagnetic Calorimeter. 20

FEBs Front-End Boards. 56

GRPC Glass Resistive Plate Chamber. 30

HCAL Hadronic Calorimeter. 20

ILC International Linear Collider. 1

ILD International Linear Detector. 25

LHC Large Hadron Collider. 1

MinDHCAL Minimal Absorber DHCAL. 32

MIP Minimum Ionizing Particle. 9

PET Polyethylene terephthalate. 34

PFA Particle Flow Algorithm. 24

RPC Resistive Plate Chamber. 31

ScECAL Scintillator strip-based ECAL. 33

SDHCAL Semi Digital Hadron Calorimeter. 30

Si-W ECAL Silicon-Tungsten Electromagnetic Calorimeter. 2

SiD Silicon Detector. 25

SiPM Silicon Photomultiplier. 30

SPS Super Proton Synchrotron. 22

TCMT Tail Catcher and Muon Tracker. 32

Bibliography

[1] D. Trojand, "A Novel Digital Hadron Calorimeter : Analysis and Calibration with Muons," Master's Thesis, McGill University, 2012, pp. 1–124.

[2] B. Freund *et al.*, "DHCAL with Minimal Absorber : Measurements with Positrons The CALICE Collaboration," *Instrumentation*, vol. 11, 2016. DOI: `10.1088/1748-0221/11/05/P05008`.

[3] I. Viarouge, "Calibration of the Digital Hadron Calorimeter using Data Track Segment Analysis," Master's Thesis, McGill University, 2018.

[4] D. Griffiths, *Introduction to Elementary Particles*, 2nd Edition. Wiley-VCH, 2004, ISBN: 978-3-527-40601-2.

[5] G. Kane, *Modern Elementary Particle Physics*, 2nd Edition. Cambridge University Press, 2017, ISBN: 9781107165083.

[6] *Standard Model of Elementary Particles*. 2019. [Online]. Available: `https://it.wikipedia.org/wiki/File:Standard_Model_of_Elementary_Particles.svg`.

[7] T. Behnke *et al.*, "The International Linear Collider Technical Design Report - Volume 1: Executive Summary," vol. 1, 2013. arXiv: `1306.6327`. [Online]. Available: `http://arxiv.org/abs/1306.6327`.

[8] W. R. Leo, *Techniques for Nuclear and Particle Physics Experiments*. Berlin, Heidelberg: Springer Berlin Heidelberg, 1994, ISBN: 978-3-540-57280-0. DOI: `10.1007/978-3-642-57920-2`. [Online]. Available: `http://link.springer.com/10.1007/978-3-642-57920-2`.

[9] C. Grupen and B. Shwartz, *Particle detectors*, 2nd Edition. Cambridge University Press, 2008, ISBN: 9780521840064. DOI: 10.1017/CBO9780511534966. [Online]. Available: https://doi.org/10.1017/CBO9780511534966.

[10] *Passage of particles through matter*, 2019. [Online]. Available: https://pdg.lbl.gov/2021/reviews/rpp2020-rev-passage-particles-matter.pdf.

[11] C. W. Fabjan and T. Ludlam, "Calorimetry in high-energy physics," *Annual Review of Nuclear and Particle Science*, vol. 32, no. 1, pp. 335–389, 1982. DOI: 10.1146/annurev.ns.32.120182.002003. eprint: https://doi.org/10.1146/annurev.ns.32.120182.002003. [Online]. Available: https://doi.org/10.1146/annurev.ns.32.120182.002003.

[12] G. Arnison *et al.*, "Experimental observation of isolated large transverse energy electrons with associated missing energy at s=540 GeV," *Physics Letters B*, vol. 122, no. 1, pp. 103–116, 1983, ISSN: 03702693. DOI: 10.1016/0370-2693(83)91177-2.

[13] G. Arnison *et al.*, "Experimental observation of lepton pairs of invariant mass around 95 GeV/c2 at the CERN SPS collider," *Physics Letters B*, vol. 126, no. 5, pp. 398–410, 1983, ISSN: 03702693. DOI: 10.1016/0370-2693(83)90188-0.

[14] ATLAS Collaboration, "Observation of a new particle in the search for the Standard Model Higgs boson with the ATLAS detector at the LHC," *Physics Letters, Section B: Nuclear, Elementary Particle and High-Energy Physics*, vol. 716, no. 1, pp. 1–29, 2012, ISSN: 03702693. DOI: 10.1016/j.physletb.2012.08.020. arXiv: 1207.7214.

[15] S. Michizono, "The International Linear Collider Technical Design Report - Volume 4: Detectors," *Nature Reviews Physics*, vol. 1, no. 4, pp. 244–245, 2019, ISSN: 25225820. DOI: 10.1038/s42254-019-0044-4.

[16] M. A. Thomson, "Particle flow calorimetry and the PandoraPFA algorithm," *Nuclear Instruments and Methods in Physics Research, Section A: Accelerators, Spectrometers, Detectors and Associated Equipment*, vol. 611, no. 1, pp. 25–40, 2009, ISSN: 01689002. DOI: 10.1016/j.nima.2009.09.009. arXiv: 0907.3577.

[17] C. Adloff *et al.*, “Construction and commissioning of the CALICE analog hadron calorimeter prototype,” *Journal of Instrumentation*, vol. 5, no. 5, 2010, ISSN: 17480221. DOI: 10.1088/1748-0221/5/05/P05004. arXiv: 1003.2662.

[18] M. Chadeeva, “Hadron Energy Resolution of the CALICE AHCAL and Software Compensation Approaches,” pp. 1–7, 2011. arXiv: arXiv:1202.6184v1.

[19] CALICE Collaboration, “Design, Construction and Commissioning of a Technological Prototype of a Highly Granular SiPM-on-tile Scintillator-Steel Hadronic Calorimeter,” 2022. arXiv: 2209.15327. [Online]. Available: http://arxiv.org/abs/2209.15327.

[20] A. Laudrain, “The CALICE AHCAL: a highly granular SiPM-on-tile hadron calorimeter prototype,” *Journal of Physics: Conference Series*, vol. 2374, no. 1, pp. 1–5, 2022, ISSN: 17426596. DOI: 10.1088/1742-6596/2374/1/012017.

[21] G. Grenier, “Recent developments of the SDHCAL prototype,” *Proceedings of Science*, vol. 380, pp. 1–5, 2022, ISSN: 18248039. DOI: 10.22323/1.380.0095. arXiv: 2202.10386.

[22] H. García Cabrera, “SDHCAL technological prototype test beam results,” *International Workshop on Future Linear Colliders, LCWS 2021*, no. March, pp. 15–18, 2021. arXiv: 2105.06585.

[23] C. Adams *et al.*, “Design, construction and commissioning of the Digital Hadron Calorimeter - DHCAL Electronics,” *Journal of Instrumentation*, vol. 11, no. 7, pp. 1–20, 2016, ISSN: 17480221. DOI: 10.1088/1748-0221/11/07/P07007.

[24] C. Adams, A. Bambaugh, B. Bilki, J. Butler, F. Corriveau, and T. Cundiff, “Design , Construction and Commissioning of the Digital Hadron Calorimeter - DHCAL,” pp. 1–22,

[25] K. Francis *et al.*, “Performance of the first prototype of the CALICE scintillator strip electromagnetic calorimeter,” *Nuclear Instruments and Methods in Physics Research A*, vol. 763, no. 2014, pp. 278–289, 2015. DOI: 10.1016/j.nima.2014.06.039.

[26] J. Repond *et al.*, "Design and electronics commissioning of the physics prototype of a Si-W electromagnetic calorimeter for the international linear collider," *Journal of Instrumentation*, vol. 3, no. 8, 2008, ISSN: 17480221. DOI: 10.1088/1748-0221/3/08/P08001. arXiv: 0805.4833.

[27] C. Adloff *et al.*, "Response of the CALICE Si-W electromagnetic calorimeter physics prototype to electrons," *Nuclear Instruments and Methods in Physics Research, Section A: Accelerators, Spectrometers, Detectors and Associated Equipment*, vol. 608, no. 3, pp. 372–383, 2009, ISSN: 01689002. DOI: 10.1016/j.nima.2009.07.026. arXiv: 0811.2354.

[28] Y. Israeli, "Energy reconstruction of hadrons in highly granular combined ECAL and HCAL systems," *Journal of Instrumentation*, vol. 13, no. 5, 2018, ISSN: 17480221. DOI: 10.1088/1748-0221/13/05/C05002. arXiv: 1803.05232.

[29] S. Bilokin *et al.*, "Commissioning of the highly granular SiW-ECAL technological prototype," Oct. 2018. arXiv: 1810.05133 [physics.ins-det].

[30] R. Pöschl, "The CALICE SiW ECAL Technological Prototype—Status and Outlook," *Instruments*, vol. 6, no. 4, pp. 1–12, 2022. DOI: 10.3390/instruments6040075. arXiv: 2211.07457.

[31] *Atomic and nuclear properties of materials for more than 350 materials*. [Online]. Available: https://pdg.lbl.gov/2020/AtomicNuclearProperties/index.html.